UNIVERSITÀ DEGLI STUDI DI PAVIA

Dottorato di Ricerca in Ingegneria Elettronica, Informatica ed Elettrica

XXXI CICLO (2015 - 2018)

NOVEL MATERIALS AND INNOVATIVE FABRICATION TECHNIQUES FOR THE SUBSTRATE INTEGRATED WAVEGUIDE (SIW) TECHNOLOGY

Ph.D. Candidate: Enrico MASSONI

Tutor: Professor Maurizio BOZZI

Table of Contents

Preface

This dissertation presents the most significant results of my research activity in the framework of the Philosophy Doctorate School entitled “Dottorato di Ricerca in Ingegneria Elettronica, Informatica ed Elettrica”, XXXI cycle, from October 2015 to September 2018. During this period, I was inserted in the Research Unit of the Microwave Laboratory, Department of Electrical, Computer and Biomedical Engineering of the University of Pavia, Italy, under the supervision of Professor Maurizio Bozzi.

The core topic of my research is focused on the Substrate Integrated Waveguide (SIW) technology and its applications to circuits and systems operating in the microwave regime. In particular, a detailed historical overview on the SIW technology, along with its main features and operational principles is summarized and provided in the Introduction of this work. Moreover, in the same Introduction, transitions between SIW and other circuitry, alternative SIW-line configurations, the concept of System on Substrate (SoS), and novel material and fabrication procedures are briefly introduced and discussed, in order to familiarize the readers with the potentialities offered by this technology.

In addition, nowadays, a large number of journal and conference papers, along with patents, has been published by IEEE and other technical associations on the SIW technology and its applications. Indeed, researchers are more and more attracted by this theme, with an ever-growing interest on SIW technology, leading to an overall improvement in the design and manufacturing of SIW devices and systems.

In this framework, materials and fabrication technologies are playing a crucial role. In fact, the selection of a material with performing electromagnetic properties and the investigation on novel fabrication procedures are fundamental aspects to design and experimentally validate innovative SIW components and systems. For those reasons, it is important to consider composite and exotic materials for novel microwave applications, along with a detailed study on original

fabrication procedures. This statement encouraged me to explore the innovative additive manufacturing techniques to implement microwave devices. A large variety of different methodologies are nowadays available while dealing with 3D printing: from the Fused Deposition Modelling (FDM), to the Binder Jetting, passing by photo-polymerization procedures. All those processes could be adopted to manufacture in a successful way SIW components. At the same time, a detailed electromagnetic characterization of the materials is required. In this way, it is also possible to discover different composite substances, showing improved properties with respect to the standard commercial laminates, usually adopted in the realization of SIW circuitry.

Bearing in mind all those features, a detailed analysis on 3D-printed SIW interconnects has been considered in Chapter 1. At first, a brief investigation on additive manufacturing procedures has been presented, highlighting the benefits provided by the FDM technique. Subsequently, the printable commercial thermoplastic polyurethane Ninjaflex® has been characterized, retrieving its electrical properties (ε_r and $\tan\delta$). To this aim, two main classical procedures have been considered: a waveguide (narrow-band) methodology and a microstrip lines (wideband) methodology, respectively. In addition, as mentioned in Appendix 1, an alternative, non invasive, enhanced SIW cavity sensor has been introduced, providing enhanced sensitivity with respect to the standard configuration, leading to a better estimate of the electromagnetic properties of the material under test (MUT). Finally, exploiting the unique feature of the FDM technology, by varying the infill percentage of the 3D-printed material, a complete set of samples has been manufactured and tested. In particular, those measured results are in good agreement with the model of the Maxwell-Garnett equation, thus enabling the possibility of fabricating specimens with selectively different dielectric constants within the same microwave component. Eventually, to prove this concept, a substrate integrated waveguide (SIW)-line and a substrate integrated slab waveguide (SISW)-line have been designed, 3D-printed and experimentally validated, providing a 50% bandwidth enhancement for the single-mode band. In conclusion, Chapter 1 demonstrated the feasibility of FDM technology for the implementation of SIW components, paving the road to a novel class of 3D-printed SIW devices operating in the microwave regime.

Subsequently, after investigating the SIW interconnects of Chapter 1, the versatility of the SIW technology has stimulated the interest in the study of SIW transitions. In particular, in Chapter 2, the attention has been focused on the direct coaxial cable to SIW transitions. At first, an historical overview about SIW coaxial launchers has been widely discussed, presenting the state of the art solutions retrieved in the published scientific literature. Successively, the single SIW mode

coaxial launchers have been examined, separately, for the first two modes, respectively. Specifically, both the launcher of the fundamental quasi-TE_{10} SIW mode and the launcher of the second quasi-TE_{20} SIW mode have been designed via the full-wave electromagnetic software Ansys HFSS. In addition, several parametric analyses on substrate thickness *h*, on the displacement of the coaxial cable insertion, and on the capacitive effect located next to the feeding point have been considered to optimize the transitions. Eventually, back-to-back prototypes have been manufactured and tested, thus validating the simulated predictions. Those encouraging results have incentivized the possibility to merge these two structures into a single transition able to sustain both the propagation of the fundamental and second SIW modes in the same physical prototype. In this way, the innovative combined launcher for the two SIW modes has been generated. Similarly to the previous cases, the device has been simulated through HFSS, parametric analyses have been considered to optimize the structure, and a back-to-back prototype has been manufactured to prove the simulated outcomes. In particular, this solution allows for a direct insertion of the coaxial cable through the substrate, thus implementing a simple, repeatable and robust to fabrication inaccuracies solution. Besides, the possibility to cover two different frequency bands, using only one physical transmission channel, makes the two SIW modes combined launcher an extremely interesting and versatile transition for the development of a novel class of performant SIW components and systems for the new wireless sensors networks (WSN) and fifth generation (5G) applications.

Afterwards, in addition to the results achieved in Chapter 1 and Chapter 2, a detailed study on SIW antennas has been conducted in Chapter 3. After a generic historical overview on SIW antennas, the attention has been focused on leaky-wave antennas (LWAs). In particular, the double-sided SIW LWA has been considered and presented along with its theoretic foundations and working principles. In parallel, an investigation proved the possibility to reduce transmission losses when considering the second quasi-TE_{20} mode and adopting the SISW technology, as already observed in Chapter 1. Those features motivate the design, implementation and testing of a double-side SIW LWA and a double-sided SISW LWA, respectively, with the aim of increasing the antenna efficiency. Moreover, the transition implemented to properly excite the second quasi-TE_{20} SIW mode for the LWA originates from the counterpart presented in Chapter 2. In this way, both the benefits of the interconnections investigated in Chapter 1 and the benefits of the transitions of Chapter 2 have been adopted to implement the antennas of Chapter 3. Furthermore, those prototypes, operating at 28 GHz, paved the road to the future implementation of a performing class of double-sided SISW LWA with extremely

high efficiency for the novel fifth generation (5G) of mobile communications and wireless sensors networks (WSN).

Eventually, all the achieved results are summarized in the Conclusions of this work.

In addition, I would like to express my sincere and deep gratitude to Professor Maurizio Bozzi, for his strenuous support and clever guidance through the entire period, spent as a Ph. D. student. He has been my academic tutor, my scientific advisor, and my technical and educational supervisor. A precious guide to work with in a scientific research environment.

Besides him, I am very grateful to Professor Luca Perregrini, head of the Microwave Lab., and Professor Marco Pasian, for the continued presence, the helpful suggestions and the useful discussions. A special mention is also addressed to Professor Marco Bressan and Professor Paolo Arcioni.

Moreover, I have to mention also some precious collaborators I had the honour to work with. First, the research group of the 3D@UniPV Laboratory, lead by Professor Ferdinando Auricchio, that introduced me to the fascinating world of the additive manufacturing procedures. Subsequently, Professor Umberto Anselmi Tamburini, from the Chemical Department of the University of Pavia, for the innovative contribute on high dielectric resonators. Following, Professor Cristiano Tomassoni, University of Perugia and Professor Giuseppe Macchiarella, Politecnico di Milano, for the theoretical deep vision on understanding microwave filters.

Furthermore, I wish to thank Professor Ke Wu and his research group of the Poly-Grames, École Polytechnique de Montréal, Université de Montréal, Montréal, Quebec, Canada, where I spent six months as a visiting research intern, from March to August, 2018.

Subsequently, I would like to list in chronological order some fundamental achievements and recognitions obtained during these three years:

- March 2016 - “Best poster award” presented by the IEEE Circuit and Systems Society (CAS)-President Professor Franco Maloberti during the special day-event of the CAS-Society for Ph.D. students (Ceremony held on March 6th, 2016 in Villa del Grumello in Como, Italy);
- October 2016 - "Student Challenge Award” presented by the European Microwave Association (EuMA) during the 16th European Microwave Week at the 46th IEEE European Microwave Conference (EuMC 2016), London, United Kingdom;
- June 2016 - SYMETA Grant ESoA2016 "Advanced Materials for Antennas” to cover the registration fee for the participation at the European

School of Antennas (ESoA2016) Course held in Athens on June 20-24, 2016 (after the successful final exam);

- May 2017 - CST Grant ESoA2017 "Antenna measurements at millimetre and submillimetre wavelengths" to cover the registration fee for the participation at the European School of Espoo (Helsinki - Finland) (ESoA2017) Course held in Espoo (Helsinki - Finland) on May 8-12, 2017;
- June 2018 - "Honorable mention" at the 3MT Competition for the presentation entitled "Hearing a whisper in the middle of a concert: be selective!", during the IMS2018, in Philadelphia, PA, USA, June 10-15, 2018.

Additionally, another special mention should be reserved for the IEEE Student Branch of Pavia (IEEE SB10871) and its sub-units I had the honour to serve as Chair, from December 2015 to now. Thanks to all Professors, colleagues and students for the organization of incredible activities (in collaboration with the student association Pavia Engineering Student Branch PESB). Thanks to the IEEE Italy Section, chaired by Tiziana Tambosso, and Region 8 for the recognitions I will briefly summarize here.

IEEE Italy Section - "Exemplary Student Branch Award" (2016 "First Classified", 2017 "First Classified", 2018 "Most Innovative Unit").

IEEE (Region 8) - "Regional Exemplary Student Branch Award" (2016/2017 and 2017/2018).

Moreover, a heartfelt thank goes to the European Microwave Association (EuMA) and the Young Professional (YP) round table I was involved in.

Later, my deep and sincere gratitude goes also to the Associazione Italiana di Elettrotecnica, Elettronica, Automazione, Informatica e Telecomunicazioni (AEIT) for the award of the prestigious and meritorious scholarship "Isabella Sassi Bonadonna" edition 2017 (nationwide competition).

In addition, even the IEEE Microwave Theory and Techniques Society (MTT-S) deserves to be mentioned and thanked for the "Graduate Fellowship", that was assigned to me for the 2018 edition (one out of ten awarded annually worldwide).

Eventually, I really liked working with the people of the Pavia Microwave Lab.! They were not only great colleagues but also sincere friends. Many of them also co-authors of different scientific works, and enjoyable mates during conferences time.

Pavia, September 2018

Enrico Massoni

Introduction

An Overview on the Substrate Integrated Waveguide (SIW) Technology

The general aim of this Introduction is to familiarize the readers with the Substrate Integrated Waveguide (SIW) technology and its applications to microwave and mm-waves components and systems. In particular, a brief historical overview will be highlighted, following the guidelines of [1]. In detail, starting from the very first applications, till reaching the modern implementations, the SIW technology has always attracted academic, scientific and industrial attention, stimulating a productive and ever-growing research in this field. Even from a publication perspective, there has always been an ever-increasing interest on the SIW technology. Proof of this statement is given in Fig. 1, where the number of scientific products is detailed and subdivided year by year. Specifically, this great output on SIW technology is expanding more and more, thus demonstrating the intriguing potentialities of this technique, suited for microwave and mm-waves applications. Moreover, the versatility of SIW technology allows for easy and effective integration with other technologies, thus solving the problem of assembling the different parts constituting the same system. In addition, this feature also leads to a cost-effective implementation of SIW components, realizable even through simple and low-cost manufacturing procedures. A detailed study of those aspects, along with theoretical formulas and analytical derivations, will be discussed in the next paragraphs.

However, another way to understand the advantageous properties of SIW technology could be the one to analyse the historical evolution, that inherently generates this technology. In particular, a summarizing roadmap of the progress of microwave technology during the last decades is sketched in Fig. 2. From the first generation of classical metallic waveguide components of the last century, to the fifth generation of SIW devices, the technological development has been performing and very intense. Eventually, this itinerary has lead to the introduction

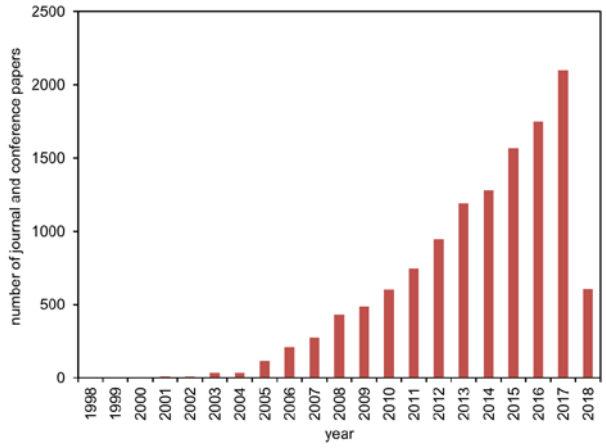

(*a*)

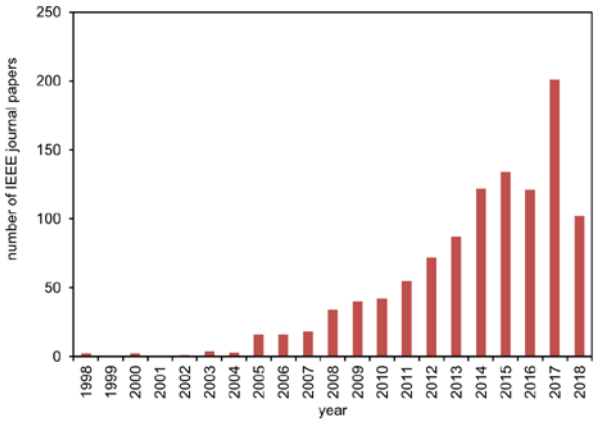

(*b*)

Fig. 1 - Number of publications on the SIW along the years:
(*a*) Total number of journal and conference papers (source: Google Scholar);
(*b*) Number of papers appeared in the IEEE journals (source: IEEExplore).
Chart updated on May 1, 2018 [1].

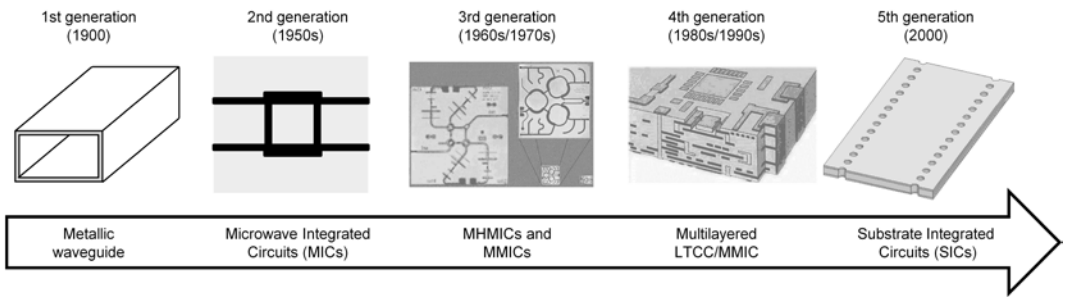

Fig. 2 - Roadmap of the global progress of microwave technology,
from the early waveguide techniques to the current high-density integrations and SIW [1].

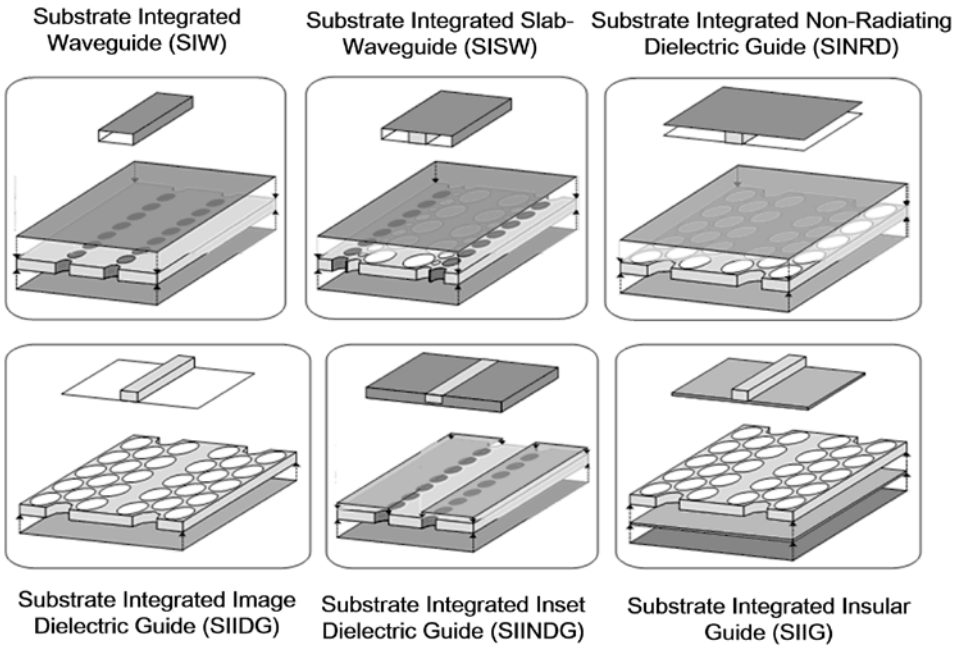

Fig. 3 - List of the major topologies of non-TEM-mode-based substrate integrated structures [1].

of the SIW technology as the most promising for a future implementation of a novel class of microwave and mm-wave components and systems.

Last, the SIW technology has also laid the groundwork for the development of different topologies of non-TEM-mode-based substrate integrated structures. A comprehensive list is reported in Fig. 3, highlighting the three-dimensional models of those guiding lines [1]-[2]. In particular, those configurations could be used to implement a large set of both passive and active components, paving the road to the future implementation of several diverse classes of microwave and mm-wave components and systems, responding to the challenges of the upcoming fifth generation (5G) of mobile applications, of the wireless sensors networks (WSN) and of the Internet of Things (IoT).

In conclusion, all those aspects stimulate the research outcomes that will be presented in this manuscript. In particular, a special consideration on fabrication technologies and materials will be addressed along the entire work, in conjunction with innovative SIW-line configurations, sensors, transitions and high efficiency antennas. Indeed, it is of crucial importance to focus the attention on those features for the future implementation of a pioneering class of original, advanced, compact, low-cost, and low-weight microwave and mm-wave devices and systems.

Eventually, in the next Sections, a general overview about the Substrate Integrated Waveguide (SIW) technology will be highlighted. In particular, the most relevant aspects, that are helping the researchers to efficiently engineer SIW components and systems, will be presented in detail. Specifically, theoretic foundations, design criteria, and some practical examples will be discussed in the next paragraphs, following the guidelines of [3].

I.1 The Origin of SIW Technology

The ease of integration between passive components, active components, transmission lines and antennas represents an essential requirement for the novel circuitry and systems operating in the microwave and mm-wavelength regime. Usually, from a fabrication point of view, each component originates from a different production process, and subsequently, it is incorporated in the final system. Due to this reason, several problems may arise: low compatibility between interfaces of different modules and radiation leakage. Furthermore, additional losses will be radiated in the environment, thus deteriorating the overall performances of the entire system. Moreover, due to the final arrangement of those different blocks, undesired interferences could appear and disturb the surrounding elements.

Among all the possible technologies, the Substrate Integrated Waveguide (SIW) technology seems to excel for its valuable properties. In fact, its beneficial aspects are of immediate comprehension. Indeed, this technology is able to merge the advantages of the standard metallic waveguides and the advantages of the classical planar circuits. A detailed analysis of those aspects will be presented in the following paragraphs.

In order to summarize the properties of the standard printed planar technology, a simple microstrip line has been considered, as the most common example inside this class of devices. In particular, Fig. 4 (*a*) highlights the three-dimensional model and lists the properties of the microstrip line device. In this case, the implementation of light-weight, low-cost, and compact components is guaranteed even using elementary fabrication procedures. In reverse, the structure is not shielded, thus suffering from the flaws of high radiation losses and high cross talking.

Conversely, as for standard non-planar technologies, a classic metallic rectangular waveguide has been considered. In this case, Fig. 4 (*b*) highlights the three-dimensional model and lists the properties of the waveguide.

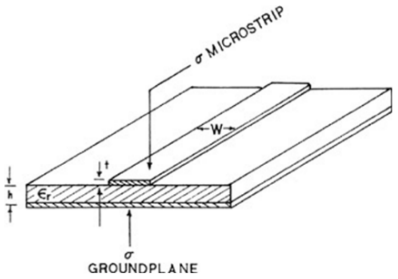

MICROSTRIP LINES (planar)

- Light and compact
- Low fabrication cost
- High losses
- High cross-talk

(*a*)

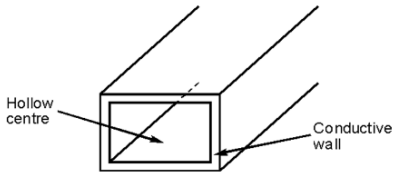

METALLIC WAVEGUIDES (non-planar)

- Low losses
- Completely shielded
- Bulky and expensive
- Difficulties with active components

(*b*)

Fig. 4 - Comparison between standard printed planar technology and conventional non-planar technology. 3D models of the prototypes along with their pros (green) and cons (red):
(*a*) The microstrip line;
(*b*) The metallic rectangular waveguide.

In particular, the structure is completely shielded, thus providing low transmission losses. In fact, thanks to this solution any radiation leakage is avoided. In addition, this feature leads also to the possibility of implementing high quality factor components, with high selectivity rate. Furthermore, those structure could handle high power levels, enabling even the design of high power systems operating in the microwave and mm-wave regime. On the opposite, waveguides are really expensive devices, the production requires really high-priced machinery and the time to market usually consists of a long process. Eventually, they are not at all light-weight components, and the integration with active circuitry is of difficult implementation.

Afterwards, the birth of the SIW technology originates from the mixed combination of all the positive aspects of the two classes of devices mentioned above. For these reasons, the SIW technology permits the implementation of waveguides in planar form, that are benefiting from the advantages of both classical metallic waveguides and printed planar circuitry. In particular, from an historical perspective, the first patent was presented in Japan in 1994 [4], but from an academic point of view, the seminal works are ascribed to Professor Ke Wu (École Polytechnique de Montréal, Québec, Canada), since 2001 [5]-[8].

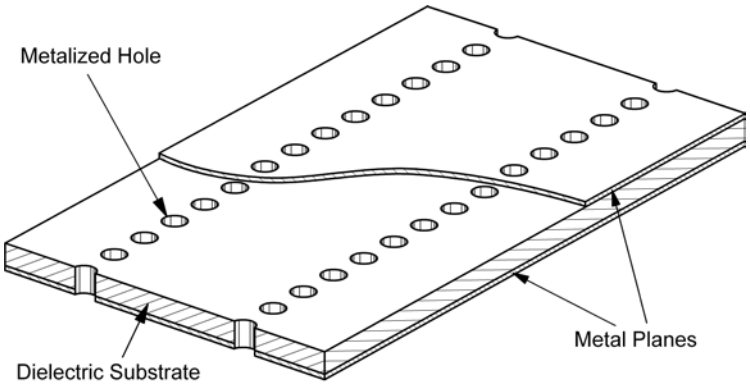

Fig. 5 - 3D model of a generic substrate integrated waveguide (SIW)-section [3].

Specifically, the three-dimensional model of a generic SIW section is shown in Fig. 5. Precisely, the structure consists of a dielectric substrate with both faces covered by a copper cladding (or similar metal, conductive element). Those planes constitute the so-called “top” metal plane (upper face) and “bottom” metal plane (lower face). In addition, two rows of metalized cylinders, the so-called “posts” or “metal via”, are used to implement the lateral metal walls. Indeed, their purpose is to confine the propagation of the electromagnetic waves inside the structure itself, and to ensure the electrical contact between the upper and the lower metal planes. In this way, they perfectly resemble the lateral walls of classical metallic waveguides, creating a complete shielding with respect to the surrounding environment. Moreover, other valid configurations admit the usage of trenches or cuts instead of cylinders, maintaining the same functionality.

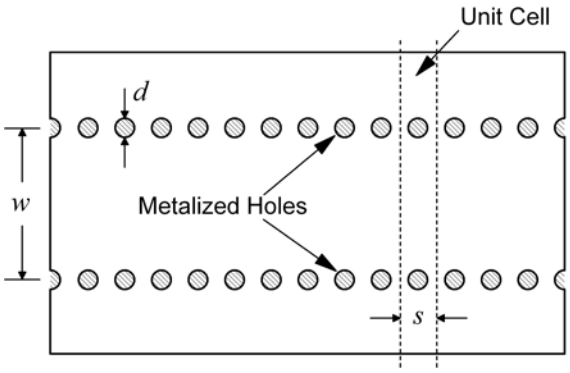

Fig. 6 - Top view of a generic SIW section along with its geometric properties [3].

I.2 The Geometric Properties of SIW Technology

A top view of the generic SIW structure is presented in Fig. 6, along with its main geometric parameters. In particular, the SIW-line is completely described by these three parameters:

- w = width (distance between the two rows of metal posts);
- d = post diameter;
- s = spacing between two adjacent posts.

Each single parameter has an impact on the electromagnetic performances of the structure itself. For this reason, detailed analytical studies have been performed to identify the design requirements. A brief summary is reported in the next paragraphs.

In detail, at first, the selection of the width *w* enables to identify the cut-off frequency of the fundamental mode propagating in the structure, thus determining the single-mode SIW bandwidth, as well as the propagation of the high order modes. For this reason, the choice of *w* exclusively depends on the project requirements, and it should be set to fulfil them, exactly like in the design of classical metallic waveguides.

Instead, some restrictions apply to *s* and *d*. First, to avoid the band-gap effect, the diameter of the single post *d* has to be eight time lower than the total width *w* of the SIW-line. At the same time, the spacing *s* between two adjacent posts must be lower than two and a half times the diameter *d* of the single post, in order to define the confinement of the electromagnetic field inside the structure. Usually, a rule of thumb suggests to adopt the spacing *s* as twice the dimension of the diameter *d*. Another possibility could suggest to adopt the spacing between adjacent posts of the same dimension of the diameter, thus using the lower limit $s=d$, without any space between consecutive posts. This solution is feasible, the device is implementable, and it provides complete shielding, but it is not convenient for manufacturing reasons.

To summarize:

$$d < \frac{w}{8} \qquad and \qquad s < \frac{5}{2}d \quad (usually\ adopting\ s = 2 \cdot d)$$

In addition, some other parameters must be considered, to fully describe the dielectric substrate adopted to implement the SIW structure:

- h = thickness;
- ε_r = dielectric constant;
- $\tan\delta$ = dielectric loss tangent;
- σ_C = metal conductivity.

In this way, all the relevant properties have been set, and it is possible to start the design. Those features are commonly stated in the data sheets provided by the selling companies. The thicknesses are usually very thin, in order to maintain the required planarity, standard values range from 0.005" (0.127 mm) to a maximum of 0.125" (3.175 mm), with the most commonly used 0.020" (0.508 mm). In addition, the metal conductivity depends on the cladding, standard values are 17.5 μm (1/2 oz) or 35 μm (1 oz). Eventually, a widespread range of ε_r and $\mathrm{tg}\,\delta$ is provided by different companies, enabling the possibility to realize a huge variety of projects with different requirements.

Finally, due to its geometric characteristics the SIW-line presents a periodic structure. For this reason, it is possible to study the unit cell, highlighted in Fig. 6. In particular, this unit cell is formed by a portion of double grounded dielectric substrate and a pair of metalized posts. Furthermore, the analysis of this single element dramatically reduces the computation time, and by using the simulated outcomes it is possible to replicate the same considerations to the whole SIW structure. This observation, combined with symmetry planes (electric or magnetic walls), represents an important feature for SIW, especially during the initial phase of the project.

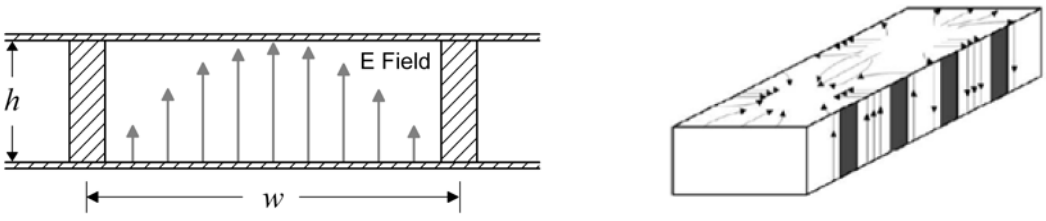

(*a*) (*b*)

Fig. 7 - The working principle of SIW technology [3]:
(*a*) Front-view of the electric field pattern for the fundamental quasi-TE_{10} SIW mode;
(*b*) Depiction of the current distribution.

I.3 The Working Principle of SIW Technology

The working principle of the SIW is completely similar to the one of the classical metallic waveguides. Peculiarly, Fig. 7 highlights the field and current distributions in a generic SIW-line. In particular, it is evident from Fig. 7 (*a*), as the fundamental SIW mode is really similar to the TE_{10} mode of the standard rectangular waveguide. Furthermore, the surface current, represented in Fig. 7 (*b*), is forced to flow on the top and bottom metal planes through the lateral metal cylinders, thus forming a completely shielded structure. Due to this property, thanks to the vertical flow of the surface current along the lateral posts, the structure itself supports only the TE_{n0} propagation modes. For the same reason, the contributions of the TM and TE_{np} modes, with $p \neq 0$, are negligible because of the absence of the longitudinal surface current term. In fact, this term, would have produced strong perturbations along the gaps, thus inducing high radiation losses, undesired effect that must be avoided. Additionally, as stated in [9], the SIW components have been classified as *H*-plane waveguide structures. In fact, the electric field is normal to the broad wall and its amplitude does not vary in the vertical direction. Moreover, the thickness *h* of the substrate plays no role in the characteristics of wave propagation, except for conductor losses, as it will be observed in the following Sections.

I.4 The Equivalent Rectangular Waveguide

The generic SIW structure, with its main geometric parameters, as well as its working principle, has been introduced in the previous Sections. Immediately appeared the strong similarity with the classical metallic rectangular waveguides. For this reason, and since its very beginnings, researchers started modelling the SIW with the equivalent rectangular waveguide. In fact, both structures, the SIW and the classical rectangular waveguide, support the same fundamental mode, the TE_{10}. This property enables the possibility to use the equivalent rectangular waveguide as the simplest model to design SIW structures.

Peculiarly, simple and straightforward formula have been proposed to link the geometric parameters of SIW to the ones of the classical metallic rectangular waveguides [10]. By means of empirical validations, a direct formula to retrieve the effective length w_{eff} of the equivalent rectangular waveguide has been proposed in [10]:

$$w_{eff} = w - \frac{d^2}{0.95 \cdot s}$$

where *w*, *s*, and *d* represent the geometric parameters of the SIW-line. Specifically, this provides an immediate value for the width of the equivalent rectangular waveguide with a reasonable accuracy (± 5 % in the validity range: $s < 4 \cdot d$).

Instead, more refined and alternative approaches have been proposed for the study of critical filters, microwave devices selective in frequency, and components with narrow bandwidth. A couple of examples are [10], [11]:

$$w_{eff} = w - 1.08\,\frac{d^2}{s} + 0.1\,\frac{d^2}{w} \qquad where \quad s < 3 \cdot d \quad and \quad d < \frac{w}{5}$$

$$w = \frac{2w_{eff}}{\pi} cotg^{-1}\left(\frac{\pi s}{4w_{eff}} \ln\frac{s}{2d}\right) \qquad where \quad s < 10.8\,w$$

I.5 The Loss Mechanism in SIW

An accurate study on the loss mechanism is required while designing a generic SIW structure. It is of fundamental importance being able to reduce transmission losses and to avoid the possible band-gap effect, that arises because of the periodicity of the insertion of the metal posts in the structure. Due to the simplicity of the SIW structure, it is possible to minimize the effect of the losses and to get rid of the band-gap effect just acting on the geometric parameters of the SIW: the width *w*, the post diameter *d*, and the relative spacing between adjacent posts *s*. In addition, several formulas have been proposed during the recent research on SIW [3], and the most important are reported in the following paragraphs. Moreover, it is possible to distinguish three main contributions for the loss mechanism in SIW [12]: the conductor losses (α_C), the dielectric losses (α_D), and the radiation losses (α_R). In particular, the first two exhibit a similar behaviour of classical metallic rectangular waveguides full of dielectric, instead, the third one is obviously not present in totally shielded systems.

Furthermore, by exploiting the linearity property and the superimposition principle, it is possible to express the total contribution by simply adding each single effect:

$$\alpha_{TOT} = \alpha_C + \alpha_D + \alpha_R$$

I.5.1 The Conductor Losses (α_C)

This class of losses originates from the finite conductivity (σ_C) of the metal planes and of the cylindrical posts present in the SIW structure. A formula has been proposed to estimate the entity of those losses [3]:

$$\alpha_C = \frac{\sqrt{\pi f \varepsilon_0 \varepsilon_r}}{h\sqrt{\sigma_C}} \frac{1 + 2\left(\frac{f_c}{f}\right)^2 \frac{h}{w_{eff}}}{\sqrt{1 - \left(\frac{f_c}{f}\right)^2}}$$

where f represents the operative frequency, f_c the cut-off frequency of the fundamental SIW mode, σ_C the metal conductivity, ε_0 the vacuum permittivity, ε_r the relative dielectric permittivity, h the substrate height, and w_{eff} the equivalent width.

In addition, it is important to address attention to the thickness h of the substrate, that strongly influences the conductor losses. In fact, when considering a fix amount of transmitted power, the increase of h entails a reduction of the amplitude of the electric current density flowing upon the metal layers, thus leading to a significant reduction of the power dissipated by the Joule effect. There is so an inverse proportionality between α_C and the substrate thickness h. For this reason, the height of the structure is a crucial parameter when minimizing conductor losses during the design phases. Last but not the least, due to the high similarity rate between the SIW structure and the classical metallic rectangular waveguides, the limitation $h_{max} = \frac{w_{eff}}{2}$ has always to be satisfied, thus ensuring the maximum bandwidth for the single-mode regime [13].

I.5.2 The Dielectric Losses (α_D)

The main responsible for dielectric losses in SIW is represented by the dielectric loss tangent $\tan\delta$ of the substrate. Ideally speaking, materials with null $\tan\delta$ represent the lower limit case that cancels the contribution due to dielectric losses. For this reason, it is of fundamental importance to select low $\tan\delta$ materials to minimize the losses in SIW structures.

A formula has been proposed to estimate the entity of those losses [3], [12]:

$$\alpha_D = \frac{\pi f \sqrt{\varepsilon_r}}{c\sqrt{1-\left(\frac{f_c}{f}\right)^2}} \, tan\,\delta$$

where c represents the speed of light in vacuum, f the operative frequency, f_c the cut-off frequency of the fundamental SIW mode, and ε_r and $\tan\delta$ the dielectric parameters. Moreover, in this formula *s*, *d*, and *w* are not present, meaning that the attenuation constant α_D is practically unaffected by the geometrical dimensions of the SIW structure.

Conversely to the case of conductor losses, it is worth noting that the dielectric losses are not decreased when the substrate thickness *h* is increased. Instead, increasing the height means decreasing the *E*-field, reasoning straightforward related to the integration over a generic volume *V*, that is increased by the factor *h* itself, thus reducing the effect of the electric field. One effect compensates for the other, and this trade-off that must be considered during the design steps.

I.5.3 The Radiation Leakage (α_R)

As discussed in the previous Sections, in the SIW configuration, the lateral walls of standard rectangular waveguides are substituted by rows of cylindrical metalized posts. In addition, by adopting the spacing *s* between adjacent posts lower than two and a half times the diameter *d* of the single post ($s < 2.5 \cdot d$), the SIW structure is shielded, and this avoids any radiation leakage. Furthermore, the electromagnetic field is completely confined inside the structure itself and the propagation of the TE_{n0} modes is ensured, as in standard rectangular waveguides. Due to this property, no electromagnetic radiation is spread in the environment, and this is controlled simply by adjusting the mutual position between posts, mostly adopting, as a rule of thumb, $s = 2 \cdot d$.

Instead, when the gap between adjacent metal posts spoils the shielding of the SIW structure, some radiation leakage is appearing. Moreover, while conductor and dielectric losses for SIW can be accurately determined by analytical formula of the equivalent rectangular waveguide, it is more difficult to derive an expression for attenuation constant due to the radiation leakage coming from SIW interconnects.

A formula has been proposed in [14] to estimate the entity of those losses:

$$\alpha_R = \frac{\frac{1}{w}\left(\frac{d}{w}\right)^{2.84}\left(\frac{s}{d}-1\right)^{6.28}}{4.85\sqrt{\left(\frac{2w}{\lambda}\right)^2-1}}$$

This formula provides a direct relation between the geometric parameters of the SIW and the attenuation constant of the radiation leakage, an immediate estimate to evaluate radiation leakage in generic SIW interconnects.

Eventually, in order to have a complete view on different loss mechanisms, a practical example of a generic SIW-line is reported, as in [15], [16], with the following geometric characteristics: w=3.97 mm, d=0.635 mm, s=1.016 mm, ε_r=9.9 and $\tan\delta$=0.0002.

At first, Fig. 8 (*a*) highlights the numerical contributions of both dielectric and conductor losses in the fundamental mode region, from f_c to $2f_c$. The influence of the finite conductivity is almost negligible when compared to the effect of the $\tan\delta$ of standard laminate materials. In particular, this is due to the fact that usually the copper cladding presents a $\sigma_C = 5.8 \cdot 10^7$ [S/m], sufficiently high value to minimize the effect of conductor losses. Instead, commercial laminates usually present $\tan\delta$ values around the magnitude of 10^{-3}, leading to a stronger contribution to the overall losses for the SIW structures.

In addition, in Fig. 8 (*b*) the same example has been adopted to investigate the effect of substrate thickness h on losses. As mentioned before, increasing h helps in reducing the conductor losses, while it has no practical effect on the dielectric losses.

Last, the radiation leakage is considered in Fig. 8 (*c*). In this case, all the geometric parameters are kept at their nominal values, except the spacing between adjacent posts s, that is increased to observe its contribution on α_R. As observed before, the radiation leakage starts contributing when $s > 2 \cdot d$.

In conclusion, this example has been presented in order to summarize the effect of the three different loss mechanisms on generic SIW components, to be considered during the design procedure.

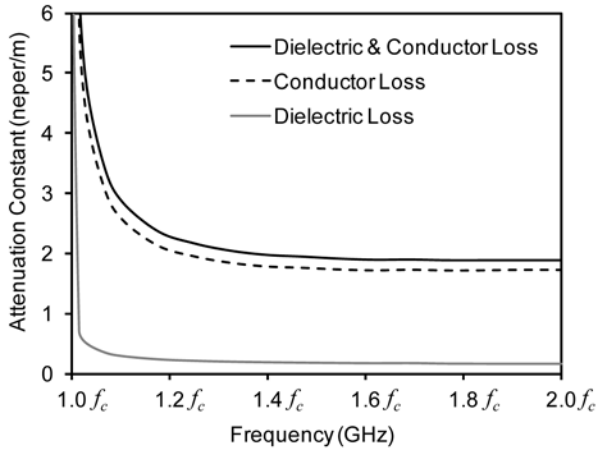

(*a*)

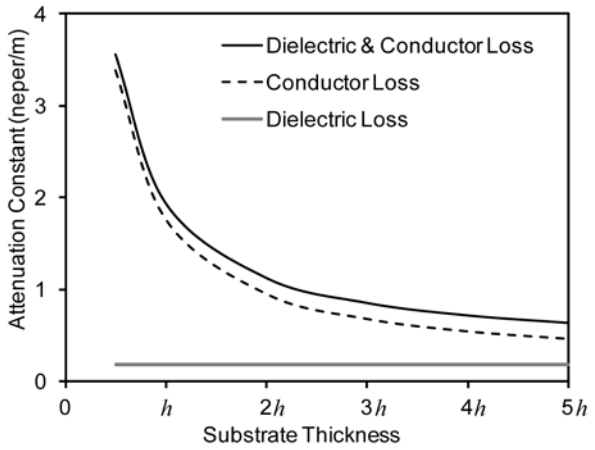

(*b*)

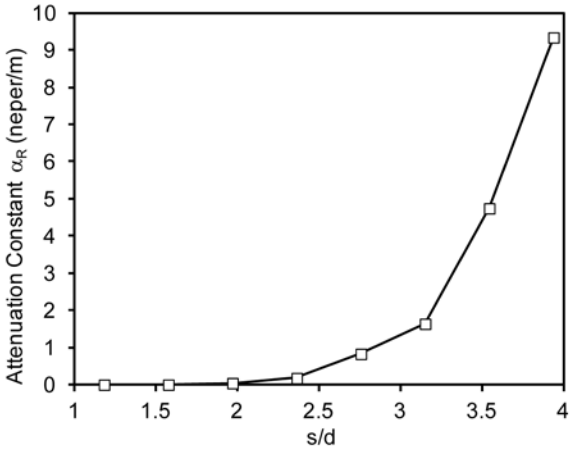

(*c*)

Fig. 8 - Study of attenuation constant in a SIW-line for the three different loss-mechanisms [3]:
(*a*) Highlight of the dielectric and conductor effects on the attenuation constant versus frequency;
(*b*) Highlight of the dielectric and conductor effects on the attenuation constant
versus substrate thickness *h* at $f=1.5\ f_c$;
(*c*) Highlight of the attenuation constant due to radiation leakage versus *s*/*d* ratio at $f=1.5\ f_c$.

I.6 The Band Gap Effect in SIW

The band gap effect is due to the periodicity of the SIW structure, that affects the propagation constant β and the length of the unitary cell s. The formula to describe this phenomenon is $\beta s = n\pi$, where n is a natural index [8]. So, the band gap effect appears when the spacing s is equal to the half of the guided wavelength. Moreover, considering the simplest case, and by substituting $n=1$, the formula is reduced to $\beta s = \pi$. Subsequently, by forcing the first band gap outside the single mode band ($f = 2f_c$) the formula is modified as:

$$\beta(2f_c) = \sqrt{{k_0}^2 - {k_c}^2} = \sqrt{4{k_c}^2 - {k_c}^2} = \sqrt{3}k_c = \frac{2\sqrt{3}\pi}{\lambda_c}$$

where λ_c represents the cut-off wavelength, and k_c the cut-off wave-number of the fundamental SIW mode. Now, by inserting $\beta s = \pi$, it is possible to obtain:

$$s = \frac{\lambda_c}{2\sqrt{3}} \qquad usually\ rounded\ as \qquad s < \frac{\lambda_c}{4} \qquad as\ design\ rule\ of\ thumb$$

Under this condition, the first band gap is centred at the cut-off frequency $2 \cdot f_c$ of the second SIW mode. Moreover, due to the finite bandwidth of the band gap, it has been noticed in [8] that also the fundamental SIW mode is moderately reduced. Eventually, a way to avoid this effect consists in selecting $s < \lambda_c/4$ (since usually $\lambda_c \cong 2w$, then $s < w/2$).

I.7 The SIW Operative Regions

Considering all the aspects mentioned in the previous Sections, it is possible to summarize all the properties required to properly design a generic SIW-line by means of only four formulas. In particular, those formulas identify the region of interest for the design of SIW structures, and set the boundaries to the undesired regions: the band gap region ($s > \lambda_c/4$), the leakage region ($s > 2d$), the not realizable region ($s < d$), and the over-perforated region ($s < \lambda_c/20$). In detail, a complete view of those regions is highlighted in Fig. 9. Specifically, this set of design rules depends exclusively on SIW geometric parameters and adopted working frequency, and it has been presented in [8]. Eventually, once fulfilled those criteria, it is possible to identify the region in the *s*-*d* plane to design a SIW-line with minimum radiation leakage and no band gap effect.

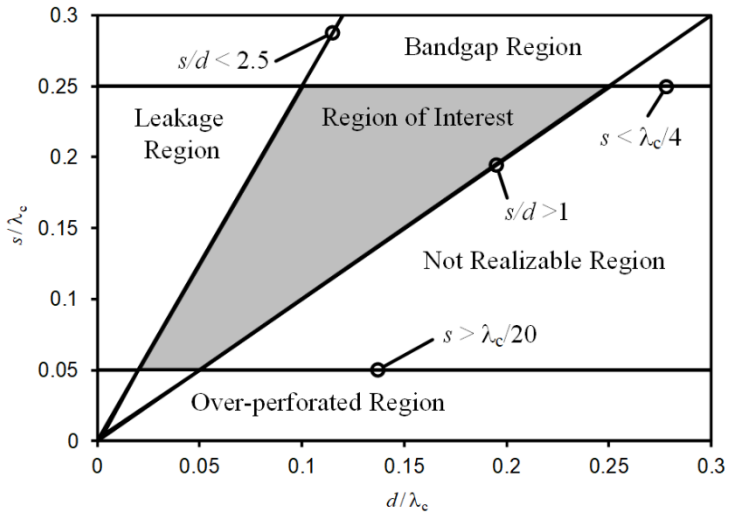

Fig. 9 - The SIW operative regions in the *d*-*s* plane (region of interest highlighted in grey).

I.8 The Transitions between SIW and other Circuitry

Several transitions between SIW and other circuitry have been investigated in the last years. Among them, a popular class is represented by the transitions between SIW and other planar transmission lines. In particular, microstrip-lines and coplanar waveguides circuits are both manufactured with the same fabrication techniques adopted for SIW components. In fact, on the same dielectric substrate it is possible to implement simultaneously these three different transmission lines, by adopting only a single fabrication process. This feature unlocks stimulating perspectives for novel hybrid circuits and systems, but at the same time requires the necessity of realizing appropriate transitions between SIW and those planar transmission lines.

Moreover, the main purpose of those transitions is to connect the SIW structure to the measurement set-up, usually composed of a vector network analyzer (VNA) and coaxial cables. Those cables are normally connected to 50-Ω planar transmission lines by means of test fixtures. Due to this reason, the input/output terminations of SIW components are generally microstrip or coplanar waveguide lines.

Another possibility, instead, contemplates the direct connection between the coaxial cable and the SIW. This solution provides significant reduction in terms of transmission losses due to the complete shielding, at the cost of slightly reduced operative fractional bandwidth. Besides, this transition also guarantees the propagation of the higher order modes, often used in the novel high frequency SIW structures.

For all those reasons, the design of transitions between SIW structures and other circuitry represents a key aspect in the development of SIW systems. The investigation on various topologies of low-cost, compact, low-losses and easy to fabricate transitions has always request the microwave engineers a significant effort. Some examples are highlighted in the next paragraphs, divided in three different Sections: the microstrip-line to SIW transition, the coplanar waveguide to SIW transition, and the coaxial cable to SIW transition.

I.8.1 The Microstrip Line to SIW Transition

This class of transitions is usually achieved by means of tapered lines, that connect the microstrip line to the SIW, thus minimizing the brutal discontinuity between them and producing a good input matching. In fact, this simple profile is possible because of the similarity between the modal fields in the two structures, that allow for a compact single layer transition. In particular, the conductor of the microstrip line is directly connected to the top metal plane of the SIW by means of a tapered microstrip section, while the ground plane of the microstrip line is directly attached to the bottom metal plane of the SIW. A detailed top view of the generic microstrip to-SIW transition is shown in Fig. 10. In this case, the tapered line assumes a triangular shape and the optimized transition is obtained by acting on both the length and the width of this tapered structure. In particular, long linear tapers, usually up to half wavelength, are required to achieve broadband input matching. Furthermore, this tapered transition is commonly adopted for the simple geometry, the ease of fabrication, the compact dimensions and the quite low insertion losses.

Specifically, the design is usually performed via the full-wave electromagnetic simulators, that allow to determine the optimal dimensions. Instead, an alternative solution [17] proposed a rigorous and analytical method to estimate the optimal dimensions via equations derived from fitting curves, thus avoiding the use of computer aided design.

In general, standard values of -20 dB are obtained for the input reflection coefficient over the full standard SIW single-mode bandwidth (conventionally defined as the frequency range from 1.25 f_0 to 1.9 f_0). Eventually, it is even possible to directly solder the connectors to the terminating part of the microstrip line and the SIW component is ready to be experimentally validated.

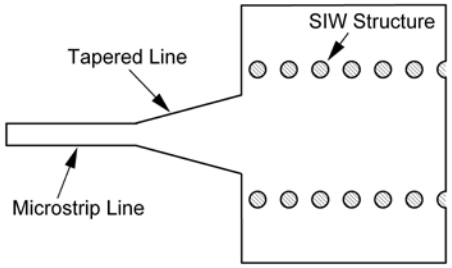

Fig 10 - Top view of the tapered microstrip line to SIW transition [3].

I.8.2 The Coplanar Waveguide to SIW Transition

In order to overcome the issue of radiation leakage, the novel coplanar waveguide to SIW transition has been introduced. In particular, the flaw of radiation losses due to the presence of fringing fields, typical of the microstrip-to-SIW transition, can be overcome adopting the coplanar waveguide to SIW transition. In fact, as demonstrated in the previous Sections, in order to reduce the conductor losses, it is beneficial to adopt thick substrates. In this case, the use of microstrip lines should be prevented, because they suffer from large radiation leakage when implemented on substrates with higher thicknesses. On the contrary, the design of coplanar waveguide is suitable with thick substrates, and the electrical parameters can be optimized practically with any substrate thickness.

Several solutions have been proposed in the scientific literature, but one peculiar example [18] is shown in Fig. 11. In this case, the top view highlights the direct insertion of the coplanar waveguide inside the SIW by means of folded 90° bends for the two slots penetrating the SIW cavity. Furthermore, the angle of those bent slots could be controlled to optimize both bandwidth and input matching, as shown in [19]. The main drawback of this transition is related to spurious radiation: in fact, due to the analogy with a centre-fed slot antenna, it is radiating both inside and outside the SIW structure. In this way, the SIW mode is excited but even undesired radiation losses are present. To overcome this issue, an alternative solution has been presented in [20], adopting an electrically thick high-permittivity substrate, and experimental validations provided a 40 % FBW with -15 dB minimum return loss and maximum 0.5 dB insertion loss around the frequency of 50 GHz. Subsequently, another example [21] exploits the usage of a current probe to implement a transition between a grounded coplanar waveguide and SIW-section.

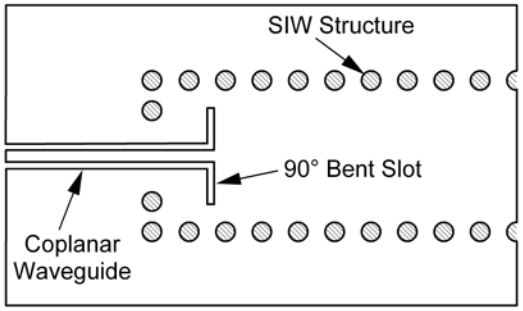

Fig 11 - Top view of the coplanar waveguide to SIW transition [3].

Regarding this approach, the operation principle can be synthesized in this way: the current vertically flowing through the probe generates a magnetic field, which matches with the magnetic field of the fundamental mode of the SIW structure. Finally, those examples conclude a brief panoramic of the possible implementations of coplanar waveguide to SIW transitions.

To summarize, coplanar waveguide to SIW transitions offer generally a 30 %, maximum 40% FBWs, significantly lower values compared to the microstrip lines to SIW transitions. Instead, in [19] it is possible to achieve an input reflection coefficient lower than -20 dB over the full single-mode SIW bandwidth, simply by adopting the conductor-backed coplanar waveguide.

I.8.3 The Coaxial Cable to SIW Transition

The necessity of exploiting different frequency bands, while simplifying the circuit geometry, reducing the fabrication costs, and maintaining the ease of manufacturing leads to the investigation of the direct coaxial cable to SIW transition. In fact, the coaxial cable is indeed able to excite various SIW modes, thus allowing the design of structures operating with higher order modes. Furthermore, it provides a total shielded connection, thus avoiding any radiation leakage.

Several transitions between coaxial cables and SIW have been proposed [22]-[29]. Among them, the most simple solution is depicted in Fig. 12, where the coaxial cable is directly inserted through a terminated SIW-line. Besides this example, generally considering the mentioned scientific contributions, modelling and experimental verifications provided fractional bandwidth spanning from 15% to 48%, when considering an input matching of -15 dB over the entire frequency band. Moreover, low levels of insertion losses are achieved due to the totally shielded configuration.

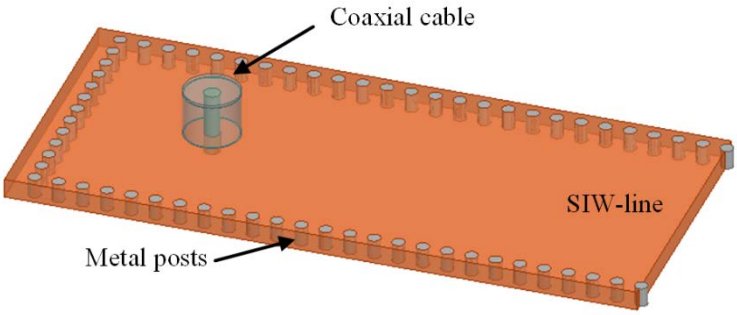

Fig. 12 - 3D view of the coaxial cable to SIW transition.

Reconsidering the solution highlighted in Fig. 12, the direct insertion of the coaxial cable inside the SIW structure enables promising results. In fact, it allows to avoid the need of extra circuitry to connect and measure the SIW component. In addition, this feature reduces the overall dimension of the system and guarantees the possibility to excite the electromagnetic field in the desired location. Eventually, to summarize, the coaxial cable does represent an excellent solution for the design of compact, low-losses and high frequency SIW devices.

I.9 Alternative SIW-line Configurations

The direct comparison between traditional planar transmission lines and SIW structures highlights two main limitations for the SIW technology: a narrower bandwidth and a not so-compact size. Basically, the SIW covers one octave and the device can be merely used in the bandwidth of the first SIW mode, spanning from the cut-off frequency f_c to the cut-off frequency of the second mode 2 f_c. Those flaws motivated the research interest in discovering alternative SIW-line configurations. Accordingly to [3], some examples are reported in the next paragraphs.

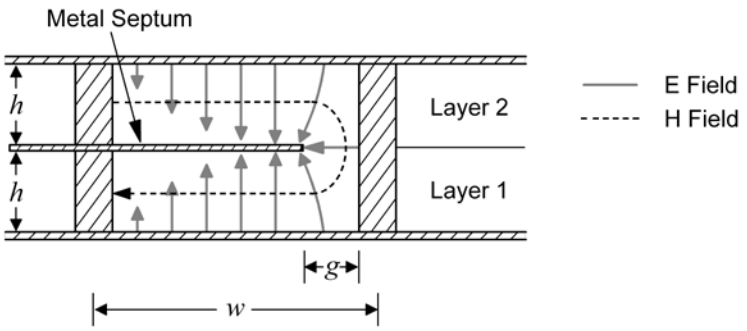

Fig. 13 - Cross-section of a generic SIFW along with electric field pattern [3].

I.9.1 The Substrate Integrated Folded Waveguide (SIFW)

The substrate integrated folded waveguide (SIFW) has been proposed for the first time in [30], and it permits to shrink the waveguide width by adopting a dual-layer substrate. In particular, this is possible simply by considering the same concept applied for the classical folded waveguide. In addition, a cross-section of a standard SIFW is presented in Fig. 13. Basically the SIFW consists of a standard SIW folded around a metal septum. Furthermore, the design criteria could be found in [31], [32]: the beneficial reducing factor could decrease two or three times the width of the SIFW with respect to the width of the SIW. In conclusion, SIFW structures presented the advantage of compact size, while maintaining a complete electrical shielding, the ease of fabrication, and exhibiting low-losses.

I.9.2 The Half-Mode Substrate Integrated Waveguide (HMSIW)

Halving the SIW structure, by cutting along the symmetry plane in the propagation direction, lead to the introduction of the novel half-mode SIW, presented in [33]. In particular, the exploited symmetry is related to the virtual magnetic wall seen by the fundamental quasi-TE_{10} SIW mode. In fact, this is possible due to the high ratio between height and width, typical in *H*-plane components, and by cutting exactly in the middle the SIW structure, the field distribution of the fundamental mode remains practically unchanged, while the width of the waveguide results halved. A detailed view of the HMSIW is highlighted in Fig. 14.

Subsequently, rigorous discussion about the characterization of the propagation properties of the HMSIW has been presented in [34]. In this work, it is even considered the presence of fringing fields near the truncated part, that slightly affect the cut-off frequency. This phenomenon could be compensated simply by modifying the width of the waveguide of a small contribute Δw. Moreover, HMSIW exhibits roughly the same losses of SIW, except in a small region near the cut-off frequency, where the open side behaves like a slot with uniform field distribution, and radiation losses are significant, as observed in [34]. Furthermore, the open side represents an excellent point to freely access the centre of the HMSIW, where it is possible to locate resonant stubs implementing transmission zeroes, where the electric field of the fundamental mode is maximum, as proposed in [35], [36].

Eventually, to further reduce the overall component size, a combination between the SIFW and the HMSIW has been presented in [37], generating the folded half-mode SIW (FHMSIW). Moreover, by exploiting the same concept of

observing symmetry planes in SIW structure, it is possible to additionally shrink the overall dimensions. For this reason, the introduction of the HMSIW has been followed by the quarter-mode SIW, the eight-mode SIW, the sixteen-mode SIW, and so on and so forth. A summary of subsequently halved SIW structures is highlighted in Fig. 15 [38], [39].

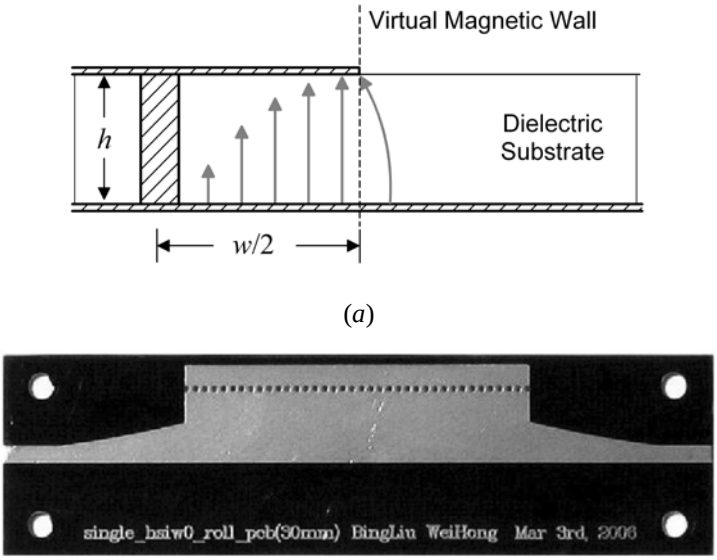

(*a*)

(*b*)

Fig. 14 - The half-mode SIW [3]:
(*a*) Cross-section view of the HMSIW along with electric field pattern;
(*b*) Photograph of the first implemented HMSIW prototype.

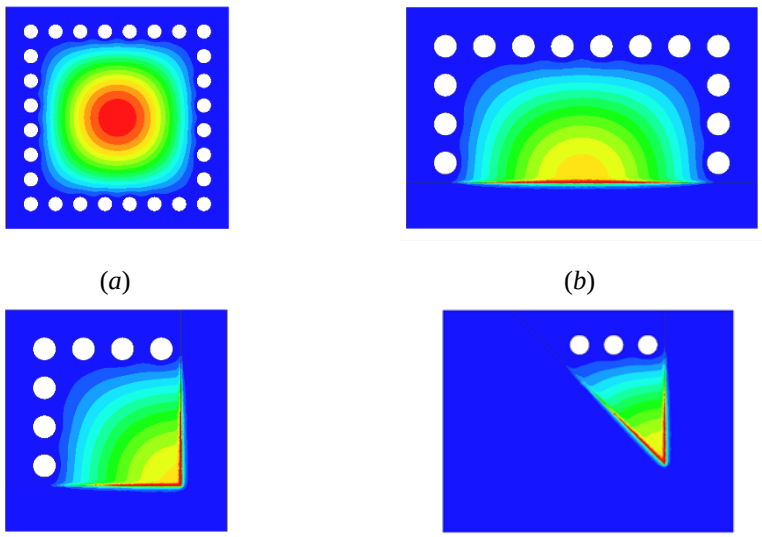

(*a*) (*b*)

(*c*) (*d*)

Fig. 15 - Miniaturization of SIW cavities [38], [39]:
(*a*) The entire SIW cavity; (*b*) The half-mode SIW cavity;
(*c*) The quarter-mode SIW cavity; (*d*) The eight-mode SIW cavity.

I.9.3 The Substrate Integrated Slab Waveguide (SISW)

In order to increase the single-mode bandwidth of the SIW, the novel substrate integrated slab waveguide (SISW) has been proposed in [40], exploiting the same concept adopted for the dielectric slab loaded rectangular waveguide. A depiction of the generic SISW-line prototype is highlighted in Fig. 16. In particular, the lateral portions of this transmission line contain air enclosures, that are reducing the effective dielectric constant ε_{eff} of the waveguide in those sections. In detail, a precise estimate for the ε_{eff} could be computed as the average mean between the dielectric constants of the left dielectric parts and the air holes, respectively. Conversely, in the central part of the waveguide the dielectric constant ε_r remains unchanged. In this way, by analysing the propagation inside the SISW, it is possible to note that the fundamental mode of the SISW (that resembles the TE_{10} of the classical rectangular waveguide) is travelling mostly in the central strip. Besides, the electric field is more concentrated in this same central portion, thus perceiving the original ε_r and presenting a cut-off frequency really similar to the one of the SIW. The air holes does not affect the propagation of the fundamental mode, instead, the second mode, the quasi-TE_{20}, is deeply affected by this geometric modification. In fact, the second SISW mode is travelling mostly in the lateral sides of the transmission line, and the effective dielectric constant is now modified by those air enclosures. The ε_{eff} constant is decreased due to the presence of air. As an immediate consequence, the cut-off frequency of the second mode is shifted upwards. In this way, the mono-modal band of the SISW is increased with respect to the one of the SIW.

Specifically, the first prototype of SISW has been presented in [41], providing a single-mode band spanning from 7.5 GHz to 18 GHz, adopting a substrate with $\varepsilon_r = 10.2$. Moreover, properly this parameter is crucial in the design of the SISW, in fact, the higher the dielectric contrast between the dielectric laminate and the air, the more significant the bandwidth enhancement with respect to the standard SIW.

Subsequently, from a technological perspective, a straightforward and simple fabrication process to implement SISW components consists of drilling the lateral portion of standard laminates, thus creating air holes next to the side rows of metal posts. This operation can be easily industrialized in standard processes, as pointed out in a recent work presenting perforated SIW filters [42]. Moreover, an alternative way to easily implement SISW structures has been presented in [43]. In this work, the additive manufacturing, also known as 3D printing technique, is adopted to construct both SIW and SIW lines and to compare their mono-modal

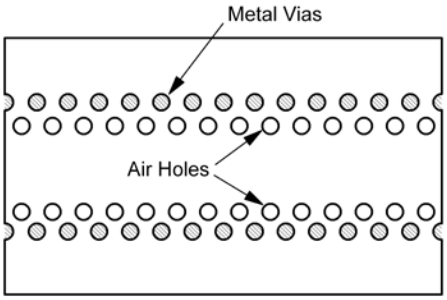

Fig. 16 - Top view of the generic SISW-line [3].

bandwidth performances, resulting in a 50 % enhancement for the SISW with respect to the SIW.

I.9.4 The Substrate Integrated Ridge Waveguide (SIRW)

Another possibility to increase the mono-mode bandwidth of the SIW is represented by the substrate integrated ridge waveguide (SIRW), that originates from the idea of the ridge waveguide, presented for the first time in [44]. In this case, by adding a ridge in the middle of the broad wall of the waveguide, it is possible to shift downward the cut-off frequency of the fundamental mode. At the same time, the cut-off frequency of the second mode remains practically unchanged. This feature can be seen as the counterpart of the idea presented in the previous Section for the SISW. At the end, in both cases, an enhancement of the single-mode SIW bandwidth is obtained.

Specifically, a prototype has been presented in [45], [46] covering the frequency band from 4.9 GHz to 13.39 GHz. Furthermore, in a following work [47], it has been demonstrated that the SIRW suffers from band gap issues, arising while adopting ridge posts with large diameters, representing a serious limitation concerning this structure. In particular, to overcome this issue, a simple metal strip should be added to connect the bottom of the ridge posts, thus totally preventing the band gap effect, as demonstrated in [47]. Furthermore, in the same work is introduced a complete list of useful criteria to design and optimize the SIRW. A prototype covering the single-mode band from 6.8 GHz to 25 GHz has been manufactured and experimentally validated. This fundamental SIRW mode bandwidth is almost three times larger than the fundamental SIW mode bandwidth.

In addition, even a width size reduction of the 40% is achieved, while comparing the *w* of the SIRW and of the SIW with the same cut-off frequency.

Additionally, from a technological perspective, the SIRW appears of more difficult implementation, due to the presence of a double layer configuration. Despite this, it allows for a broadband and compact design scenario among SIW technology. Specifically, an additional example of SIRW implemented adopting two substrates with different ε_r has been presented in [48]. In this case, the two different substrates allow to double the bandwidth of the composite SIRW with respect to the single substrate SIRW.

Eventually, it is even possible to merge the two different concepts of SISW and SIRW, creating a complex SIW component, presented in [47], achieving a huge mono-modal bandwidth spanning from 7.1 GHz till 30.7 GHz. A detailed view of the SIRW configurations with and without metal strip, along with the manufactured prototype, is shown in Fig. 17.

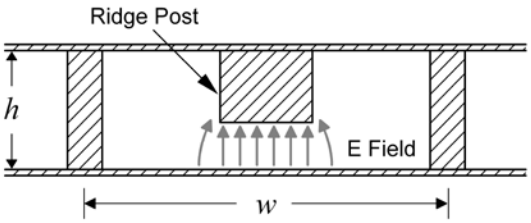

(*a*)

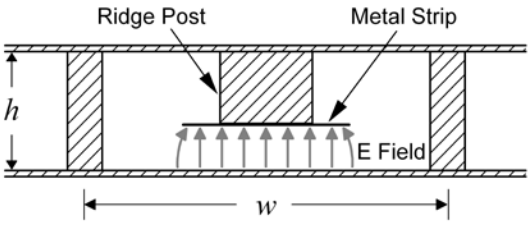

(*b*)

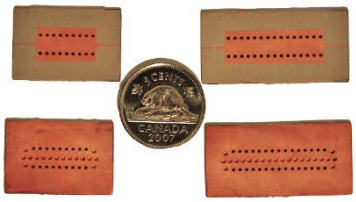

(*c*)

Fig. 17 - Substrate integrated ridge waveguide configurations [3]:
(*a*) Classical SIRW configuration without metal strip;
(*b*) Classical SIRW configuration with metal strip;
(*c*) Photograph of the manufactured SIRW prototype.

I.10 The Versatility of SIW Technology: from Components to System Perspective.

Almost all standard metallic waveguide components and antennas can be replicated adopting the SIW technology. This feature has fostered the rapid growth of various passive and active SIW circuits. Examples include passive structures like filters, directional couplers, diplexer, and multiplexers; active structures like oscillators, mixers and amplifiers; antennas like leaky-wave antennas, and array feed networks, etc. All those components have stimulated the research interest of microwave engineers, and represented a challenge in the design of performant SIW circuitry. Moreover, even the possibility to easily interconnect SIW devices with microstrip lines and CPWs in the same substrate have been widely discussed in Section I.8. In particular, properly this feature is opening interesting perspectives for the implementation of complete systems on a single substrate. In this way, the concept of the System-in-Package (SiP), widely adopted in the design of RF and microwave circuits, can be extended and gradually replaced by the paradigm of the System-on-Substrate (SoS) [49].

In detail, two major methodologies for the deployment and integration of SoS have been proposed in the recent scientific literature. The first example consists of a 24 GHz complete front-end frequency-modulation continuous-wave (FMCW) radar, presented in [50]. In particular, the circuit, shown in Fig. 18 (*a*), integrates on the same substrate several building blocks, including up-converters, down-converters, power dividers, as well as one receiving and one transmitting 16-element slotted-wave antenna array. Besides, the other methodology is based on the use of multi-chip modules, which are mounted on SIW circuits. Specifically, it consists of a 60 GHz receiver based on multi-chip modules in GaAs technology, referenced in [51], and shown in Fig. 18 (*b*).

To summarize, the SoS concept represents the ideal platform for the development of cost-effective, easy-to-fabricate and high-performance microwave and mm-wave systems, opening interesting design possibilities in the framework of the new wireless sensors networks (WNS) and Internet of Things (IoT) applications.

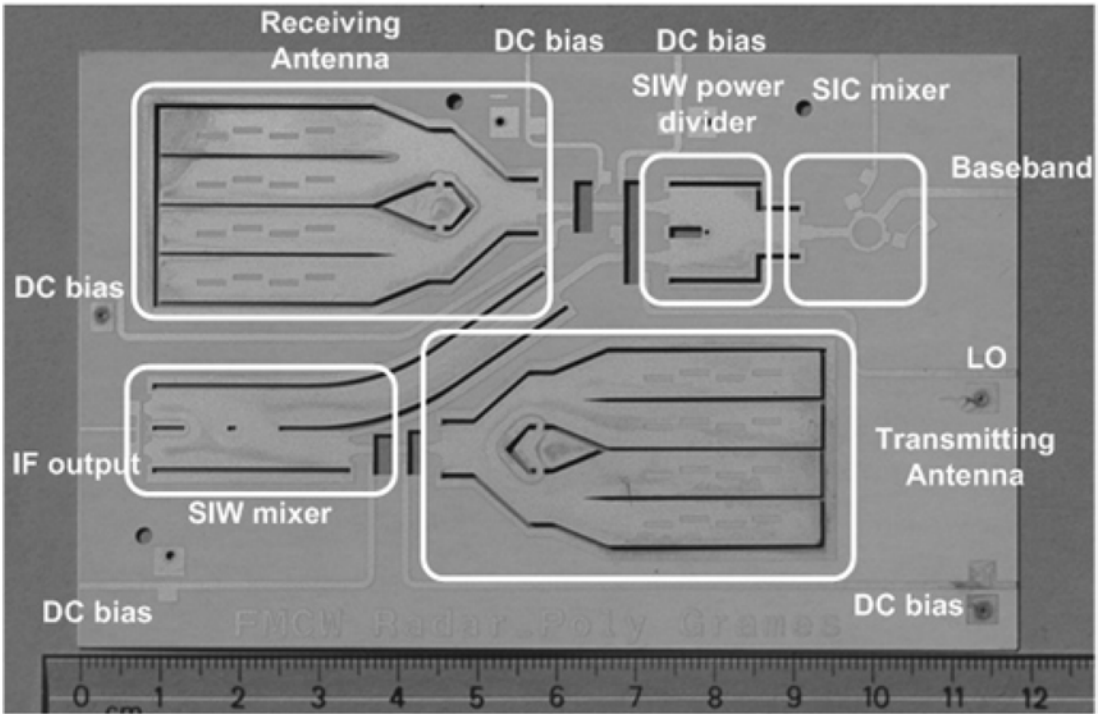

(*a*)

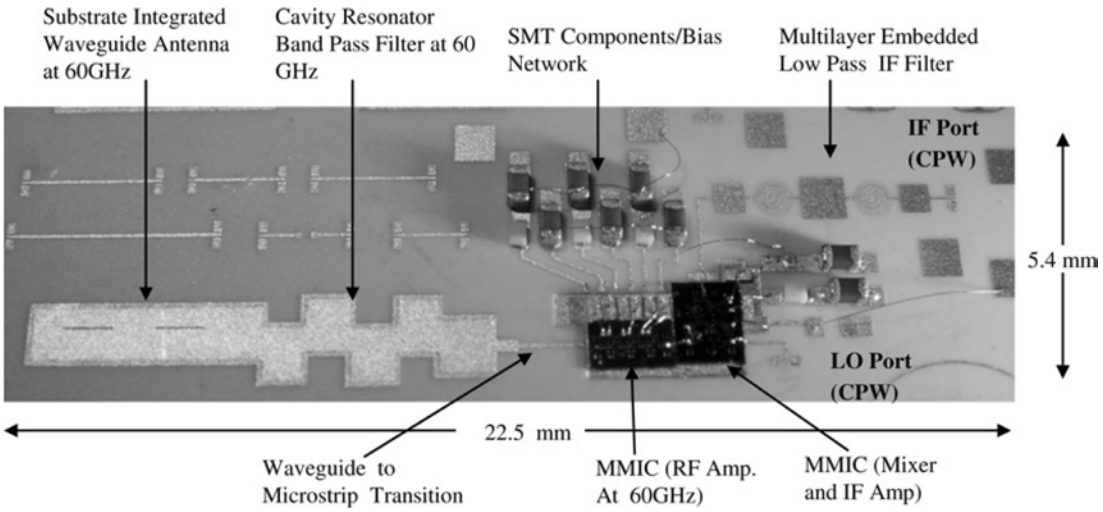

(*b*)

Fig. 18 - Examples of System-on-Substrate (SoS) integration [3]:
(*a*) 24-GHz FMCW radar front-end;
(*b*) 60-GHz multi-chip module receiver.

I.11 Materials and Fabrication for the SIW Technology

As observed in [3], the prototypes physical dimensions have a great impact on the technology choice. In fact, the large majority of SIW components operate in the frequency range between 3 GHz and 30 GHz. Only few other example have been proposed up to 60 GHz or 90 GHz, with little exceptions above 100 GHz. Specifically at lower frequency, less than 3 GHz, the SIW components exhibit large size in comparison to the operation wavelength, thus enabling easy and low cost manufacturing procedures. Moreover, at those frequencies losses are relatively small, highlighting the benefit of SIWs when compared to microstrip lines or CPWs. Conversely, at high frequencies, the challenge of fabrication tolerances represent a serious issue, and expensive and precise manufacturing procedures are required. In addition, severe transmission losses affect the electromagnetic performances of SIWs, with an important request of sophisticate technologies and dedicated materials for microwave and mm-waves applications.

In particular, the fabrication through printed circuit board (PCB) and low-temperature co-fired ceramic (LTCC) technologies represents the most popular choice [3]. Regarding the PCB manufacturing, standard substrates and commercial laminates are drilled, cut and etched via numerically controlled milling machines, both laser-based or mechanical-based, providing different realization accuracies. Subsequently, the posts are implemented through metal rivets, or directly metallized via conductive pastes or alternative metallization procedures, thus finalizing the SIW prototype. This solution provides good design flexibility, achieved through low cost materials and technologies, thus representing a popular choice also in custom designs, therefore widely adopted by the scientific community worldwide. On the contrary, LTCC is also popular in the design of SIW filters and antennas, for the possibility to realize multi-layer structures, enabling the possibility to reduce footprint sizes by means of stacked or folded cavities [52], [53].

Subsequently, another interesting approach has been proposed in [54], where silicon-based SIW structures have been developed for mm-wave applications. In particular, this solution is attractive for the possibility to integrate SIW structures with silicon-based RF and MEMS devices, opening a total new scenario in the design of microwave and mm-waves devices and systems.

In parallel, a deep investigation on novel materials represents a fascinating research topic for material scientists and designers of more and more performing SIW circuits. Besides standard commercial laminates, novel solutions have been recently proposed for the implementation of SIW devices and systems. In [55], the

use of a flexible plastic substrate has been proposed for the implementation of an SIW-based slot array antenna operating at 79 GHz, where the flexibility of this substrate opens interesting perspectives for wearable conformal circuits and antennas. Subsequently, even photographic paper has been adopted for microwave circuit applications, and conductive strips have been implemented through ink-jet printing [56], presenting the possibility to implement bio-degradable, eco-friendly, green, and extremely low-cost sensors for future microwave and mm-wave applications. In addition, another unconventional material, which is receiving attention for microwave applications, is represented by textile fabrics. An example is mentioned in [57], presenting the implementation of a wearable textile SIW antennas for rescuing applications, directly incorporated in the firefighters garments. Eventually, even the exotic super low-cost chalk powder, treated by the additive manufacturing procedure called binder jetting, has provided promising properties for the design of microwave and mm-wave devices and systems. In detail, a NRD-guide and a NRD 3-ports junctions have been presented for the very first time in [58], [59].

Last, several issues have to be considered in the design of high frequency SIW structures. Among all, the impact of considerable important transmission losses and technological constraints on manufacturing inaccuracies have to be faced and solved. In detail, a first approach has been proposed in [60], where the lateral cylindrical posts have been substituted by metalized slots, easier to be implemented at frequencies above the 60 GHz. Other alternatives have been presented and recently published in the scientific literature, with various diverse fabrication approaches. A detailed summary has been summed up in [3].

Eventually, fabrication technologies and material choice both represent a crucial point to design, manufacture and experimentally validate a new class of performing microwave and mm-waves SIW devices and systems. For this reason, the scientific interest on novel additive manufacturing procedures and novel exotic composite materials is nowadays representing an attention grabbing research topic. Moreover, it provides a lot of opportunities for a challenging design of components for the new fifth generation (5G) of wireless sensors networks (WNS) inside the Internet of Things (IoT) scenario.

Chapter 1

Substrate Integrated Waveguide (SIW) Interconnects

The versatility of SIW technology, as highlighted in the Introduction, allows to replicate almost all kind of standard metallic waveguide components and antennas, combining the advantageous properties of both classical planar and non-planar microwave structures [3], as mentioned in Section I.1. In particular, this feature has fostered a rapid growth in the design, manufacturing and experimental validation of different passive and active SIW circuits [3]. Exactly inside this context, the possibility to implement complete systems-on-substrate (SoS), combining various and diverse SIW devices in the same physical prototype, has been presented and discussed in Section I.10. Specifically for those applications, there is a crucial need of compact, efficient, and high performance interconnects [61]-[63]. Particularly in this scenario, the researchers attention has been focused on exploiting both novel materials and fabrication technologies [3]. Specifically, easy, cost-effective and flexible manufacturing procedures are required to implement the novel class of microwave and mm-waves systems [3]. All those features are suggesting to adopt the additive manufacturing techniques: in fact, the 3D printing is able to satisfy all those requirements, providing a final prototype in a fast and cost-effective way, through an easy, flexible and not so expensive fabrication process. Moreover, the 3D printing technology can also accommodate the requirements of flexible, light-weight, and eco-friendly devices, required by the rapid development of the next generation of wireless sensors networks toward the Internet of Things (IoT) paradigm [64]-[68]. In parallel, a deep investigation on novel printable materials is solicited. Indeed, to efficiently design a competitive microwave system, it is extremely important to adopt a material with excellent electromagnetic properties. To this aim, the study of the electrical properties (dielectric constant and loss tangent factor) of 3D printable materials represents the first project phase in the

design of pioneering microwave components [69], [70]. To summarize, the new frontiers of the microwave research include the study of additive manufacturing techniques, also known as 3D printing methodologies, together with the investigation about the electrical properties of original 3D printable materials.

Furthermore, regarding this work, a brief historic overview on alternative SIW-line configurations, like SIFW, HMSIW, SISW, and SIRW has already been presented in Section I.9, with the aim of improving the classical SIW electromagnetic performances. In particular, special attention has been focused on the SISW-line, that consists of a slight modification of the standard SIW interconnect, and provides a wider mono-modal bandwidth [43]. Specifically, by adopting the Fused Deposition Modelling (FDM) 3D printing technique, and the commercial thermoplastic polyurethane Ninjaflex® filament, both SIW and SISW interconnects have been designed, fabricated and tested [43], to prove the bandwidth enhancement and to pave the road to a future implementation of innovative, light-weight, flexible, and low-cost microwave devices and systems.

This Chapter is organized as follows. At first, the 3D printing technology is introduced, along with a detailed overview on its features and potentialities, especially suited for microwave design. In particular, a special attention has been addressed to the Fused Deposition Modelling (FDM) technique, that allows for a simple, fast, and low-cost implementation of fully three-dimensional prototypes. Subsequently, an investigation on the thermoplastic polyurethane Ninjaflex®, a commercial FDM-printable material, has been widely discussed. Specifically, the electrical properties of the filaments have been retrieved adopting two different methodologies: the waveguide-based narrow-band setup, and the microstrip lines broadband setup, thus demonstrating the suitability of the Ninjaflex® for microwave designs. Following, the design, fabrication and experimental verification of both SIW and SISW interconnects have been highlighted, demonstrating the potentialities of 3D printing and providing a 50 % single-mode bandwidth enhancement, thus paving the road to a future implementation of FDM 3D-printed microwave devices and systems.

The achieved results have been collected and published in [43], [70].

1.1 The 3D Printing Technology

The Additive Manufacturing (AM) procedures, also known as 3D Printing technologies, are becoming increasingly relevant for the implementation of the next generation of wireless sensors networks and the Internet of Things (IoT) [64], [66]. In fact, besides providing rapid prototyping and low fabrication costs, they offer also an unprecedented flexibility and a completely novel design scenario for the manufacturing of microwave components and systems.

In particular, the use of 3D printing represents an emerging class of manufacturing processes, where materials are deposited, usually layer upon layer, to create objects from 3D models. Due to this feature, it is possible to realize the most complex and strange geometries, with fully three-dimensional shapes, that are difficult or impossible to implement adopting standard fabrication procedures. Those characteristics are achieved only by additive manufacturing procedures, that deposit selectively the printable material in the desired volumetric regions, thus creating the final solid object in compliance with the designed geometry. On the contrary, they are opposed to subtractive manufacturing technologies, where material is removed to shape the final objects. An ordinary example is represented by the numerically controlled milling machines, that can realize shapes only removing external materials. In particular, they are commonly used to pattern the metal layers of the standard commercial laminates, thus creating planar microwave components. Conversely, this limitation is indeed overcome by the novel additive manufacturing procedures, that are opening the design scenario to fully three-dimensional structures.

In addition, several 3D printing technologies can adopt diverse materials to implement complex structures. In particular, both dielectrics and metals can be 3D-printed, but using separate processes and different machines. Still, at the time of writing, a complete system able to print both dielectric and metal parts in the same project phase, with reasonable accuracy for microwave applications, is missing. In fact, the bulky metals are commonly printed using very expensive machinery based on laser sintering procedures [65], [67]. Instead, less expensive facilities are available for a large selection of printable dielectrics.

Nevertheless, a standard definition for AM procedures has not been clearly proposed by the large scientific community yet. Only the American Society for Testing and Materials (ASTM) suggested the following sentence to define the AM procedures: “A process of joining materials to make objects from 3D model data, usually layer upon layer, as opposed to subtractive manufacturing methodologies”.

Moreover, the same society classified the AM techniques introducing seven different classes:

- "Binder Jetting": a liquid bonding agent is selectively deposited to join powder materials;
- "Direct Energy Deposition": focused thermal energy is used to melt materials as they are being deposited (Beam Deposition Process);
- "Material Extrusion": material is selectively dispensed through a nozzle or orifice (Fused Deposition Modelling - FDM);
- "Material Jetting": droplets of build materials are selectively deposited (3D inkjet printing);
- "Powder Bed Fusion": thermal energy selectively fuses region of a powder bed (Electron Beam Melting, and Selective Laser Melting);
- "Sheet laminations": sheets of material are bonded to form an object;
- "Vat Photo-Polymerization": liquid photopolymer in a vat is selectively cured by light-activated polymerization (Stereo-litography).

Most of these techniques have been adopted to fabricate microwave and mm-wave components and systems. A brief overview is presented in the next paragraphs, starting with the Fused Deposition Modelling (FDM) technique, that will be adopted for the study of both SIW and SISW 3D-printed interconnects.

Specifically, a particular attention is dedicated to the Fused Deposition Modelling (FDM) technique, due to its high popularity among microwave designers. In fact, the FDM allows to print a huge variety of both standard and exotic plastic filaments, like the commercials acrylonitrile butadiene styrene (ABS), the polylactic acid (PLA) and flexible or eco-friendly composite materials. Moreover, another feature of the FDM consists on the possibility to vary selectively the infill percentage of the deposited material. In this way, enabling the unique opportunity to tune the 3D-printed material electrical properties, simply by modifying the quantity of the extruded material, thus achieving the final implementation of totally three-dimensional structures. A more detailed investigation about this technology will be presented in the next Section 1.1.1, and experimental results for SIW and SISW interconnects highlighted in the following Sections.

Subsequently, the Binder Jetting technique has been considered. In particular, this technology works with a printing tray filled with a dedicated powder, that solidifies in presence of a specific liquid binding agent. Peculiarly, this binding

agent is used to bond the powder together in order to create the final desired three-dimensional geometry. A lot of applications especially inside the medical field (e.g. orthopaedics, oto-surgery, and maxillofacial surgery, prostheses, …) adopt binder jetting technology in conjunction with chalk powder [71]-[73]. However, this technique has never been applied to realize microwave devices, to the best of authors' knowledge, and at the time of writing. An investigation, for the very first time, has been proposed in [58], [59]. The chalk powder, 3D-printed via binder jetting, has been adopted to design, manufacture and experimentally validate a Non Radiative Dielectric (NRD)-guide, and a NRD 3-ports junction, respectively.

Furthermore, even 3D printing by means of photo-polymerization, adopting dedicated laser sintering procedures, represents an efficient technique to treat special plastic materials. In addition, it permits to create fully three-dimensional structures, with extremely precise accuracies (in the order of the μm, in particular of 20 μm in [74]). In this way, all the classical microwave components can be manufactured in a cost-effective and personalized mode. Peculiarly, in [74], a two-poles bandpass filter, a four-poles bandpass filter, a SMA to waveguide adapter, a plastic horn antenna, and an helical resonator have been designed, manufactured and tested, demonstrating the validity of the vat photo-polimerization 3D printing technique, applied to microwave design.

Besides, classical microwave waveguide components have been 3D-printed also through a Selective Laser Melting (SLM) additive manufacturing procedure [75], achieving performing results even around the operative frequency of 20 GHz. In particular, two selective components, a fifth-order and a sixth-order microwave filters with complex 3D geometries, have been designed, fabricated and tested, proving the validity of this AM approach for the design of passive microwave components.

In addition, even the possibility to fabricate millimetre wave components and interconnects for communications and sensing applications by 3D/inkjet printed technologies has been presented in [76]. In particular, microstrip patch antennas, lens antennas, interconnections and array have been designed, fabricated and validated through this novel approach, paving the road for the implementation of innovative, low-cost wireless sensors networks (WSN) class of microwave devices for the fifth generation (5G) and the Internet of Things (IoT) applications.

Eventually, 3D printing is recently gaining increasing popularity in a variety of applications, from anatomical models to building constructions, and it represents a kind of third industrial revolution, where industry and production are based on a completely new model [67], [68]. In fact, initially, 3D printing was mainly

exploited for rapid prototyping, with the aim of testing designs before starting the final production. Instead, nowadays, 3D printing technologies have rapidly evolved towards the complete manufacturing of end-use components. Furthermore, in this context, inside the field of microwave components and systems, even the possibility to embed wireless systems into everyday life objects has opened interesting perspectives for the development of the Internet of Things [77].

To summarize, this concludes the panoramic overview on the state of the art about the 3D printing technology and its applications to microwave and RF engineering. Subsequently, a detailed description of the FDM technique is highlighted in the following Section, with the aim of better understanding the potentialities offered by this additive manufacturing procedure, for the fabrication of novel 3D-printed SIW and SISW microwave devices and systems.

1.1.1 The Fused Deposition Modelling Technique

Among all the different 3D printing procedures, the Fused Deposition Modelling (FDM) technique is one of the most common additive manufacturing techniques. Moreover, due to its features, the FDM represents also one of the most promising approach for printing thermoplastic polymeric materials for applications in the radio frequency (RF) and microwave frequency ranges. In detail, the working principle of this technology consists of an extrusion-based 3D printing technique, where a thermoplastic filament is heated and then extruded from a nozzle. Specifically, two-dimensional layers of printable plastic material are selectively deposited by the extruder. The pre-heated and melted material solidifies immediately after being extruded from the nozzle, thus forming the geometry set by the machine. Eventually, at the end of the fabrication procedure, the 3D-printed structure is formed by several overlapped two-dimensional layers, that constitute the final fully three-dimensional prototype. Furthermore, from an industrial point of view, this technology is simple and cost-effective, both when considering materials and facilities. Instead, from a technical perspective, affords quite good printing resolutions: commercial prototypes commonly deposit layers with height ranging between 50 μm and 300 μm, and present typical planar resolution of 10-20 μm with a vertical accuracy down to 20 μm. In addition, a unique feature of FDM is the capability of changing the density of the 3D-printed material. In fact, the infill percentage could be nominally varied from 100 %, that represents a complete dense structure, to 0%, that means a completely hollow structure. Due to this reason, FDM represents a very popular 3D printing technique, that allows to play with the infill percentage of deposited material, thus enabling the possibility

to modify the dielectric characteristics of the printed material, leading to fascinating microwave design possibilities. Last, FDM even allows for the implementation of fully three-dimensional structures, with extremely low cost materials and in one single pass fabrication process, paving the road to the manufacturing of a future class of performing 3D-printed microwave devices and systems.

Specifically, in this work, the thermoplastic polyurethane Ninjaflex® filament, with diameter 1.75 mm, has been adopted and 3D printed through a commercial LeapFrog Creatr 3D printer (Fig. 1), by using the Fused Deposition Modelling (FDM) technique together with the slicing software is Slic3r [www.slic3r.org]. In detail, this machine is equipped with two direct extruders that can be heated up to 260 °C, and nozzles of diameter $d = 0.35$ mm. Moreover, the glass bed temperature can reach 85 °C. Furthermore, such a printer is especially suitable when printing low modulus filaments as thermoplastic polyurethanes. Finally, some specifications are reported for sake of completeness: build volume of 23 x 27 x 20 cm^3, minimum layer height $h_{min} = 50$ μm, maximum layer height $h_{max} = 350$ μm, *xy*-precision of 0.05 mm, and printing speed of 10-60 mm/s. This standard facility has been adopted in the realization of all prototypes presented along this communication.

1.2 The Characterization of 3D Printable Dielectric Materials

In order to perform accurate full-wave electromagnetic simulations, the electrical properties of the 3D printable dielectric materials need to be estimated in a precise way. In particular, to fully describe the electromagnetic performances of a generic medium it is sufficient to consider the dielectric permittivity ε_r and the loss tangent $\tan\delta$. To this aim, the electromagnetic characterization of the 3D-printed material has been performed by adopting two different techniques. The former is based on the usage of a classic metallic waveguide, and provides accurate but narrow-band values. Instead, the latter is based on the implementation of microstrip lines with different lengths on a 3D-printed substrate, and provides broadband information. Indeed, the combination of these two techniques offers a complete description of the electrical properties of the 3D printable dielectric material.

Eventually, in the following Sections, both narrow-band and broadband methodologies will be illustrated, providing almost identical results for a complete electromagnetic characterization of the considered 3D printable dielectric material. In addition, in the last Section, an alternative methodology will be mentioned, and referenced in detail in Appendix 1.

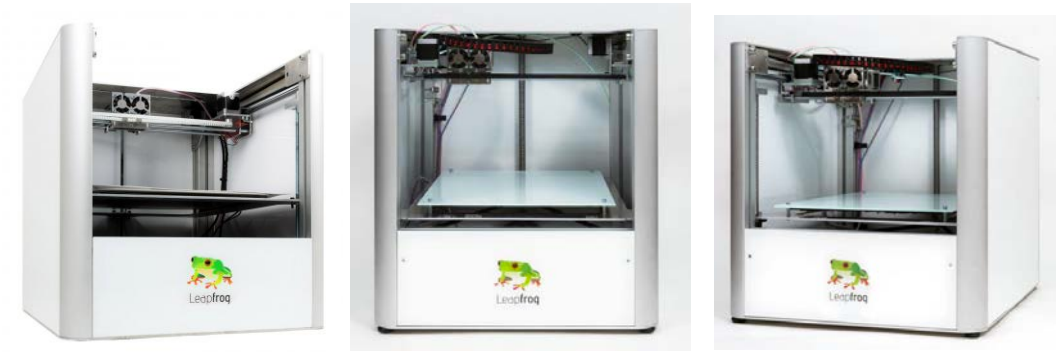

Fig. 1 - Photographs of the commercial LeapFrog Creatr 3D printer adopted in this work.

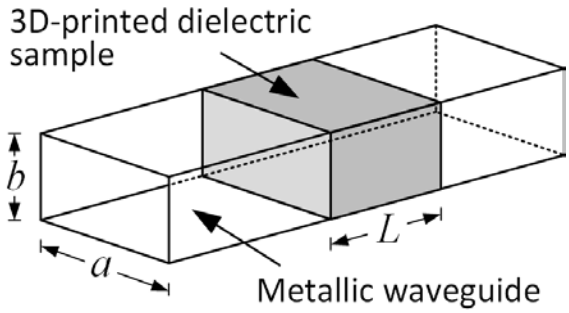

(*a*)

(*b*)

Fig. 2 - Narrow-band dielectric characterization [43], [70]:
(*a*) Schematic drawing of the measurement setup for waveguide-based material characterization;
(*b*) Photograph of 3D-printed dielectric samples with different infill percentages
(from left to right, nominal values of 100%, 50% and 25%).

TABLE I

NARROW-BAND MEASUREMENTS OF THE DIELECTRIC CHARACTERISTICS OF 3D-PRINTED MATERIAL

	Infill percentage	ε_r	tanδ
Sample 1	95.5%	3.18	0.052
Sample 2	95.8%	3.13	0.047
Sample 3	93.8%	3.13	0.042

1.2.1 The Waveguide (Narrow-band) Characterization

The measurement setup for the narrow-band characterization of the printable material simply consists of a hollow metallic waveguide, where the 3D-printed dielectric samples must be inserted in, one at a time. A minimal schematic drawing of the proposed system is shown in Fig. 2 (*a*).

In particular, the testing procedure appears straightforward and immediate. In fact, starting from the measurements of the scattering parameters, both ε_r and $\tan\delta$ can be retrieved for the analysed specimens. In detail, the dielectric permittivity is calculated from the half-wavelength resonance frequency inside the waveguide, thus inherently providing narrow-band results. For this reason, the retrieved value is theoretically valid only at that precise frequency (in practice, it can be assumed effective in a small frequency band around that resonance frequency). Subsequently, the loss tangent is obtained from the difference of the insertion loss with and without the dielectric sample inserted in the waveguide setup.

Regarding this work, the thermoplastic polyurethane Ninjaflex® filament, with diameter 1.75 mm, 3D-printed via FDM technique, has been investigated, retrieving its electrical properties. At first, a set of dielectric specimens, with different infill percentages, and nominal length $L = 20$ mm, have been realized by 3D printing. In particular, the photograph, reported in Fig. 2 (*b*), highlights three 3D-printed bricks with nominal infill percentage of 100 %, 50 % and 25 %, respectively. However, for initial testing purposes, only three 3D-printed samples with nominal 100 % infill factor have been considered, to estimate the electrical properties of the completely dense printed material. At this point, it is worth specifying that the actual value of the infill has been estimated from the volume and the weight of each specimen, and it resulted approximately 95 %, for the three considered samples. Instead, the nominal infill percentage value refers to the parameter imposed during the 3D printing procedure. In order to summarize, retrieved data are reported in Table I. Moreover, measurements have been performed in the *X*-band (8 - 12 GHz), by adopting a standard metallic WR-90 rectangular waveguide ($a = 22.86$ mm, $b = 10.16$ mm). Furthermore, the sample size $L = 20$ mm has been chosen because it provides a half-wavelength resonance at the frequency of 9.8 GHz. Eventually, on average, the retrieved values of the relative dielectric permittivity and loss tangent of these samples are close to $\varepsilon_r = 3.15$ and $\tan\delta = 0.047$, respectively, at the frequency of 9.8 GHz. Finally, a limited spread of the measured data can be appreciated considering the exact values reported in Table I.

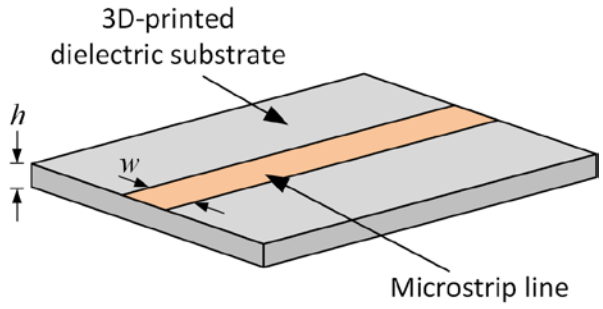

(*a*)

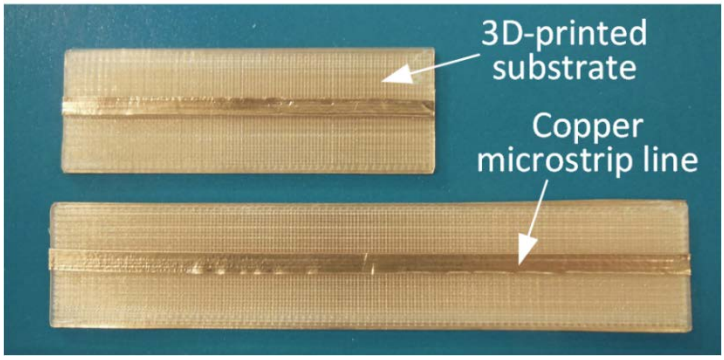

(*b*)

Fig. 3 - Broadband dielectric characterization [43], [70]:
(a) Schematic drawing of the measurement setup for microstrip-based material characterization;
(b) Photograph of the two microstrip lines with different lengths (L_1 = 59 mm and L_2 = 98 mm), realized on 3D-printed dielectric substrate.

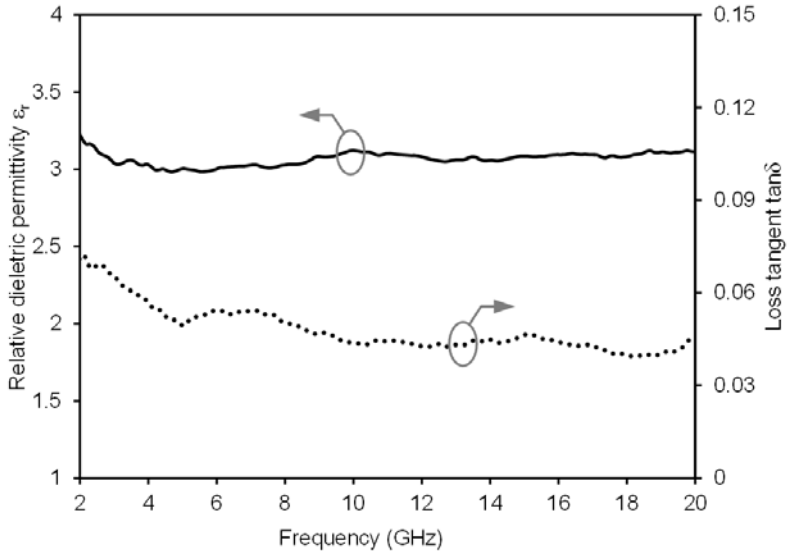

Fig. 4 - Broadband measurements of the dielectric characteristics (dielectric permittivity ε_r and loss tangent tanδ) for the 3D-printed material thermoplastic polyurethane Ninjaflex® filament, with diameter 1.75 mm [43].

1.2.2 The Microstrip Lines (Broadband) Characterization

In order to extent the validity of the electrical properties, for the 3D-printed material, in a wider frequency range, the use of a microstrip lines approach is required. In particular, for this work, it allowed to perform a broadband material characterization over the frequency band from 2 GHz to 20 GHz. A detailed three dimensional drawing of a microstrip line is highlighted in Fig. 3 (*a*), along with its crucial dimensions: the height *h* and the strip width *w*.

In particular, for testing purposes, two microstrip lines have been fabricated. The 3D-printed substrate is realized by using the same material mentioned in Section 1.2.1: the thermoplastic polyurethane Ninjaflex® filament, with diameter 1.75 mm, 3D-printed via FDM technique, with nominal 100 % infill factor. Subsequently, a commercial adhesive copper tape has been pasted on both substrate faces, to implement the metal strip and the ground plane of the microstrip line. Specifically, the thickness of the 3D-printed substrate is $h = 1.12$ mm and the width of the microstrip line has been set equal to $w = 2.5$ mm, in order to obtain $50\,\Omega$ characteristic impedance. This last assumption originates from the narrow-band values, retrieved in Section 1.2.1. In fact, the calculation of the impedance value requires the a priori knowledge of the dielectric relative permittivity constant. In particular, as for typical dielectric laminates, it is possible to assume a rather flat ε_r along the entire frequency band of interest. Eventually, this feature allows to use the ε_r previously retrieved for the computation of the microstrip line characteristic impedance. Finally, to complete the design, two microstrip lines of lengths $L_1 = 59$ mm and $L_2 = 98$ mm, respectively, have been manufactured. A photograph of both prototypes is shown in Fig. 3 (*b*).

Once the fabrication is completed, the relative dielectric permittivity ε_r and the dielectric loss tangent $\tan\delta$ have been calculated along the guidelines of [78]. In particular, the retrieved values over the entire frequency band are shown in Fig. 4, and, as previously mentioned, exhibit a rather constant behaviour over the entire frequency band. In detail, the permittivity and loss tangent values, at the frequency of 9.8 GHz, well agree with the ones obtained by using the previous methodology (namely, $\varepsilon_r = 3.12$ and $\tan\delta = 0.045$ in this case, compared to $\varepsilon_r = 3.15$ and $\tan\delta = 0.047$ with the waveguide method).

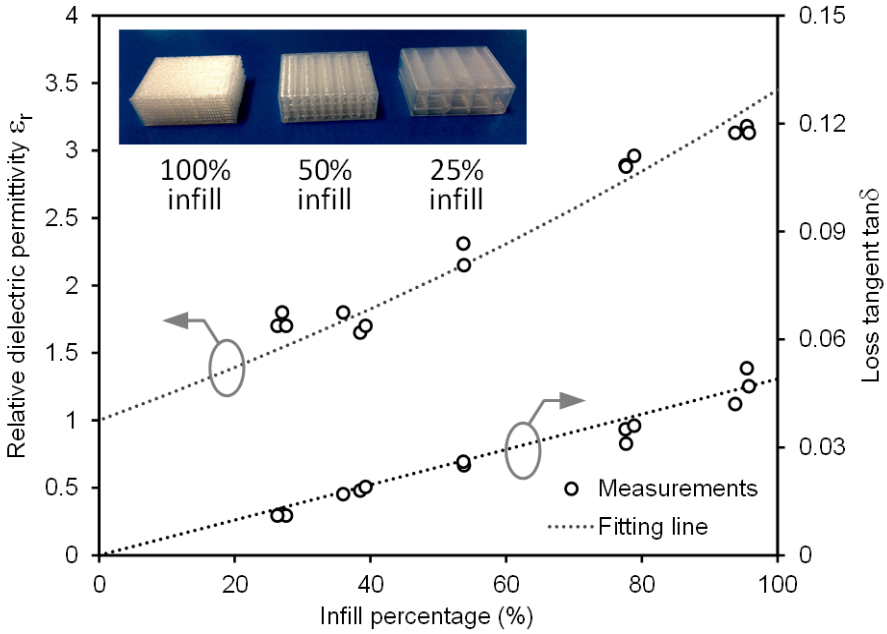

Fig. 5 - Narrow-band material characterization of dielectric permittivity and loss tangent versus different infill percentages. The 3D-printed material is the thermoplastic polyurethane Ninjaflex®, and the adopted technique is the waveguide measurement set-up [43].

1.2.3 A Detailed Study on the Variation of the Infill Percentage

As observed in the previous Sections, a unique feature of FDM is the capability of varying the printed material density, by simply changing the infill percentage, nominally from 100% to 0%, that means a completely hollow structure [43], [79], [80]. For this reason, a detailed investigation on the 3D-printed Ninjaflex® specimens dielectric characteristics, with different infill percentages, has been considered. In particular, a set of samples, with infill ranging from a minimum nominal value of 25 % to a maximum nominal value of 95 %, have been manufactured. A sub-set has already been shown in Fig. 2 (*b*). Subsequently, those samples have been measured, adopting the waveguide approach described in Section 1.2.1. Eventually, measured results (dotted symbols) for the relative dielectric permittivity ε_r and for the dielectric loss tangent $\tan\delta$ are shown in Fig. 5, versus the infill percentage. In detail, for every infill percentage considered, three samples have been fabricated and tested. Furthermore, the measured values (dotted symbols) well arrange around the fitting curve (dashed lines), obtained through the Maxwell-Garnett equation [81].

Finally, the possibility of tuning the dielectric permittivity and the loss tangent, by playing with the infill percentage, opens interesting perspectives for novel microwave components, potentially with reduced losses. In particular, a wide spread of different devices can be realized playing with the infill percentage, from sophisticated step-impedance SIW filters [42] to double-sided SISW leaky-wave antennas [82]. Definitely, those considerations have been applied in the design of the prototypes presented in this work. Indeed, all these structures, manufactured via classical subtractive procedures, could be replicated via 3D printing, reducing costs and opening towards a fully three-dimensional project scenario for a novel class of microwave and RF systems.

1.2.4 Other Material Characterization Methodologies

Besides the waveguide (narrow-band) and the microstrip lines (wideband) characterization methodologies, several different techniques are available to estimate the electrical properties of unknown materials. In particular, some examples include: coaxial probes measurements, free-space procedures, transmission-lines techniques, and cavity resonators methods. Specifically, those techniques have been summarized in [83]. Among them, the cavity resonators are particularly suitable for narrow-band, and highly accurate characterization. Moreover, the implementation of cavity resonators is particularly convenient in substrate-integrated waveguide (SIW) technology, which allows for low-cost solutions and relatively high quality factor [84]. Several implementations have already been proposed in SIW technology [85]-[90]. Still, the sensitivity proposed by those sensors in order to estimate the electrical parameters is not enough precise, motivating the research interest in finding innovative solutions to solve this problematic issue.

Driven by those observation, I proposed an inventive configuration for an enhanced and original SIW cavity sensor to better estimate the electrical properties of unknown materials. Moreover, this solution preserves the material intact, being a non invasive characterization methodology. The achieved results are summarized in Appendix 1, and published in [91].

1.3 The 3D-Printed SIW and SISW Interconnects

The recent engineering research trends encourage to exploit 3D printing possibilities in order to create innovative and low-cost microwave components, as observed in the previous Sections. Moreover, the additive manufacturing

procedures allow for a fully three-dimensional design, where the non-planar structure can assume the most strange and complicated shapes, opening a wide new scenario for the implementation of microwave systems. In addition, the FDM technique permits also to modify the infill percentage of the deposited material, thus providing the opportunity to tune the dielectric properties of the 3D-printed materials. This feature is crucial, and can be used to selectively control the dielectric constant only by acting on a single material, thus enabling the design of microwave filters or other components where different ε_r are required, but avoiding the necessity to resort to different commercial laminates to implement a single device or system. In addition, at the same time, it is possible to drastically reduce the loss tangent factor, thus providing the opportunity to fabricate systems with low transmission losses, or antennas with increased efficiency. For those reasons, the 3D printing via FDM technique has been widely considered for the implementation of microwave and mm-wave devices and systems. However, at first, an investigation on printable materials dielectric properties is required, as highlighted in the previous Sections, and, subsequently, the design of simple interconnects on both SIW and SISW technologies have been examined and demonstrated, laying the foundation for a future class of FDM 3D-printed microwave systems.

Specifically regarding this work, the adopted 3D printable material is the thermoplastic polyurethane Ninjaflex® filament, with diameter 1.75 mm, printed through the LeapFrog Creatr 3D printer, by using the Fused Deposition Modelling (FDM) technique, as observed in previous Sections. Besides, the electrical properties have been already retrieved in Section 1.2, by using two different methodologies: the waveguide-based narrow-band setup, and the microstrip lines broadband setup, thus demonstrating the suitability of the Ninjaflex® for microwave designs. Nevertheless, it offers also an outstanding a design flexibility, without precedents, due to its mechanical properties. In particular, it is flexible and it presents a tensile elongation at break of 660%, that means it can be stretched and elongated almost 7 times before reaching a breaking point. Those features, in combination with the fabrication characteristics, have been efficiently exploited to create innovative 3D-printed SIW and SISW interconnects.

Properly considering this brand new scenario, a first investigation on the basic components is required before moving forwards with the design of complex devices and systems. For this reason, at first, the study of simple interconnects have been considered. In particular, a classical SIW and a broadband SISW based on the 3D-printed material, previously presented, have been designed, fabricated and experimentally validated, in order to compare their bandwidth performance. The achieved results are summarized in the following Sections.

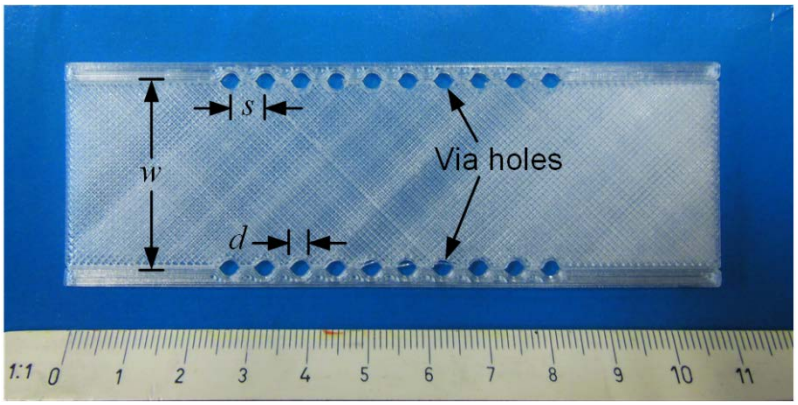

Fig. 6 - Photograph of the 3D-printed SIW interconnect with nominal 100% infill percentage, prior to the pasting of the adhesive aluminium foils, and prior to the insertion of the metallic lateral copper rivets [43].

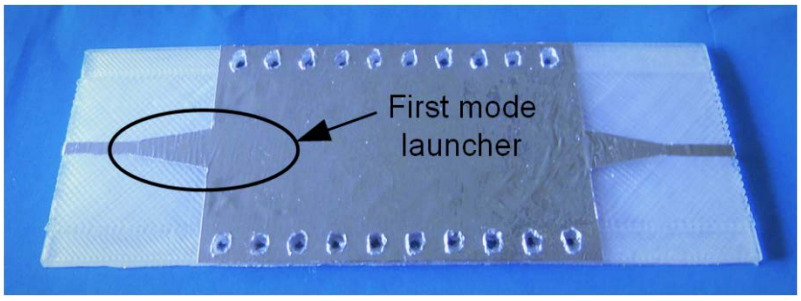

(*a*)

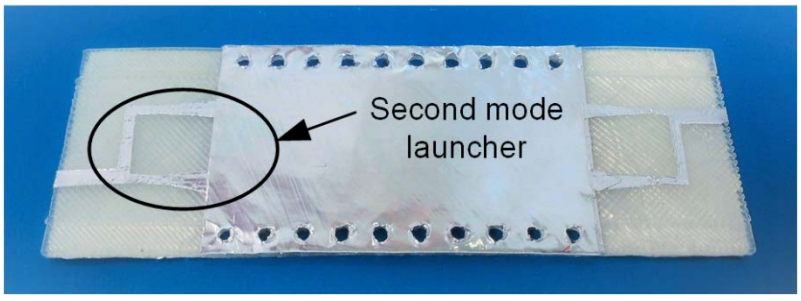

(*b*)

Fig. 7 - Photographs of the final 3D-printed SIW interconnects with 100% infill percentage, after pasting the adhesive aluminium foils, but prior to the insertion of the copper rivets [43]: (*a*) Prototype for the excitation of the fundamental quasi-TE_{10} SIW mode; (*b*) Prototype for the excitation of the second quasi-TE_{20} SIW mode.

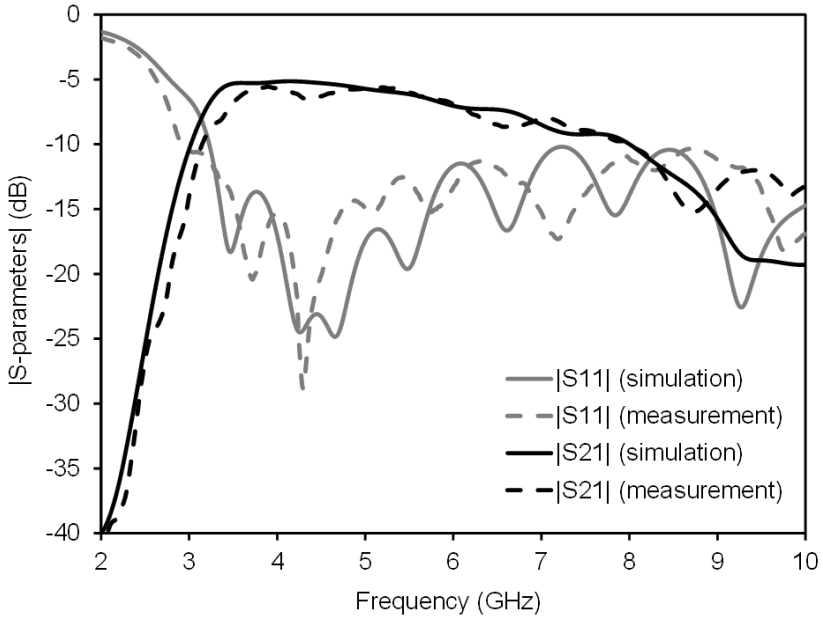

(*a*)

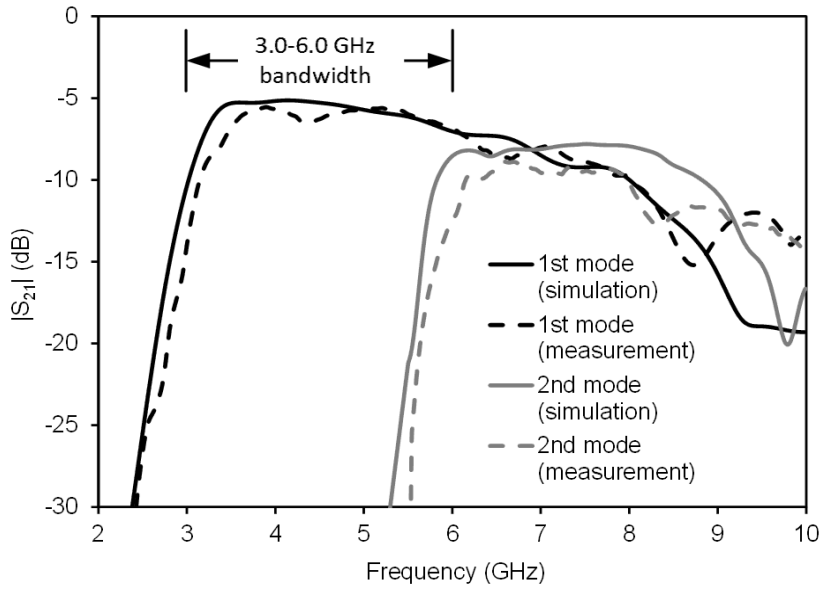

(*b*)

Fig. 8 - Simulated (continuous lines) and measured (dashed lines) scattering parameters versus frequency for the 3D-printed 100% infill SIW interconnect:
(*a*) Fundamental quasi-TE_{10} SIW mode characterization;
(*b*) Transmission parameters for both fundamental quasi-TE_{10} and second quasi-TE_{20} SIW modes.

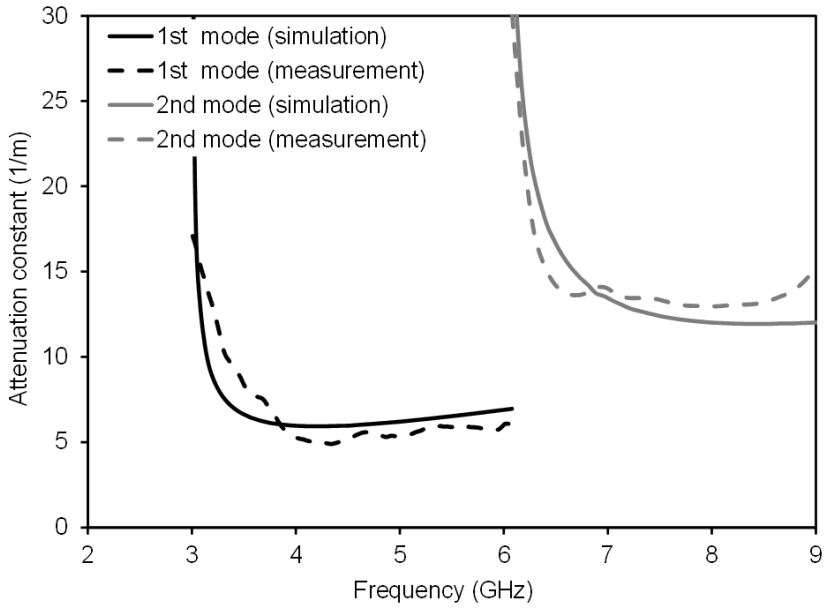

(*a*)

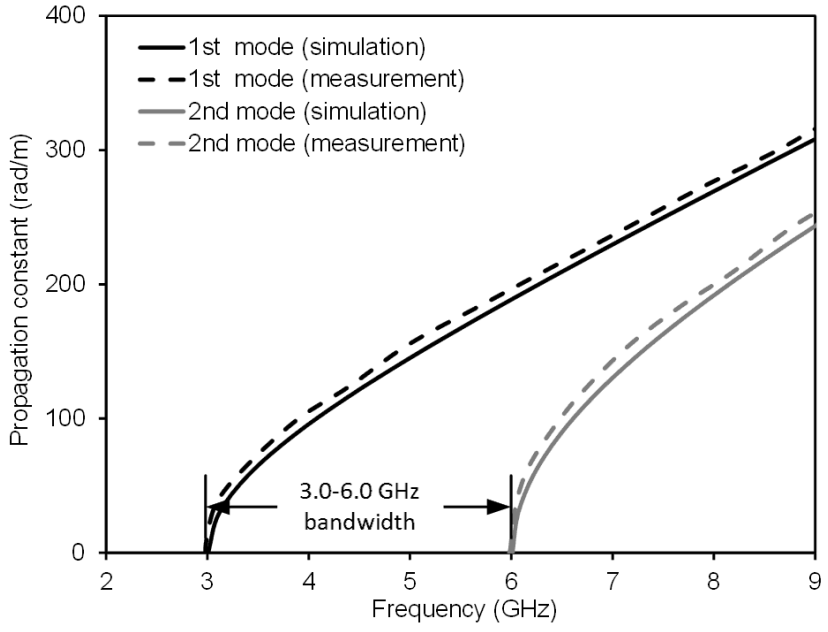

(*b*)

Fig. 9 - Dispersion characteristics of the fundamental quasi-TE_{10} and second quasi-TE_{20} modes of the 3D-printed 100% infill SIW interconnect [43]:
(*a*) Simulated (continuous lines) and measured (dashed lines) attenuation constants;
(*b*) Simulated (continuous lines) and measured (dashed lines) propagation constants.

1.3.1 The 3D-Printed SIW Interconnect

This Section is dedicated to the design, fabrication and testing of a 3D-printed SIW interconnect. A photograph of the manufactured prototype, prior to the pasting of the adhesive aluminium foils, and prior to the insertion of the metallic lateral screws, is shown in Fig. 6, along with its main geometric parameters: the width *w*, the post diameter *d*, and the spacing between adjacent posts *s*.

At first, the SIW has been designed adopting the 3D printable Ninjaflex® material, with nominal 100% infill percentage, and with dielectric constant $\varepsilon_r = 3.15$ and loss tangent $\tan\delta = 0.05$. Moreover, as a project requirement, it has been chosen a cut-off frequency of 3 GHz, for the fundamental quasi-TE_{10} SIW mode. In particular, to satisfy this condition, the modal analysis of the unit cell leads to the following optimized geometrical dimensions: w = 32 mm, d = 3 mm, s = 6 mm (Fig. 6), thus resulting in a single-mode band spanning from 3.00 GHz to 6.00 GHz. Specifically, all those analyses have been performed through the use of the commercial software Ansys HFSS.

Subsequently, adopting the LeapFrog Creatr 3D printer with it properties listed in Section 1.1, two prototypes of a 3D-printed SIW interconnect have been manufactured with a substrate thickness $h = 1$ mm. Subsequently, both top and bottom metal layers of the SIW structure have been implemented by pasting commercial adhesive aluminium foils. In addition, metallized posts have been realized directly screwing copper rivets inside the holes, constituting the lateral walls of the SIW interconnect, as in [69].

Afterwards, for measurement purposes, two different tapered microstrip to SIW transitions have been adopted. In particular, the former allows to launch the fundamental quasi-TE_{10} SIW mode, as highlighted in Fig. 7 (*a*). It consists of a simple tapered microstrip line, directly connected to the centre of the SIW-line. Instead, the latter permits to launch the second quasi-TE_{20} SIW mode, as shown in Fig. 7 (*b*). This structure is more sophisticated, and it implements a balanced power divider with 180° output phase shift, implemented to verify the exact position of the cut-off frequency for the second quasi-TE_{20} SIW mode.

Successively, simulated (continuous lines) and measured (dashed lines) scattering parameters versus frequency, related to the mono-modal bandwidth of the SIW interconnect, have been reported in Fig. 8 (*a*). The pretty good agreement between the represented curves validates the simulated predictions. Specifically for the input matching, the $|S_{11}|$ curve is well maintained under -12.5 dB both in simulation and measurement, inside the entire operative frequency band. Instead,

concerning the transmission, the considerable losses ($|S_{21}|$ always less than -5.5 dB in the entire frequency band) are mainly attributed to the significant high $\tan\delta$ of the Ninjaflex®. This concern suggested a further investigation on novel materials with lower loss tangent factors, that the rapid development of the 3D-printed applications market was able to propose, but, in a successive date with respect to this publication.

Besides, to assess the bandwidth performance, the transmission parameters for both the fundamental quasi-TE_{10} and the second quasi-TE_{20} SIW modes have been reported in Fig. 8 (*b*). Even in this case, the pretty good agreement between measured (continuous lines) and simulated (dashed lines) curves leads to the validation of the prototypes. In particular, the mono-modal SIW bandwidth of 3 GHz has been confirmed, from f_{c1} = 3 GHz, the cut-off frequency of the fundamental quasi-TE_{10} SIW mode, to $f_{c2} = 2 \cdot f_{c1} = 6$ GHz, the cut-off frequency of the second quasi-TE_{20} SIW mode.

Eventually, to complete the experimental verification of the SIW interconnect, the investigation on the dispersion characteristics has been presented. In detail, the attenuation and propagation constants have been experimentally determined following the technique described in [92], that allows the de-embedding of the transitions effect. In particular, this technique requires to compare the scattering parameters of two structures, totally similar except for exhibiting different lengths. To this aim, two 3D-printed SIW interconnects of nominal lengths 60 mm and 48 mm, respectively, have been fabricated and tested. Simulated (continuous lines) and measured (dashed lines) dispersion curves of the first and second modes of the SIW structure are shown in Fig. 9, highlighting a single-mode bandwidth of 3 GHz. Specifically, Fig. 9 (*a*) highlights the attenuation constant values for both SIW modes of the 100% infill SIW interconnection, while Fig. 9 (*b*) shows the propagation constant values, thus confirming the mono-modal SIW bandwidth of 3 GHz, from $f_{c1} = 3$ GHz to $f_{c2} = 2 \cdot f_{c1} = 6$ GHz, as previously noted in the scattering parameters outcomes of Fig. 8.

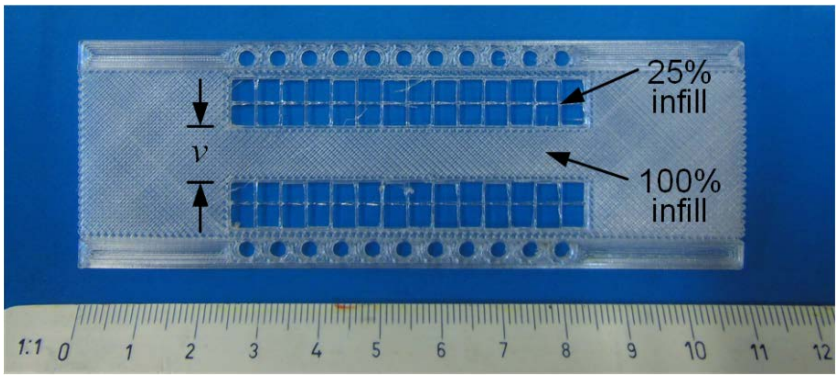

Fig. 10 - Photograph of the 3D-printed SISW interconnect with nominal 100 % infill percentage (central portion) and nominal 25 % infill percentage (side portions), prior to the pasting of the adhesive aluminium foils and prior to the insertion of the metallic lateral copper rivets [43].

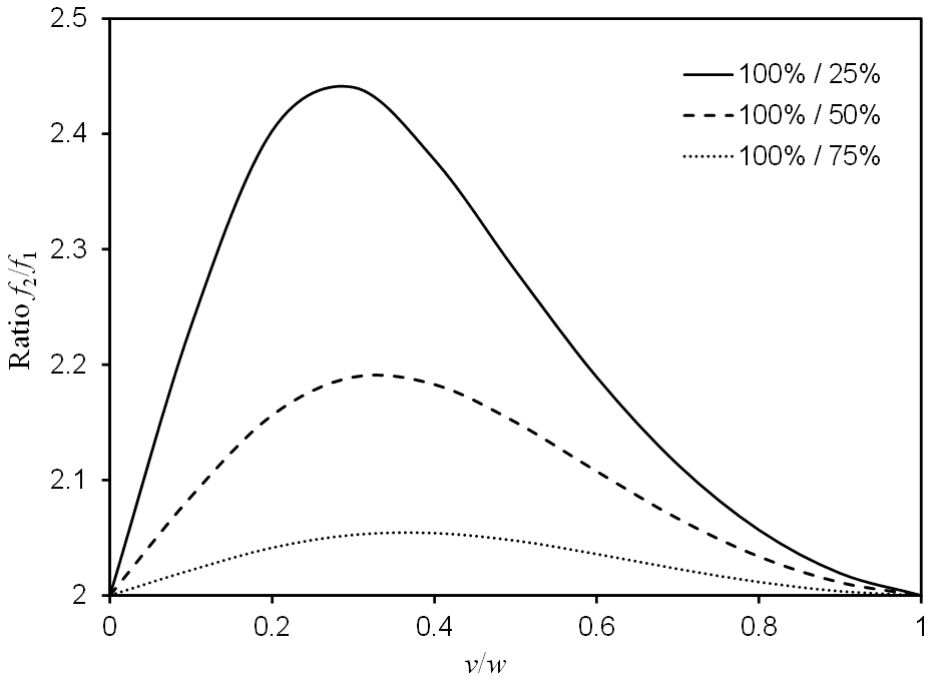

Fig. 11 - Simulation of the ratio between the cut-off frequency of the second quasi-TE_{20} and fundamental quasi-TE_{10} SISW modes (f_2/f_1) versus width v of the central portion (normalized to w), for different values of the infill percentages of the lateral portions [43].

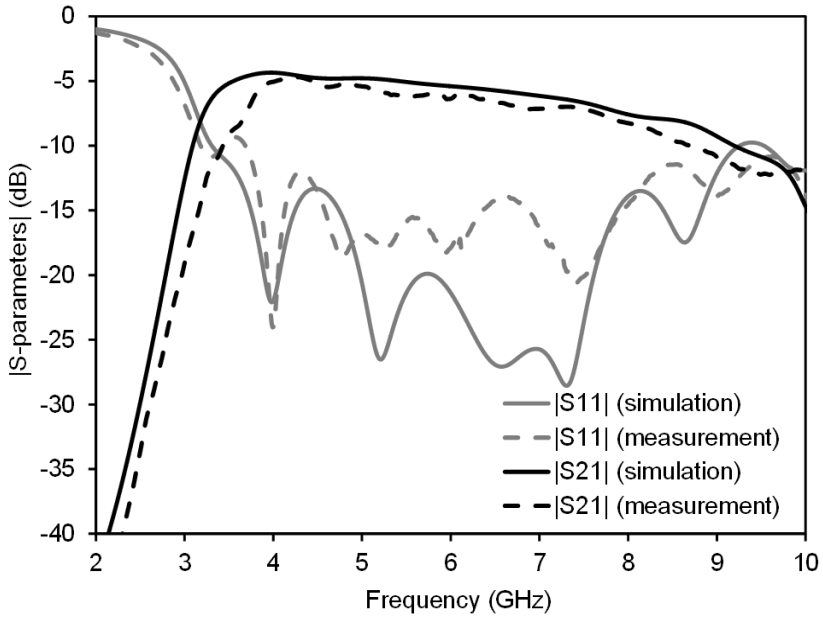

(*a*)

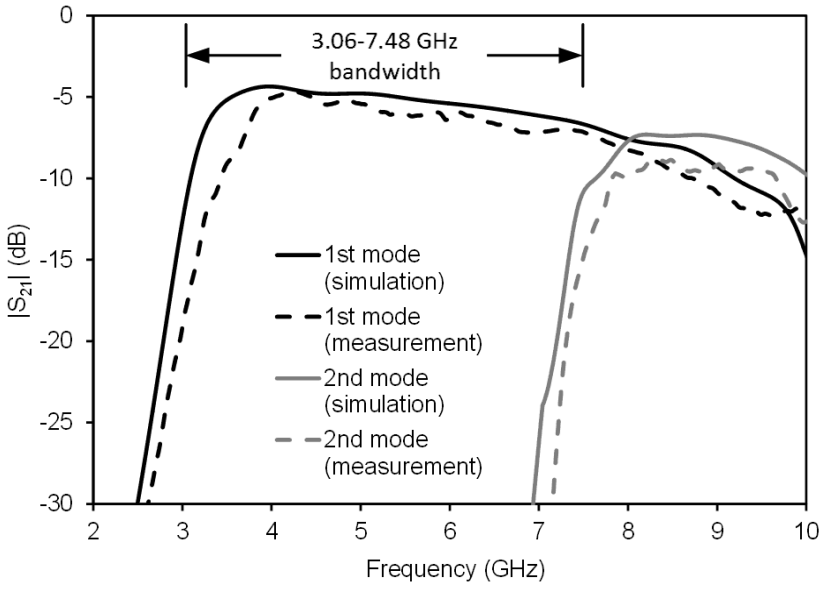

(*b*)

Fig. 12 - Simulated (continuous lines) and measured (dashed lines) scattering parameters versus frequency for the 3D-printed SISW interconnect:
(*a*) Fundamental quasi-TE_{10} SIW mode characterization;
(*b*) Transmission parameters for both fundamental quasi-TE_{10} and second quasi-TE_{20} SIW modes.

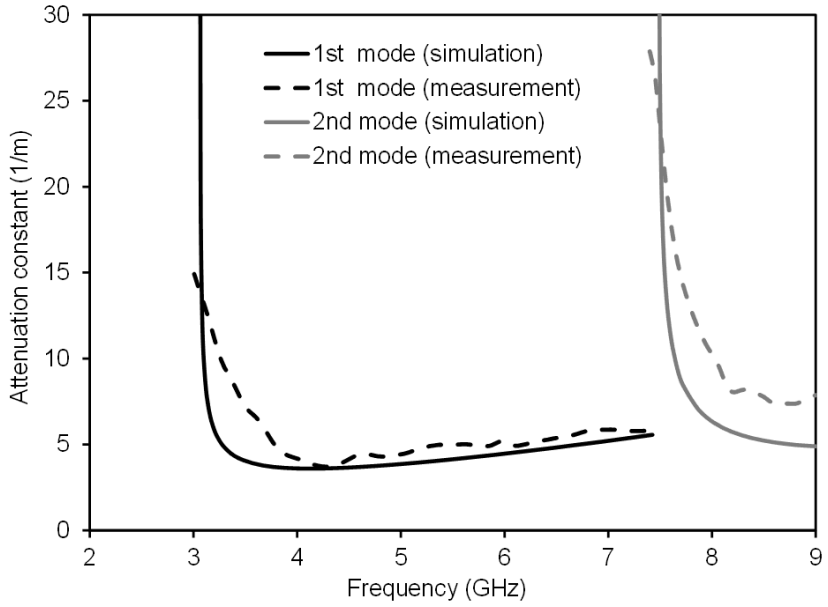

(*a*)

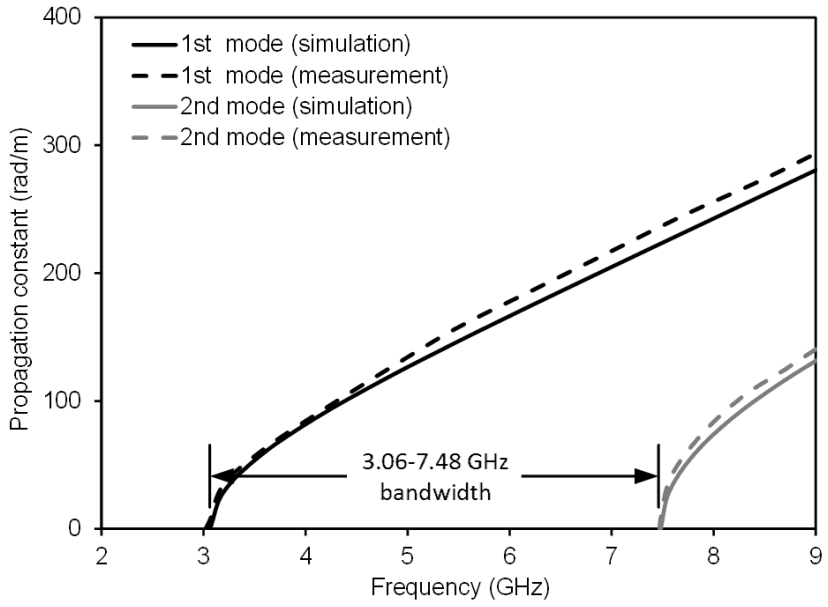

(*b*)

Fig. 13 - Dispersion characteristics of the fundamental quasi-TE_{10} and second quasi-TE_{20} modes of the 3D-printed SISW interconnect [43]:
(*a*) Simulated (continuous lines) and measured (dashed lines) attenuation constants;
(*b*) Simulated (continuous lines) and measured (dashed lines) propagation constants.

1.3.2 The 3D-Printed SISW Interconnect

In a similar way to Section 1.3.1, this Section is dedicated to the design, fabrication and testing of a 3D-printed SISW interconnect. As a remind, the geometric properties and the working principle of the substrate integrated slab waveguide (SISW) have been already presented and discussed in Section I.9.3. To summarize, this configuration represents a slightly modified version of the conventional SIW structure and it is commonly used to increase the single-mode bandwidth, that represents the goal of this dissertation. A photograph of the manufactured prototype, prior to the pasting of the adhesive aluminium foils, and prior to the insertion of the metallic lateral screws, is shown in Fig. 10, along with its main geometric properties. In detail, the SISW consists of a central portion, of width *v*, with high-permittivity material (in this case, 100 % nominal infill, i.e., $\varepsilon_r = 3.15$ and $\tan\delta = 0.05$) and two side portions with low-permittivity material (25 % nominal infill, i.e., $\varepsilon_r = 1.70$ and $\tan\delta = 0.01$) [43].

In particular, similarly to the previous case, the design of the SISW interconnect has been performed through the commercial software Ansys HFSS. Specifically, in order to directly compare this novel SISW prototype with the previous SIW line, the cut-off frequency of the fundamental quasi-TE_{10} mode has been set around 3 GHz. Afterwards, in order to justify that the adopted geometric dimensions and the selected dielectric properties represent the optimum case in term of bandwidth enhancement, a parametric study has been carried out via HFSS simulations and highlighted in Fig. 11. In particular, Fig. 11 depicts the ratio (f_2/f_1) between the cut-off frequency of the second quasi-TE_{20} mode f_2 and the cut-off frequency of the fundamental quasi-TE_{10} mode f_1 versus the width *v* of the central portion of the SISW (normalized to the total width *w*), for different values of the lateral portions infill percentage. In this way, the ratio (f_2/f_1) indicates the bandwidth extension, while the width *v* indicates the dimension of the inner 100 % infill septum, with respect to the lateral portions, because it is normalized to the total width *w*. Moreover, in the same graphs even the information about dielectric properties of the adopted materials are included. In fact, the inner septum, as a design requirement, is fabricated with 100 % infill percentage, in order to provide the maximum dielectric constant, as observed in Section I.9.3. Instead, the choice of the dielectric constant of the lateral sides represent a degree of freedom for this project, and it is achieved by varying the infill percentage, that inherently leads to the possibility of tuning the dielectric properties, as a peculiar outstanding feature of the FDM technology. In addition, it is worth noting that for null value of the ratio between *v* and *w* ($v/w = 0$), that means $v = 0$, in other words representing the 100 % infill SIW interconnect, or when those values coincide ($v/w = 1$), that indicates the

same case, the ratio f_2/f_1 is set equal to two, so the cut-off frequency of the second quasi-TE_{20} mode is doubled with respect to the cut-off frequency of the fundamental quasi-TE_{10} mode, confirming the previously studied case for the SIW interconnect where $f_1 = 3$ GHz and $f_2 = 6$ GHz, as known from the SIW theory. Furthermore, in all other cases, the ratio f_2/f_1 exceeds this value, thus leading to a bandwidth improvement with respect to the SIW line case. Besides, simulations demonstrate that the single-mode bandwidth increases by decreasing the infill of the lateral portions, and that an optimal width *v* exists. Specifically, considering the peak of the black continuous curve of Fig. 11, the maximum mono-modal bandwidth is achieved for a 25% nominal infill of the lateral portions (i.e., $\varepsilon_r = 1.70$ and $\tan\delta = 0.01$) and a width $v = 8.4$ mm; resulting in a single-mode band spanning from $f_1 = 3.06$ GHz to $f_2 = 7.48$ GHz. Consequently, the use of the SISW topology leads to a 50 % enhancement of the single-mode bandwidth performance with respect to the SIW interconnect.

Successively, the same analyses adopted for the SIW line, on the scattering parameters versus frequency, has been reconsidered for the SISW interconnect. In particular, simulated (continuous lines) and measured (dashed lines) curves have been reported in Fig. 12. First, the mono-modal SISW bandwidth has been highlighted in Fig. 12 (*a*). Also in this case, the pretty good agreement between the represented curves validates the simulated predictions. Specifically for the input matching, the $|S_{11}|$ curve is well maintained under -15 dB in simulation, and under -12.5 dB in measurement, respectively, inside the entire operative frequency band. Furthermore, even if transmission losses are lowered, with respect to the SIW solution, the $|S_{21}|$ curve presents considerably high values around -5 dB, once again due to the significant high $\tan\delta$ of the Ninjaflex®. As previously mentioned, a fresh investigation about novel composite printable materials have been considered for subsequent works.

Moreover, to assess the bandwidth performance, the transmission parameters of both the fundamental quasi-TE_{10} and the second quasi-TE_{20} SISW modes have been reported in Fig. 12 (*b*). Even in this case, the good agreement between measured (continuous lines) and simulated (dashed lines) curves leads to the validation of the prototypes. In particular, the mono-modal SIW bandwidth of 3 GHz has been extended by the novel mono-modal SISW bandwidth of almost 4.5 GHz. Peculiarly, the cut-off frequency of the fundamental quasi-TE_{10} SISW mode $f_{c1}' = 3.06$ GHz, and the cut-off frequency of the second quasi-TE_{20} SIW mode $f_{c2}' = 7.48$ GHz, provide a mono-modal SISW bandwidth of 4.42 GHz, almost 50% times larger than the mono-modal SIW bandwidth of 3 GHz.

Finally, to complete the experimental verification of the SISW interconnect, the investigation on the dispersion characteristics has been presented. In detail, the attenuation and propagation constants have been experimentally determined as in Section 1.3.1, considering the de-embedding of the transitions effect. Moreover, even in this case, a couple of 3D-printed SISW interconnects of nominal lengths 60 mm and 48 mm, respectively, have been fabricated and tested. Simulated (continuous lines) and measured (dashed lines) dispersion curves of the first and second modes of the SISW structure are shown in Fig. 13, highlighting a single-mode bandwidth of 4.42 GHz. Specifically, Fig. 13 (*a*) highlights the attenuation constant values for both SISW modes, while Fig. 13 (*b*) shows the propagation constant values, thus providing a mono-modal SISW bandwidth of 4.42 GHz, from $f_{c1}' = 3.06$ GHz to $f_{c2}' = 7.48$ GHz, as previously noted in the scattering parameters outcomes of Fig. 12. Eventually, this result proved the bandwidth enhancement of the SISW line with respect to the SIW interconnect.

1.4 Conclusions

This Chapter presented the design, fabrication and testing of 3D-printed SIW interconnects. In particular, both SIW and SISW lines have been 3D-printed via the FDM technique. Moreover, by adopting the thermoplastic polyurethane Ninjaflex® filament, with diameter 1.75 mm, and the LeapFrog Creatr 3D printer in conjunction with the slicing software Slic3r it is possible to implement fully three-dimensional and cost-effective prototypes, suited for microwave applications. Eventually, to summarize, the characterization of the printable dielectric material, the validation of the FDM process, and the testing of two SIW interconnects have been proposed as a technological demonstrator for a novel class of RF, microwave, and mm-wave 3D-printed components and systems.

Specifically, in the first part, the investigation of the 3D-printed material dielectric properties has been performed via both narrow-band (waveguide-based setup) and broadband (microstrip lines setup) characterization methodologies. In detail, the dielectric permittivity and the loss tangent of the Ninjaflex® TPU have been determined over the frequency band from 2 GHz to 20 GHz, providing suitable values for microwave designs. In parallel, the variation of the infill percentage, special feature provided by the FDM technique, allows to control the dielectric permittivity and loss tangent of the 3D-printed dielectric material. Measured results showed a good agreement with the predictions of the Maxwell-Garnett equation. Particularly, those experimental outcomes paved the road to the implementation of

novel microwave components, based on the local variation of the dielectric permittivity, and suggested a technique to effectively reduce dielectric losses.

Subsequently, SIW and SISW interconnects have been designed through HFSS simulations, 3D-printed adopting the material and the technology previously examined, and experimentally validated. Furthermore, considering the framework of the ever-increasing interest for the SIW technology, the possibility to implement novel broadband interconnects by 3D printing represents a remarkable innovation, towards fully integrated and shielded microwave systems. In particular, considering this work, the proposed 3D-printed SISW interconnect covers a mono-modal bandwidth 50% wider than the standard SIW line bandwidth. Besides the broader operation bandwidth, the interesting characteristic of the proposed waveguide is the possibility to implement the structure in one-pass fabrication and using only one single TPU filament. Finally, while nowadays losses of 3D-printed structures are still large, many composite and innovative materials are currently under development for 3D printing applications, which are expected to exhibit significantly lower losses in the near future.

In conclusion, this Chapter proved the possibility to print fully three-dimensional SIW prototypes, adopting low-cost and flexible dielectric materials, via the versatile one-pass FDM procedure, with the possibility of varying the infill percentage, in order to tune both the dielectric constant and the loss tangent, for the implementation of a novel class of performing microwave devices and systems.

Chapter 2

Substrate Integrated Waveguide (SIW) Transitions

The recent widespread implementation of different microwave components and systems has been possible thanks to an intense, remarkable and ever-growing interest on the substrate integrated waveguide (SIW) technology [1], [3], and [84]. In fact, as mentioned in Section I.1, the SIW technology combines the positive aspects of both classical planar technologies and standard metallic waveguides, providing moderately low losses in combination with a shielded structure. In addition, it is possible to manufacture SIW components via easy, cost-effective and flexible manufacturing procedures. Those features guarantee a complete integration of entire wireless systems, in compliance with the fresh evolution of the wireless market, with a specific attention on Internet of Things (IoT) and fifth mobile generation (5G) applications.

Following those market requests, a huge variety of diverse SIW devices dedicated to different applications, like couplers, mixers, filters, power dividers, antennas, etc. has been proposed in the scientific literature [43], and [93]-[96]. In all those examples, especially for components integration requirements and measurement purposes, it is needed to implement a performant transition between the SIW structure and other typologies of transmission lines. In particular, exploiting the planarity of the SIW structure, direct transitions with other planar transmission lines have been widely adopted. A brief historic overview on SIW transitions (particularly microstrip-lines and coplanar waveguide to SIW) has already been presented in Section I.8. However, a more broad selection consists of tapered microstrip-lines to SIW [97]-[100], coplanar and grounded coplanar waveguide (CPW) to SIW [101]-[103], coplanar stripline (CPS) to SIW [104], slot line to SIW [105], suspended line to SIW [106], and including also different waveguide topologies to SIW [107]-[110]. The majority of those structures have

been designed to operate with the fundamental TE_{10} SIW mode, thus working in a reasonably low frequency band. Conversely, the recent attracting need of 5G applications is demanding to exploit high frequency bands, while maintaining a simple geometry and low fabrication costs. Those requirements suggest to investigate SIW components operating with high order modes. In addition, those devices should provide low transmission losses, avoiding any radiation leakage, possible when shielded solutions are adopted. For those reasons, an investigation on novel transitions is required and a good candidate seems to be the coaxial cable, structure able both of preventing radiation leakage and supporting the propagation of higher order modes. A deep investigation on SIW coaxial launchers is presented in the next paragraphs, leading to the proposal of an innovative combined launcher for two SIW modes.

This Chapter is organized as follows. First, an historical overview on different SIW coaxial launchers is presented. Subsequently, an investigation on single SIW modes launchers is discussed. Specifically, two prototypes have been examined: the former implements a fundamental quasi-TE_{10} SIW mode launcher, while the latter represents a second quasi-TE_{20} SIW mode launcher. In particular, parametric analyses on substrate parameters, feeding displacements and capacitive effects have been considered for both structures. Furthermore, in both cases, back-to-back prototypes have been realized and tested, proving the simulated outcomes. Afterwards, the idea of a combined launcher for two SIW modes, coming from the integration of the two previous structures, is highlighted in detail. Then, a slightly modified launcher for the fundamental quasi-TE_{10} SIW mode is presented and experimentally validated through a back-to-back prototype. Eventually, the novel combined two SIW modes structure is analysed, constructed and measured. Finally, the retrieved performances are compared to the state of the art technologies, paving the road to the implementation of a low-loss, simple, repeatable, and robust to fabrication inaccuracies transition, that supports the propagation of two SIW modes within the same physical structure.

The achieved results have been collected and published in [111].

2.1 The Substrate Integrated Waveguide Coaxial Launchers

Among all the various transitions between the SIW structure and other types of transmission lines, the SIW coaxial launcher represents an excellent candidate in terms of low transmission losses and possibility to support high order modes, as highlighted in the previous Section.

For those reasons, several transitions between coaxial cable and planar waveguides have been proposed [22]-[29]. In particular, in [22] the authors theoretically investigate the design of low-cost non-radiative SMA-to-SIW launchers, where the connector is directly inserted in the SIW-section, achieving a 18% fractional bandwidth, evaluated at -20 dB, at the operative frequency f=10 GHz for the fundamental quasi-TE_{10} SIW mode. Similarly, in [23] R-type and G-type connectors are implemented to feed substrate integrated radiating waveguides, obtaining fractional bandwidth in the order of the 30%. Instead, a more sophisticated solution is presented in [24] with a tapered termination of the SIW-line, and a particular geometry etched on the top metal plane. In this case, measurement results of a back-to-back prototype provide a 23 % fractional bandwidth, evaluated at -15 dB, around the operative frequency f=10 GHz, with 1.2 dB of insertion losses. Later, in [25] and [26] the authors proposed a novel configuration for a compact and direct coaxial line to SIW transition, removing the conductor from the top metal plane, thus creating an artificial magnetic wall, achieving the wider performance in [26] of a 48.5% fractional bandwidth, evaluated at -15 dB, around the operative frequency f=10 GHz, with an insertion loss of 0.75 dB. Then, in [27] the authors implement an hybrid system with microstrips and coaxial cables, with a wideband transition, for parallel multi-channel signalling systems applications. Besides, in [28] a SIW cavity-backed circularly polarized antenna is fed using two different transitions, the tapered microstrip and the direct coaxial cable. Rather, in [29] a systematic analysis of a via-to-SIW transition is presented. This briefly summarize an attention grabbing research topic for microwave engineers, with the possibility to implement more and more efficient transitions between coaxial cables and the SIW structure.

Nevertheless, in most of those cases, the attention has been focused only on the transmission of a single quasi-TE_{n0} SIW mode, thus not exploiting the capability of exciting different SIW modes by using the coaxial cable. For this reason, as previously noted, to fully exploit the potentialities of the coaxial cable, it is convenient to investigate the possibilities to excite in the same structure both the fundamental quasi-TE_{10} and the second quasi-TE_{20} SIW modes.

Finally, properly from this consideration originates the idea of implementing a two SIW modes combined launcher, that will be presented in the following Sections.

2.2 The Single SIW Mode Launchers

This Section is dedicated to the analysis, design, and experimental verification of single SIW mode launchers. In particular, the fundamental quasi-TE_{10} SIW mode and the second quasi-TE_{20} SIW mode launchers will be considered.

As for theoretical investigations, parametric analyses on substrate thickness, coaxial cable displacement and capacitive effects of a circle etched on the SIW top metal plane, in the proximity of the feeding, will be performed in detail. Specifically, all the simulations have been carried out through the commercial full-wave electromagnetic software Ansys HFSS.

In addition, as for substrate choice, the commercial laminate Taconic TLY-5, with dielectric permittivity $\varepsilon_r = 2.2$, dielectric loss tangent $\tan\delta = 0.0009$, thickness $h = 1.53$ mm, and metal conductivity $\sigma = 5.8 \cdot 10^7$ S/m, has been adopted for the design and the practical implementation of all the transitions presented in this work.

Subsequently, regarding the manufacturing procedure, a LPKF E33 milling machine has been utilized to pattern the metal layers and to drill the via through the substrate itself. Later, a silver-based conductive paste has been employed to metalize the via holes, implementing the side walls of the SIW. Moreover, the adopted connectors are the SMA-coaxial-cable with square flange extended dielectric female receptacles, namely the R125-414-000 provided by Radiall. Those connectors are directly inserted through the substrate and soldered at both top and bottom metal planes, thus ensuring a straightforward, simple, repeatable and robust to fabrication inaccuracies transition.

Eventually, back-to-back prototypes have been manufactured and tested through the Anritsu 37347C vector network analyser, thus proving the simulated outcomes.

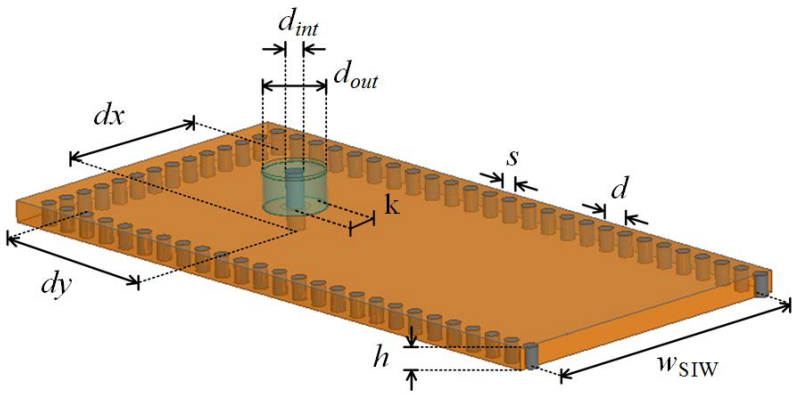

Fig. 1 - 3D model of the launcher of the fundamental quasi-TE_{10} SIW mode,
along with its geometric dimension in mm [111]:
d_{int} = 1.27, d_{out} = 4.4, d_x = 10.5, d_y = 12.5, w_{SIW} = 21, h = 1.53, k = 1.25, d = 1, and s = 2.

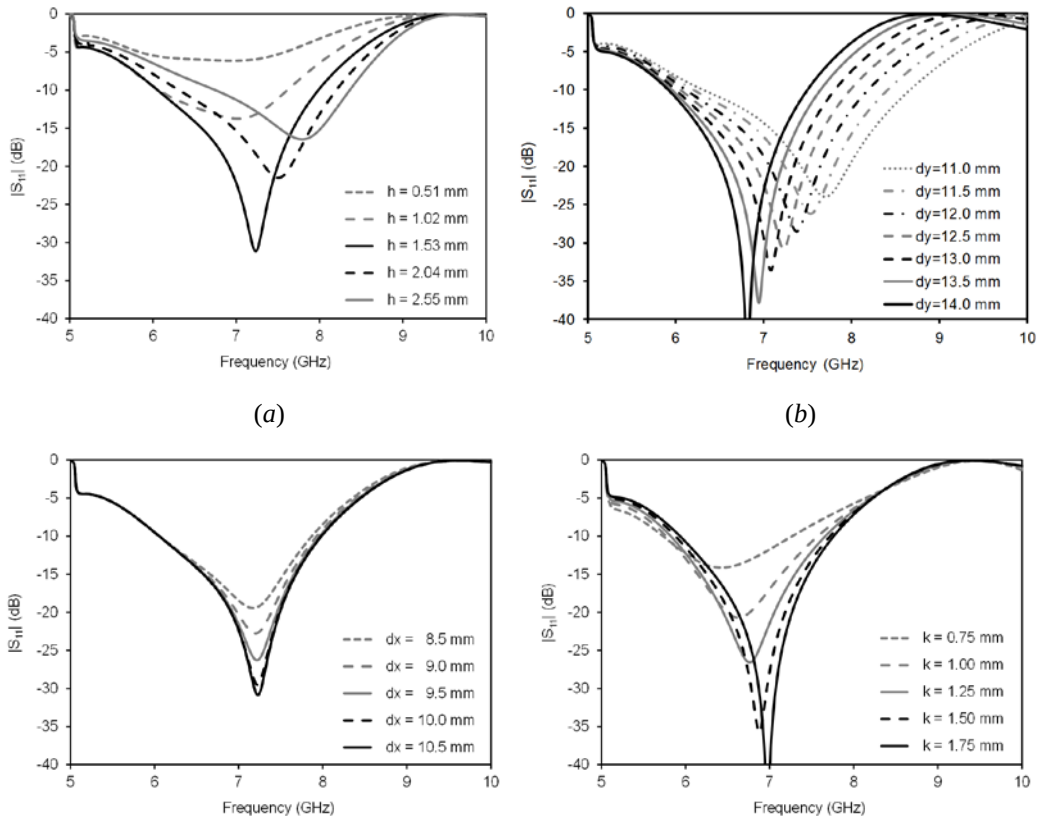

(*a*) (*b*)

(*c*) (*d*)

Fig. 2 - Parametric analyses of the scattering parameter $|S_{11}|$ versus frequency
for the launcher of the fundamental quasi-TE_{10} SIW mode [111]:
(*a*) Effect of the substrate thickness h;
(*b*) Effect of the displacement d_y;
(*c*) Effect of the displacement d_x;
(*d*) Effect of the radius k of the circular shape etched from the top SIW metal plane.

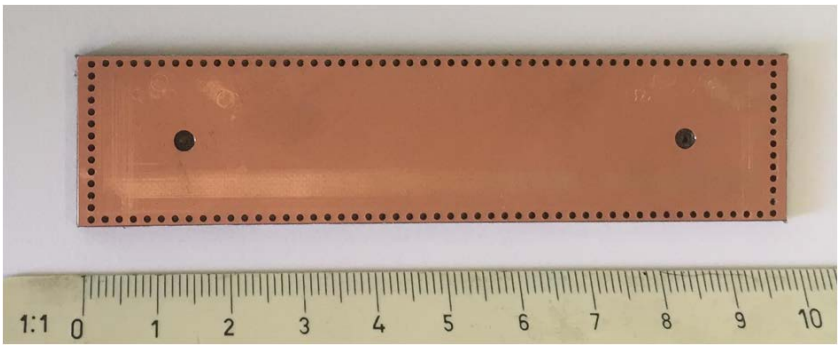

(*a*)

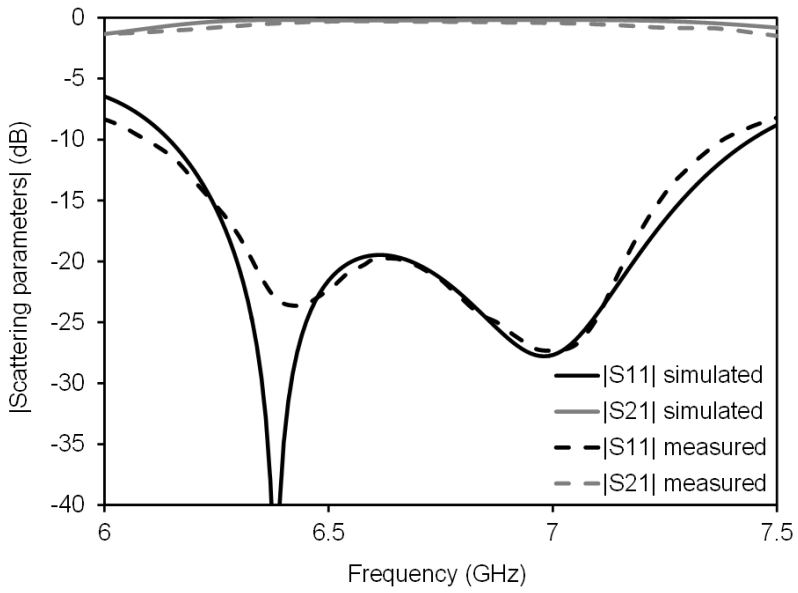

(*b*)

Fig. 3 - Back-to-back prototype of the fundamental quasi-TE_{10} SIW mode launcher [111]:
(*a*) Photograph of the manufactured prototype, prior to the metallization of the posts and prior to the soldering of the connectors;
(b) Simulated (continuous lines) and measured (dotted lines) scattering parameters.

2.2.1 The Launcher of the Fundamental Quasi-TE_{10} SIW Mode

A launcher of the fundamental quasi-TE_{10} SIW mode is presented in this paragraph. A detailed view of the three-dimensional prototype is shown in Fig. 1. In particular, the structure consists of a direct connection between the coaxial cable and a terminated SIW-line. Moreover, the inner conductor of the coaxial cable is passing through the substrate and it is soldered at both top and bottom metal planes of the SIW structure. In addition, a concentric circle, with respect to the inner and outer conductors of the coaxial cable, is etched on the top metal plane of the SIW. Furthermore, the radius k of this circle assumes values between the dimensions of the two coaxial cable conductors radii.

Besides, as a project choice, the SIW-line has been designed to operate in a mono-modal bandwidth spanning from 5 GHz to 10 GHz. For this reason, the cut-off frequency of the fundamental quasi-TE_{10} SIW mode has been fixed at $f_c = 5$ GHz, thus providing a SIW width $w_{SIW} = 21$ mm. Eventually, a light optimization has been performed through HFSS and the retrieved values are reported in the caption of Fig. 1.

Consequently, in order to fully understand the electromagnetic response of the transition, several parametric analyses have been performed, by changing (one at a time) each single parameter. In particular, substrate thickness h, coaxial cable displacement d_x and d_y and the radius k, that regulates the capacitive effect in the proximity of the feeding, have been considered. Eventually, all the results obtained from this investigation are reported and summarized in Fig. 2.

At first, the effect of the substrate thickness h on the electromagnetic performances of the transition has been analysed. In particular, considering the commercially available thicknesses, the parameter h has been varied in the range from 0.51 mm to 2.55 mm, with a fixed linear incremental step of 0.51 mm. Results are shown in Fig. 2 (*a*). Specifically, for this study, the goal is being able to achieve the wider bandwidth with a reasonable good input matching (-15 dB for most applications, or at least -10 dB). For this reason, the preferable result is obtained when $h = 1.53$ mm, that provides the best input matching and the broadest bandwidth within the considered values.

Afterwards, the location of the coaxial cable insertion through the SIW has been considered. This location is univocally determined by two parameters: d_y, that indicates the distance between the coaxial cable and the terminating short circuit SIW wall, and d_x, that represents the displacement of the connector with respect to the exact centre of the SIW-line, equidistant from the lateral side-walls, as depicted

in Fig. 1. In all cases, the dimensions are evaluated from the centre of the inner conductor of the coaxial cable to the centre of the closer post of the corresponding via row, terminating or lateral. In particular, the former, d_y, has been varied from 11 mm to 14 mm, with a fixed linear step increment of 0.5 mm. In this case, increasing the distance d_y means lowering the working frequency and changing the input matching value. In fact, d_y denotes the distance between the feed and the terminating electric wall of the waveguide, thus creating the resonance at quarter the guided wavelength. Eventually, the value $d_y = 12.5$ mm provides the best performances inside the single-mode frequency band. Simulated results are depicted in Fig. 2 (*b*). Similarly, the effect of the latter parameter, d_x, has been considered. Specifically, d_x has been varied in the interval from 8.5 mm to 10.5 mm, with a fixed linear step increment of 0.5 mm, providing the best performances, in terms of input matching, inside the single-mode frequency band for $d_x = 10.5$ mm. Precisely, this value indicates the exact middle of the SIW: $d_x = 10.5\ \text{mm} = w_{SIW}/2$. Moreover, in this exact point, the electric field assumes maximum strength, while considering the fundamental quasi-TE_{10} SIW mode, and, for symmetry reasons, it represents the best choice, as expected from theoretical considerations. Finally, simulated results are depicted in Fig. 2 (*c*).

Subsequently, the capacitive effect, generated by the circle of radius *k* etched on the top SIW metal plane, has been investigated. In particular, *k* assumes values in the range between 0.75 mm and 1.75 mm, with a fixed linear incremental step of 0.25 mm. In this way, the minimum radius is greater than the radius of the inner conductor ($r_{int} = 0.635$ mm) and the maximum radius is lower than the outer conductor ($r_{out} = 2.2$ mm) of the coaxial cable. Simulated outcomes are reported in Fig. 2 (*d*). Observing those data, it is possible to appreciate as the variation of *k* provides a change in the series capacitance next to the feeding point, thus leading to a significant variation on the input matching of the transition. In particular, as a compromise between large input matching and wide operational bandwidth, the value $k = 1.25$ mm has been adopted, providing a $|S_{11}|$ well below -20 dB in the desired frequency band.

Successively, once parametric analyses have provided the optimum design parameters, and for measurement purposes, a back-to-back prototype of the fundamental quasi-TE_{10} SIW mode launcher has been designed, manufactured and experimentally validated. In particular, this device is formed just by simply symmetrically doubling the launcher investigated in the previous paragraphs. A detailed view of the manufactured prototype, prior to the metallization of the posts and prior to the soldering of the connectors, is shown in Fig. 3 (*a*). For sake of completeness, it is worth noting that the minimal optimized distance between the

two coaxial cables is 69.5 mm, while the other dimensions are equal to the ones reported in the caption of Fig. 1.

Subsequently, the device has been tested through the Anritsu 37347C vector network analyzer. The retrieved scattering parameters versus frequency have been compared to the simulated ones in Fig. 3 (*b*). In particular, the performed measurements are reported in dashed lines, and are in good agreement with the simulations, reported in continuous lines. The input matching, the $|S_{11}|$ curve, is well maintained under -20 dB in a band of 874 MHz, corresponding to a fractional bandwidth of 17.48% (from 6.292 GHz to 7.166 GHz) in simulation, and confirmed in measurement by 830 MHz, corresponding to a fractional bandwidth of 16.60% (from 6.325 GHz to 7.155 GHz). Moreover, similar results have been retrieved also at -15 dB, providing bandwidth of 1044 MHz, corresponding to a fractional bandwidth of 20.88 % (from 6.228 GHz to 7.272 GHz) in simulation, confirmed by the 999 MHz, corresponding to a fractional bandwidth of 19.98 % (from 6.228 GHz to 7.227 GHz) in the measured outcomes. In addition, the insertion loss, the $|S_{21}|$ curve, in the bandwidth is always greater than -0.38 dB (simulated) and -0.70 dB (measured). Finally, at $f = 10.5$ GHz (center of the band) the insertion loss is -0.18 dB (simulated) and -0.28 dB (measured).

This completes the investigation about the fundamental quasi-TE_{10} SIW mode launcher.

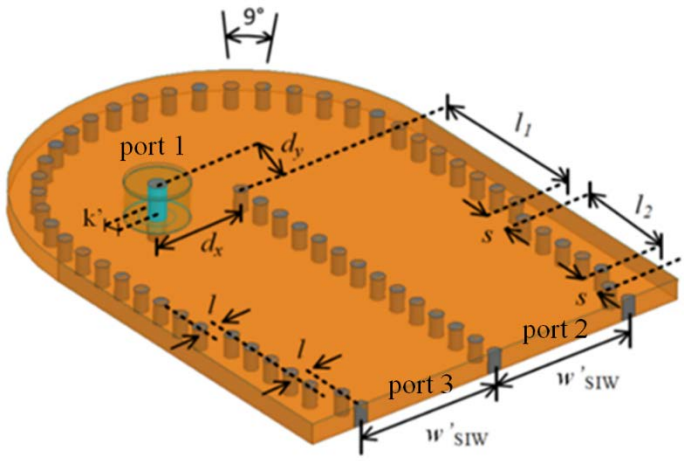

Fig. 4 - 3D model of the launcher of the second quasi-TE_{20} SIW mode [111].
Coaxial cable displacement parameters (from center to center between inner conductor and the nearest metal via of the central row): $d_x = 6.25$ mm and $d_y = -1.5$ mm.
Semi-circular region with 20 posts separated by an angle of 9° and originated with the center coincident to the center of the first post of the central row and radius of 12.5 mm ($w'_{SIW} + l + l$).
Two main waveguide sections of width $w'_{SIW} = 10.5$ mm. Lateral displacement $l = 1$ mm, spacing $s = 2$ mm, and lengths $l_1 = 12$ mm and $l_2 = 8$ mm. Radius of the etched disk $k' = 1.25$ mm.

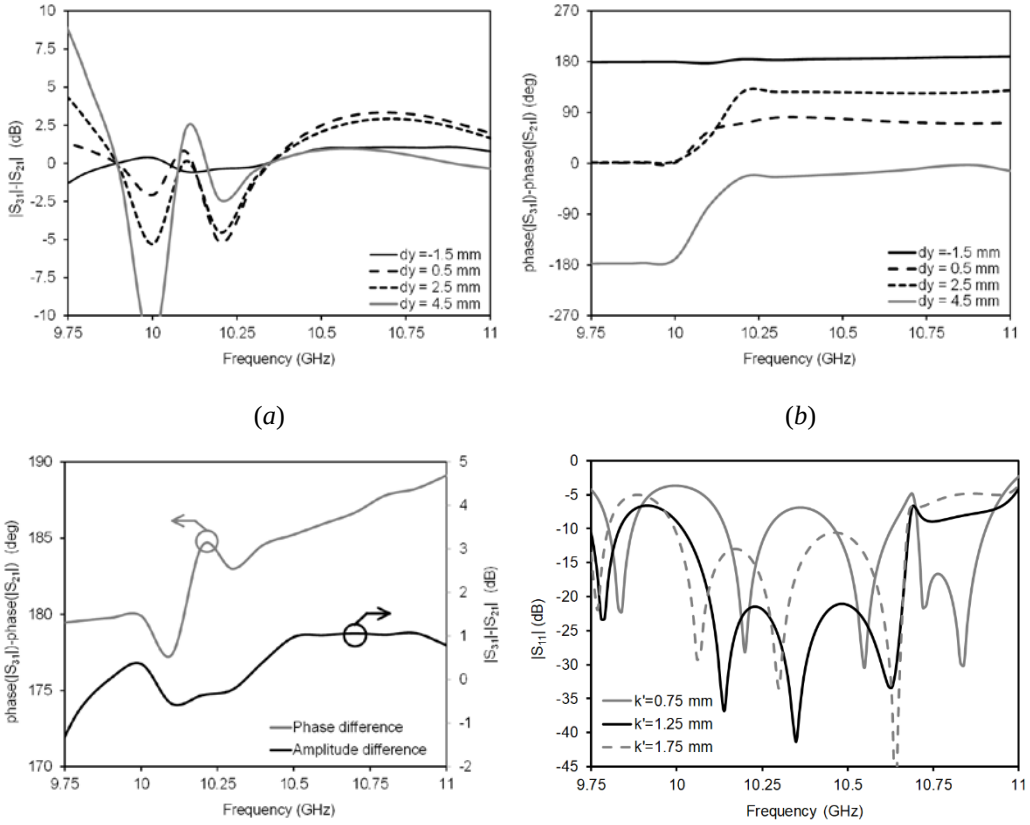

Fig. 5 - Parametric analyses on the launcher of the second quasi-TE_{20} SIW mode [111]:
(*a*) Difference of the modules of the scattering parameters ($|S_{31}|$-$|S_{21}|$ curves) versus frequency, while changing the displacement d_y of the inner conductor along the *y*-axis;
(*b*) Difference of the phases of the scattering parameters (phase($|S_{31}|$)-phase($|S_{21}|$) curves) versus frequency, while changing the displacement d_y of the inner conductor along the *y*-axis;
(*c*) Best case extrapolated and highlighted from (a) and (*b*);
(*d*) Scattering parameter ($|S_{11}|$ curves) versus frequency, while changing the radius *k'* of the circular shape etched from the top metal plane.

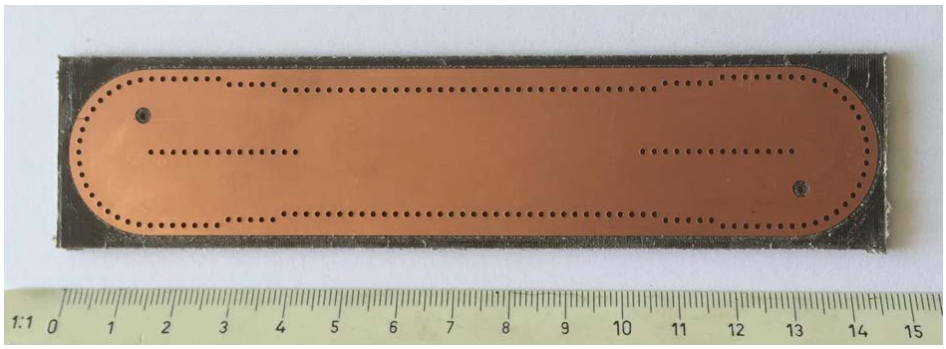

(*a*)

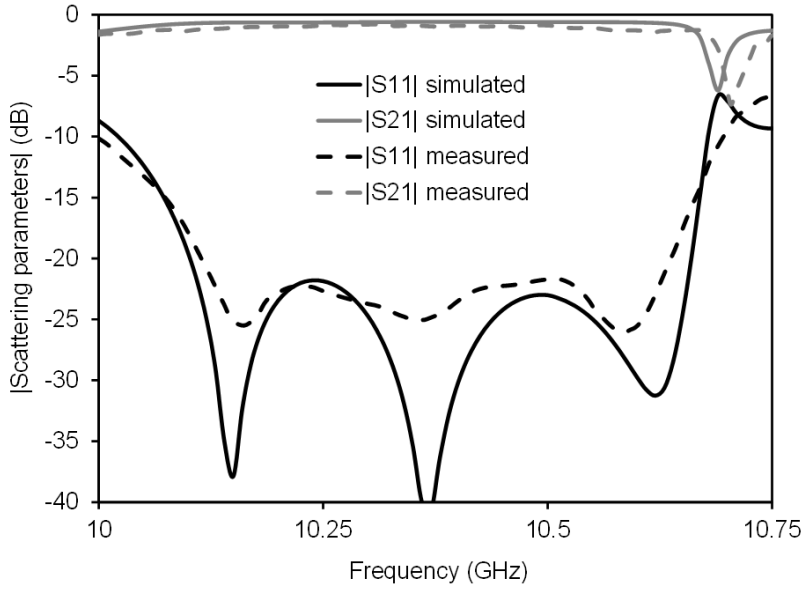

(*b*)

Fig. 6 - Back-to-back prototype of the second quasi-TE_{20} SIW mode launcher [111]:
(*a*) Photograph of the manufactured prototype, prior to the metallization of the posts and prior to the soldering of the connectors;
(b) Simulated (continuous lines) and measured (dotted lines) scattering parameters.

2.2.2 The Launcher of the Second Quasi-TE_{20} SIW Mode

A launcher of the quasi-TE_{20} SIW mode is investigated in this Section. The structure consists of a terminated circular SIW-line, equally separated by a central row of metalized posts. The purpose of this line is to create two identical waveguide sections, needed to properly excite the quasi-TE_{20} SIW mode. In addition, this field distribution requires a phase delay in order to correctly propagate, and this feature is achieved by properly locating the feeding in the circular SIW termination. A detailed view of the three-dimensional prototype is shown in Fig. 4. Moreover, simulated and optimized geometric parameters are reported in the same figure, with the values listed in the caption. In addition, similarly to the launcher of the fundamental quasi-TE_{10} SIW mode, the coaxial cable is directly inserted through the substrate and soldered at both top and bottom metal planes. Furthermore, in order to maintain the compatibility with the previous design, the waveguide sections have been kept half of the former ones, leading to $w'_{SIW}=w_{SIW}/2=10.5$ mm. In this way, the cut-off frequency of the first mode is preserved at $f_{c1}=5.00$ GHz, with the mono-modal band spanning from 5 GHz to 10 GHz, and the cut-off frequency of the second mode is fixed at $f_{c2}=10.00$ GHz.

Subsequently, in order to efficiently design the transition, similar parametric analyses, with respect to the former case, have been considered. In detail, the displacement of the coaxial cable inside the round SIW termination and the capacitive effect of the circular shape etched from the top metal plane have been investigated. Simulated outcomes are reported in Fig. 5.

At first, the position of the feeding system has been examined. In particular, this investigation is crucial to properly excite the second quasi-TE_{20} SIW mode and to optimize the bandwidth performance of the transition at the desired frequencies. The regulation mechanism is fully controlled by acting on the two parameters d_y and d_x. The former, d_y indicates the distance between the centre of the inner conductor of the coaxial cable and the centre of the nearest terminating metal post of the central via row. This parameter is of crucial importance to properly excite the second quasi-TE_{20} SIW mode. To this aim, in fact, it is important to obtain a zero moduli difference and a π phase difference between the two waves generated in the specular waveguide sections. In particular, Fig. 5 (*a*) shows the amplitude difference ($|S_{31}|-|S_{21}|$) evaluated at the two SIW sections of width w'_{SIW} (namely port 2 and port 3), with respect to the coaxial cable feeding point (namely port 1). In this case, the desired goal is being able to achieve same field amplitude at the two ports reference sections in a possible wider bandwidth, thus setting the difference $|S_{31}|-|S_{21}|$ approximatively equal to zero. Specifically, the parameters d_y

has been varied in the interval from -1.5 mm and 4.5 mm, with a fixed linear step increment of 2 mm. Simulated results have been reported in Fig. 5 (*a*). Likewise, an equivalent study has been carried out for the phase difference between the fields evaluated at the reference ports. In this situation, the main target is reaching an absolute phase difference around 180°, that means having the fields in counter-phase at those reference sections, in order to properly excite the second quasi-TE_{20} SIW mode. Simulated results have been provided in Fig. 5 (*b*). In conclusion, the optimal value that satisfies both condition is obtained for d_y=-1.5 mm. A detailed highlight of the best case is presented in Fig. 5 (*c*).

Afterwards, the capacitive effect generated by the circle of radius *k*' etched on the top metal plane of the SIW has been investigated, similarly to the analysis of the fundamental quasi-TE_{10} SIW mode launcher. In particular, *k*' assumes values in the range between 0.75 mm and 1.75 mm, with a fixed linear incremental step of 0.5 mm. In this way, the minimum radius is greater than the radius of the inner conductor and the maximum radius is lower than the outer conductor of the coaxial cable. Simulated outcomes are reported in Fig. 5 (*d*). It is clear, as this effect has a strong impact on the input matching of the transition. In particular, it has been found an optimal value for *k*' = 1.25 mm, providing a good input matching with the $|S_{11}|$ well below -20 dB in the desired frequency band.

Successively, once parametric analyses have provided the optimum design parameters, and for measurement purposes, a back-to-back prototype of the second quasi-TE_{20} SIW mode launcher has been designed, manufactured and experimentally validated. This device is formed just by simply symmetrically doubling the launcher investigated in the previous paragraphs. A detailed view of the manufactured prototype, prior to the metallization of the posts and prior to the soldering of the connectors, is shown in Fig. 6 (*a*). Subsequently, the device has been tested through the Anritsu 37347C vector network analyzer. The retrieved scattering parameters versus frequency have been compared to the simulated ones in Fig. 6 (*b*). In particular, the performed measurements are reported in dashed lines, and are in good agreement with the simulations, reported in continuous lines. The input matching, the $|S_{11}|$ curve, is well maintained under -20 dB in a band of 555 MHz, corresponding to a fractional bandwidth of 11.10% (from 10.106 GHz to 10.661 GHz) in simulation, and confirmed in measurement by 514 MHz, corresponding to a fractional bandwidth of 10.28 % (from 10.117 GHz to 10.631 GHz). Moreover, similar results have been retrieved also at -15 dB, providing bandwidth of 592 MHz, corresponding to a fractional bandwidth of 11.84 % (from 10.072 GHz to 10.664 GHz) in simulation, confirmed by the 590 MHz, corresponding to a fractional bandwidth of 11.80 % (from 10.072 GHz to 10.662 GHz) in the measured outcomes. In addition, the insertion loss, the $|S_{21}|$

curve, in the bandwidth is always greater than -0.71 dB (simulated) and -0.98 dB (measured). Finally, at $f = 10.5$ GHz (center of the band) the insertion loss is -0.52 dB (simulated) and -0.77 dB (measured).

At this stage, the second quasi-TE_{20} SIW mode launcher is ready to be integrated with the fundamental quasi-TE_{10} SIW mode launcher, thus forming the novel combined launcher for two SIW modes.

2.3 The Combined Launcher for Two SIW Modes

The fundamental quasi-TE_{10} SIW mode and the second quasi-TE_{20} SIW mode launchers presented in Section 2.2.1 and in Section 2.2.2, respectively, are now ready to be integrated and to form the innovative combined launcher for two SIW modes. In this way, the transmission of the electromagnetic field in both the mono-modal and second SIW bands is allowed within the same physical prototype. In addition, identical material, technology, fabrication procedures and testing facilities of the previous prototypes have been adopted to design, manufacture and experimentally validate the novel combined launcher for two SIW modes.

A detailed description of the project phases is presented in the following Sections.

2.3.1 Design Strategies for the Combined Launcher

A successful design to implement the combined launcher for the two SIW modes originates from the straightforward integration between the launcher of the fundamental quasi-TE_{10} SIW mode and of the second quasi-TE_{20} SIW mode. A detailed three-dimensional view of the prototype is highlighted in Fig. 7. In particular, starting from the launcher of the second quasi-TE_{20} SIW mode (with same geometric parameters as in Section 2.2.2) it is possible to insert an additional connector at the exact centre of the main SIW-line, at a distance $l_3 = 9.9$ mm from the last post of the central metalized via row, thus implementing the launcher for the fundamental quasi-TE_{10} SIW mode. In this way, in the same physical prototype, the coaxial cable inserted in the round SIW termination is used to excite the second quasi-TE_{20} SIW mode, while the coaxial cable inserted in the main SIW-line is responsible for the propagation of the fundamental quasi-TE_{10} SIW mode. Moreover, all the geometric parameters have been optimized through HFSS, and the values are reported in the caption of Fig. 4 and Fig. 7, respectively.

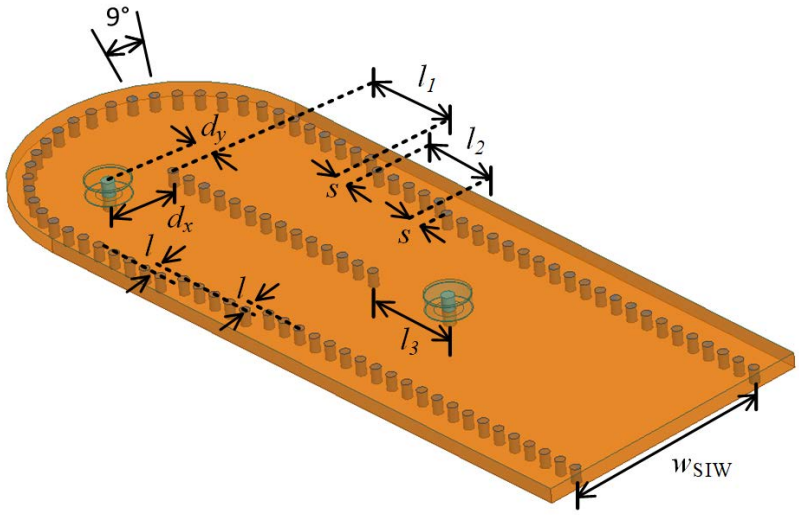

Fig. 7 - 3D model of the combined prototype, that includes the launcher of the fundamental quasi-TE_{10} SIW mode and the launcher of the second quasi-TE_{20} SIW mode. Parameters identical to the ones highlighted in Fig. 4, except for the new introduced length l_3=9.9 mm [111].

2.3.2 The Modified Launcher for the Quasi-TE_{10} SIW Mode

As mentioned in Section 2.3.1, in order to implement the combined launcher for two SIW modes, it is required to modify the geometry of the fundamental quasi-TE_{10} SIW mode launcher. In particular, it is evident from Fig. 7 as the presence of the terminating wall, typical of the previous structure, and highlighted in Fig. 1, should be avoided. In fact, this terminating barrier, that constitutes an electric wall, needs to be removed to allow the propagation of the quasi-TE_{20} SIW mode inside the structure itself. To this aim, it is sufficient to open the side-wall of the main SIW-line, maintaining only the central metal via row. Moreover, only this via row is also sufficient to prevent even the penetration of the quasi-TE_{10} SIW mode inside the two sub-sections of the SIW structure. Eventually, a parametric analysis on the necessary number of posts has been carried on through Ansys HFSS and the optimal outcome was obtained adopting three posts.

Subsequently, for measurement purposes, a back-to-back prototype of the modified launcher for the quasi-TE_{10} SIW mode has been designed, manufactured and experimentally validated. A detailed photograph, prior to the metallization of the posts and prior to the soldering of the connectors, is shown in Fig. 8 (*a*). Successively, the device has been tested through the Anritsu 37347C vector network analyser. The retrieved scattering parameters versus frequency have been compared to the simulated ones in Fig. 8 (*b*). In particular, the performed measurements are reported in dashed lines, and are in good agreement with the

simulations, reported in continuous lines. The input matching, the $|S_{11}|$ curve, is well maintained under -13.5 dB in a band of 1868 MHz, corresponding to a fractional bandwidth of 37.36 % (from 5.963 GHz to 7.831 GHz) in simulation, and confirmed in measurement by 1876 MHz, corresponding to a fractional bandwidth of 37.52 % (from 5.912 GHz to 7.788 GHz). Moreover, the insertion loss, the $|S_{21}|$ curve, in the bandwidth is always greater than -0.44 dB (simulated) and -0.96 dB (measured). Finally, at f=7 GHz (centre of the band) the insertion loss is -0.12 dB (simulated) and -0.21 dB (measured).

Eventually, the structure is now ready to be integrated in the final two SIW modes combined launcher.

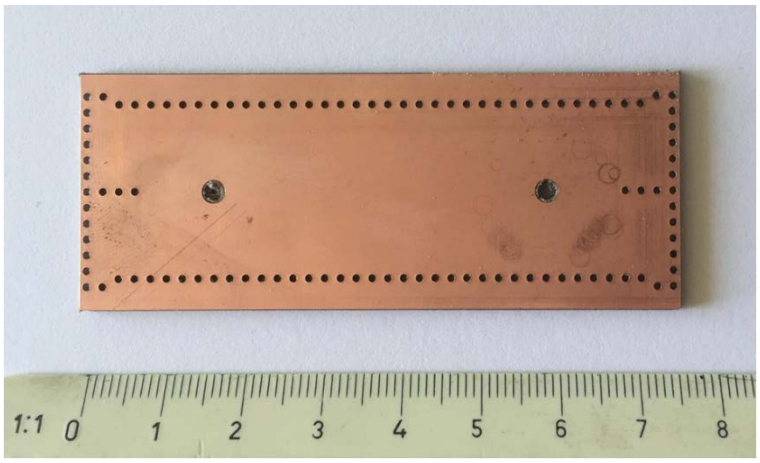

(*a*)

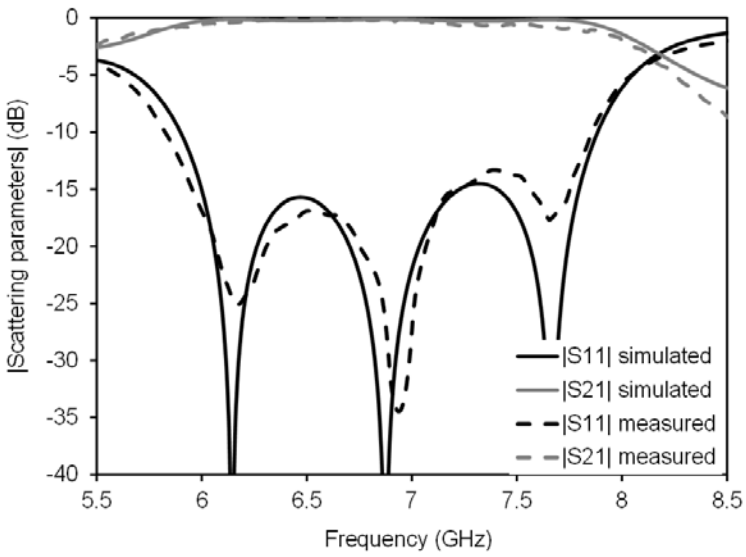

(*b*)

Fig. 8 - Modified back-to-back launcher of the fundamental quasi-TE_{10} SIW mode [111]:
(*a*) Photograph of the manufactured prototype, prior to the metallization of the posts and prior to the soldering of the connectors;
(*b*) Simulated (continuous lines) and measured (dotted lines) scattering parameters.

2.3.3 The Two SIW Modes Combined Launcher

Following the considerations proposed in the previous Sections, a combined structure, that implements both the launchers for the fundamental quasi-TE_{10} and the second quasi-TE_{20} SIW modes, has been designed, manufactured and tested. A photograph of the prototype, prior to the metallization of the posts and prior to the soldering of the connectors is shown in Fig. 9.

At first, a preliminary analysis on the number of posts constituting the central row, that separates the diverse launchers of the two SIW modes, is required. In fact, it represents the only difference compared to the previously presented prototypes. In detail, Fig. 10 highlights this effect. In particular, the number # of posts affects the length l_3 and provides the values of the coupling level between the launcher of the quasi-TE_{10} and the launcher of the quasi-TE_{20}. In addition, by regulating this value it is possible to achieve a good level of isolation between the two ports, while keeping the dimensions of the transition as compact as desired. A reasonable compromise has been found when selecting 14 posts. This choice ensures a $|S_{31}|$ well maintained under -20 dB among the desired band, where the transition of the second quasi-TE_{20} SIW mode is optimized.

Subsequently, following those considerations, the prototype has been manufactured and experimentally validated. The most significant results are highlighted in Fig. 11.

Initially, the performance of the fundamental quasi-TE_{10} SIW mode launcher integrated in the combined structure has been investigated. In particular, Fig. 11 (*a*) shows the scattering parameters curves versus frequency. Measured results (dashed lines) are in good agreement with simulated predictions (continuous lines). Specifically, the input matching, the $|S_{11}|$ curve, is well maintained under -15 dB in a band of 1753 MHz, corresponding to a fractional bandwidth of 35.06 % (from 6.008 GHz to 7.761 GHz) in simulation, and confirmed in measurement by 1706 MHz, corresponding to a fractional bandwidth of 34.12% (from 6.021 GHz to 7.727 GHz). Moreover, the insertion loss, the $|S_{21}|$ curve, in the considered bandwidth is always greater than - 0.38 dB (simulation) and - 0.88 dB (measurement). Finally, at f=7 GHz (centre of the band) insertion loss is -0.13 dB (simulation) and -0.23 dB (measurement). Furthermore, those achieved results are comparable with the state of the art technology for the single SIW mode launchers. A detailed comparison with previous works will be presented at the end of this paragraph, and summarized in Table I.

Subsequently, the performance of the second quasi-TE_{20} SIW mode launcher integrated in the combined structure has been considered. In particular, Fig. 11 (*b*) shows the scattering parameters curves versus frequency. Measured results (dashed lines) are in good agreement with simulated predictions (continuous lines). Specifically, the input matching, the $|S_{11}|$ curve is well maintained under -19 dB in a band of 569 MHz, corresponding to a fractional bandwidth of 11.38% (from 10.101 GHz to 10.670 GHz) in simulation, and confirmed in measurement by 595MHz, corresponding to a fractional bandwidth of 11.90% (from 10.108 GHz to 10.703 GHz). In addition, similar results have been retrieved also at -15 dB, providing bandwidth of 629 MHz, corresponding to a fractional bandwidth of 12.58 % (from 10.072 GHz to 10.701 GHz) in simulation, confirmed by the 663 MHz, corresponding to a fractional bandwidth of 13.26 % (from 10.072 GHz to 10.735 GHz) in the measured outcomes. Moreover, the insertion loss, the $|S_{21}|$ curve, in the bandwidth is always greater than -0.89 dB (simulation) and -1.25 dB (measurement). Finally, at $f = 10.5$ GHz (centre of the band) insertion loss is -0.59 dB (simulation) and -0.78 dB (measurement). Eventually, those achieved results are summarized in Table I and constitute the added value of this novel structure, able to cover two SIW modes bands simultaneously and within the same physical prototype.

Afterwards, even the isolation between the different coaxial cables of the two SIW modes launcher needs to be evaluated. In particular, Fig. 11 (*c*) presents the isolation between the launcher of the second quasi-TE_{20} SIW mode (namely port 1) and the nearest launcher of the fundamental quasi-TE_{10} SIW mode (namely port 3). Measured values (dashed lines) confirms simulated predictions (continuous lines), and the $|S_{31}|$ curve is well maintained under -20 dB, inside the desired frequency band of the second quasi-TE_{20} SIW mode. Additionally, Fig. 11 (*d*) highlights the isolation between the launcher of the second quasi-TE_{20} SIW mode (namely port 1) and the farthest launcher of the fundamental quasi-TE_{10} SIW mode (namely port 4). Even for this case, measured values (dashed lines) confirm simulated predictions (continuous lines), and the $|S_{41}|$ curve is well maintained under -19 dB, inside the desired frequency band of the second quasi-TE_{20} SIW mode.

Eventually, in order to summarize the achieved results, the main properties of the proposed two SIW modes combined launcher have been listed in Table I. In particular, the fractional bandwidth related to the fundamental quasi-TE_{10} SIW mode is comparable to the state of the art transitions. Conversely, the possibility to launch the second quasi-TE_{20} SIW mode is not achieved in the mentioned transitions, thus representing the beneficial novelty of the proposed structure.

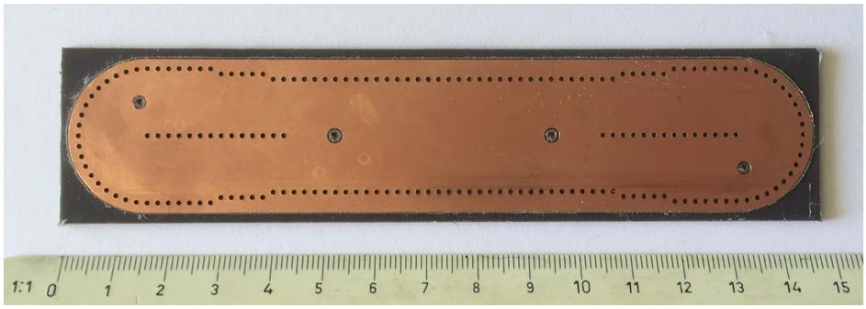

Fig. 9 - Photograph of the two SIW modes combined launcher prototype,
prior to the metallization of the posts and prior to the soldering of the connectors [111].

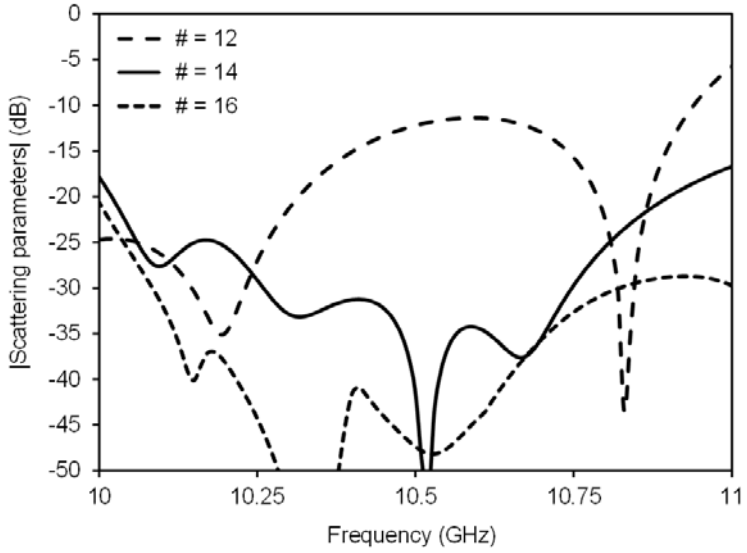

Fig. 10 - Scattering parameter curve $|S_{31}|$ for the combined launcher of two SIW modes:
parametric analysis on the number # of the central posts (that are separating the two SIW sections,
needed to launch the quasi-TE_{20} SIW mode, and that are preventing the penetration
of the fundamental quasi-TE_{10} SIW mode inside the two SIW sections) [111].

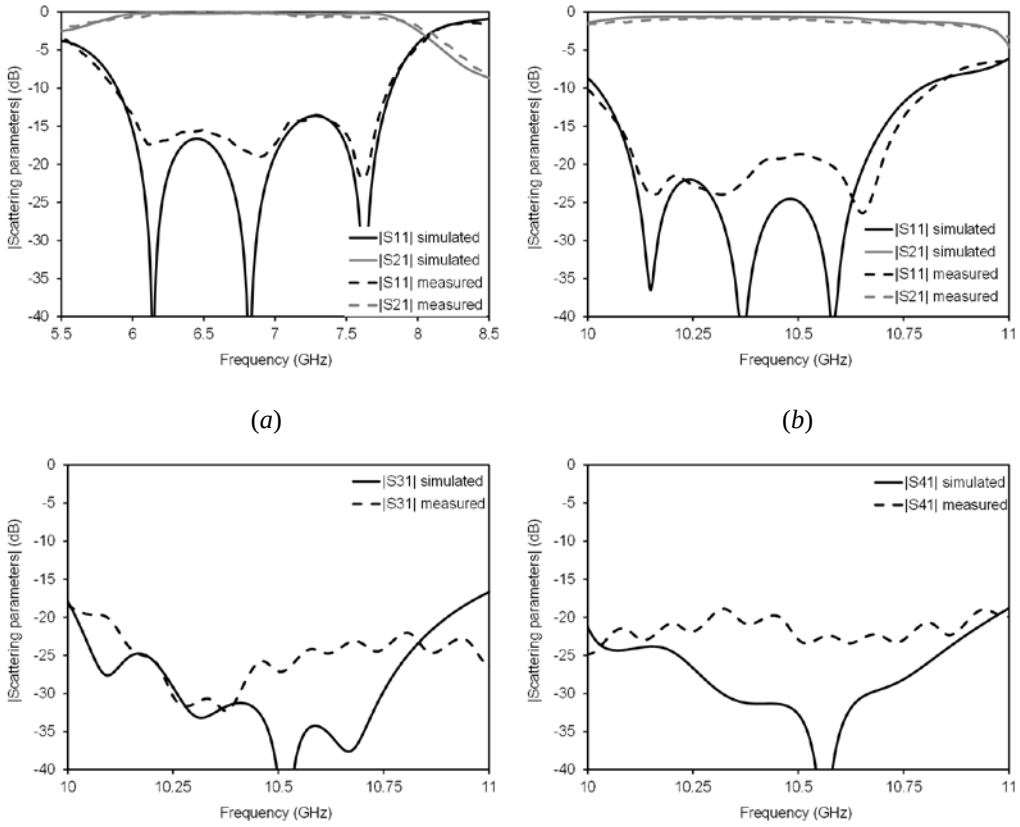

Fig. 11 - Simulated (continuous lines) and measured (dotted lines) scattering parameters curves versus frequency for the two SIW modes combined launcher [111]:
(*a*) Fundamental quasi-TE_{10} SIW mode;
(*b*) Second quasi-TE_{20} SIW mode;
(*c*) Isolation between port 1 and port 3;
(*d*) Isolation between port 1 and port 4.

TABLE I
COMPARISON TABLE WITH STATE OF THE ART TRANSITIONS

Ref.	1st mode			2nd mode	
	FBW % (-15 dB)		IL (dB)	FBW % (-15 dB)	IL (dB)
[22]	14.7		Not shown	---	---
[23]	30.0		Not shown	---	---
[24]	R-type	G-type	Not shown	---	---
	31.0	26.0			
[25]	23.0		1.2	---	---
[26]	22.0		0.82	---	---
[27]	48.5		0.75	---	---
This work	**35.1**		**0.23**	**13.2**	**0.78**

2.4 Conclusions

This Chapter presented the design strategy, the manufacturing procedure, and the experimental verification of an innovative two SIW modes combined launcher, operating in the microwave regime.

At first, a brief overview on SIW transitions has been discussed, as an extent to the classical solutions proposed in Section I.8. In particular, special attention has been dedicated to the coaxial cable to SIW transitions, due to the properties of low transmission losses and capability of supporting the propagation of higher order modes. In fact, those features suggested the possibility to create a novel transition, that implements both the launchers of the fundamental quasi-TE_{10} and the second quasi-TE_{20} SIW modes in the same physical prototype.

To this aim, at the beginning of the investigation, the transitions for the single SIW modes need to be considered separately. At first, the fundamental quasi-TE_{10} SIW mode launcher has been evaluated and optimized through several parametric analyses on substrate thickness, coaxial cable displacement, and capacitive effect next to the feeding point. Subsequently, same parametric studies have been conducted on the second quasi-TE_{20} SIW mode launcher. In both cases, back-to-back prototypes have been manufactured and tested in order to prove the simulated outcomes.

Consequently, the integration between these two transitions required a slight modification of the fundamental quasi-TE_{10} SIW mode launcher, that has been successfully achieved through the simple removal of the terminating SIW wall. Even in this case, a back-to-back prototype has been realized and experimentally validated.

Eventually, the novel two SIW modes combined launcher has been proposed, along with design strategy, manufacturing procedure and measurements, confirming the theoretical and simulated outcomes.

Finally, the retrieved results have been compared to the state of the art technology with other SIW mode launchers. The combined prototype is able to cover a 35.1% fractional bandwidth, evaluated at -15 dB, with measured insertion loss of 0.23 dB at $f = 7$ GHz, interesting data among the investigated scientific literature. Moreover, this novel combined prototype is offering also a 13.2% fractional bandwidth, evaluated at -15 dB, with measured insertion loss of 0.78 dB at $f = 10.5$ GHz, feature not present in any of the above mentioned transitions. Moreover, another relevant property consists in the direct insertion of the coaxial cable through the substrate, that implements a simple, repeatable and robust to

fabrication inaccuracies solution. Besides, the possibility to cover two different frequency bands, using only one physical transmission channel, makes the two SIW modes combined launcher an extremely interesting transition for the development of a novel class of performant SIW components and systems for the new wireless sensors network and 5G applications.

Chapter 3

Substrate Integrated Waveguide (SIW) Antennas

In the current years, the introduction of the Internet of Things (IoT) [112]-[114] and, more recently, of the fifth generation of mobile communications networks (5G) is bound to change the scenario of wireless components and systems [115], [116]. In fact, the advent of an innovative class of increasingly high performance antennas is required to meet the challenges proposed by those fresh innovative communications protocols [117]. Moreover, the rapid growth of a variety of new applications in the microwave and millimetre-wave frequency range requires the implementation of a novel class of circuits, able to integrate data transmission, wireless power transfer, and sensing capabilities in a single wireless device. The success of these new applications relies on several concurrent features: on one hand, it is fundamental to identify a technology that guarantees high performance and, at the same time, low cost for mass production. Furthermore, compact size and system miniaturization are becoming increasingly important, with the aim to develop components and systems working at higher frequencies. Finally, the constraints of a short time-to-market impose the choice of easy manufacturing processes and effective integration technologies. In parallel, also other two necessities need to be fulfilled: satisfy massive traffic volume and provide high data rate [118]. These conditions require to offer a speeder delivery with respect to the present 4G wireless networks, and the spectrum identified to provide those services is in the frequency band centred around 28 GHz, as already mentioned in [115]. These high frequency services require simple, compact in size, low-profile, low-cost, and high directivity antennas, and the natural candidate that satisfies all those features is represented by the Substrate Integrated Waveguide (SIW) technology.

Properly the SIW technology is playing a key role for the development of the future IoT and 5G systems [3], [119], for all the benefits highlighted in the previous Sections of this manuscript. In particular, simplicity in the design, easy manufacturing procedures, low transmission losses due to the complete shielded structure, facility of integration with other classical planar microwave devices (e.g. microstrip lines and coplanar waveguides), as well as active devices and integrated circuits, have fostered a rapid and variegated growth of several SIW antennas. A lot of examples could be mentioned, from classical cavity-backed SIW antennas [120], [121], till SIW active antennas [122], [123], passing through SIW leaky-wave antennas [82], and [94]. In particular, this last class of antennas caught the attention of the microwave researchers in the last years. In fact, it is possible to implement low cost, compact, high gain and high efficiency SIW leaky-wave antennas, paving the road to the development of the future 5G and WSN systems.

This Chapter is organized as follows. At first, an historical overview about SIW antennas is presented, highlighting two main classes: the slot array and the leaky-wave antennas. Among this last class, particular attention has been dedicated to the novel proposed double-sided SIW LWA. This antenna is working with its quasi-TE_{20} mode, providing an increased directivity on the *E*-plane. Subsequently, a summary of the theoretical properties has been discussed, giving the basic design rules. Afterwards, the loss mechanism in SIW and SISW-lines has been analysed, suggesting to adopt the SISW technology in combination with the quasi-TE_{20} mode to minimize transmission losses, as already observed in [43]. Later, a double-sided SIW LWA and a double-sided SISW LWA working at the centre frequency f = 28 GHz and with same radiation characteristics (radiating pointing angle θ_{RAD} = 50° and beamwidth θ = 10°) have been designed, fabricated and experimentally validated. Eventually, measured results proved the simulated outcomes: the double-sided SISW LWA presents an increased efficiency with respect to the double-sided SIW LWA, paving the road to the implementation of a novel class of extremely high efficiency antennas for the novel fifth generation (5G) of mobile communications and wireless sensors networks (WSN).

Eventually, all those results have been collected and published in [82].

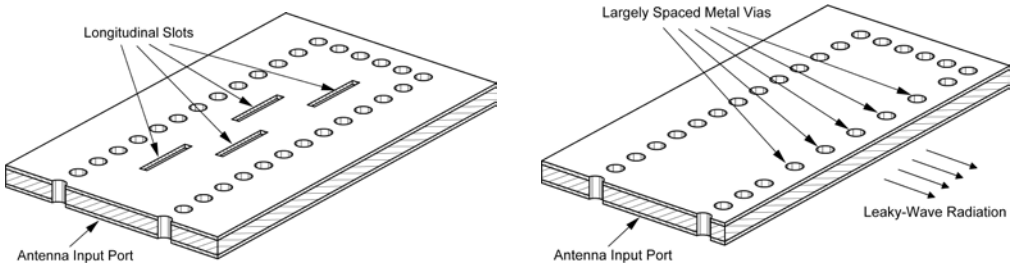

(*a*) (*b*)

Fig. 1 - 3D model of different SIW antennas [3]: (*a*) Slot array; (*b*) Leaky-wave.

3.1 An Overview on Substrate Integrated Waveguide Antennas

The substrate integrated waveguide antennas could be essentially subdivided in two main classes [3]: the SIW slot array antennas and the SIW leaky-wave antennas. In particular, the way to obtain radiation from SIW structures could be achieved by etching slots in the top metal plane, as shown in Fig. 1 (*a*), or by increasing the spacing *s* between the adjacent posts of the lateral walls, implemented by the metalized cylinders, as shown in Fig. 1 (*b*).

Considering the first class, the SIW slot array, and by adopting the same principles of classical slotted-waveguide antennas, it is possible to achieve radiation simply by etching a number of longitudinal resonant slots in the broad wall of the waveguide. A common design strategy requires the longitudinal spacing between slots to be half the guided-wavelength. Moreover, the slots are positioned in an alternate way with a slight offset with respect to the vertical symmetry plane of the SIW, thus providing broadside radiation at the desired operative frequency [124]. Furthermore, following the design strategies provided by Elliot [125], also the effect of internal high-order mode coupling is included. This phenomenon must be considered due to the geometry of the SIW structure, in fact, it arises because of the aspect ratio between substrate thickness *h* and substrate width *w* (usually *h* is way smaller than *w*). Eventually, the rotation of the slots of the amount $\pm 45°$ provides the circular polarization [126]. To summarize, the SIW slot array antennas offer reduced cost and weight when compared to the standard antennas implemented in classical waveguide technology. On the contrary, due to the dielectric losses, gain and efficiency of the SIW slot arrays are lowered with respect to the classical slotted waveguide arrays.

Considering the second class, the SIW leaky-wave antennas have been presented first in [127]. The prototype is obtained simply by increasing the longitudinal space *s* between adjacent posts in one row of side-wall metal cylinders. In fact, properly this large gap between consecutive metal posts is responsible for the radiation leakage, exploited to implement the antenna. Moreover, the larger the gap the larger the radiation leakage. This feature permits to reduce the overall length of the antenna, paying the cost of having a larger beamwidth. However, a large gap *s* could cause the band gap effect, that is accountable to the reduction of the beamwidth, due to the prevention of the propagation of the electromagnetic filed inside the SIW structure. Furthermore, it is worth noting that in leaky-wave SIW antennas, the propagation constant of the waveguide mode is the direct responsible for the direction of the maximum radiation, and the radiation pattern can be calculated by using the value of the electromagnetic field at the edge of the SIW structure. Another peculiar issue to be considered in the design of SIW leaky-wave antennas is represented by the interface between dielectric and air. In fact, an upper value for the allowed dielectric permittivity could be computed numerically, thus avoiding the total internal reflection at the dielectric/air interface [127]. Afterwards, a detailed study on a SIW leaky-wave antenna, working with the second quasi-TE_{20} mode, has been presented in [128]. This prototype provides better performances when compared to the classical SIW leaky-wave antenna, that operates with the fundamental mode, paving the road to a deep investigation about this novel structure.

Besides these two major SIW antenna categories, the slotted waveguide array and the leaky-wave antenna, other antenna configurations have been proposed and implemented in SIW technology. A complete summary could be found in [3]. Some examples include SIW cavity-backed slotted antennas [129], [130], active SIW cavity-backed slotted antennas [122], [123], *H*-plane SIW sectoral horn antennas [131], Yagi-Uda antennas [132], [133] and, finally, also frequency selective surfaces (FSS) and polarizers [134]-[136]. Those numerous examples validate the versatility of the SIW technology that could be exploited to create a large set of components operating in the microwave regime.

3.2 The Double-sided SIW Leaky-wave Antenna

As mentioned in the previous Section, the radiation properties of LWA are mainly determined by the complex propagation constant of a leaky mode. Depending on the topology adopted to implement this kind of antennas, it is possible to achieve different radiation characteristics [137], that can be modified simply by controlling

the leaky mode of the structure. Moreover, LWAs generally provide high gain and ease of integration with other structures, thus attracting the interest of researchers through the last years. A wide range of diverse implementations on different transmission lines (e.g. microstrip lines, coplanar waveguides, stripline, etc.) has been proposed, a summary could be retrieved in [137]. Among them, a special attention has been dedicated to planar LWAs, due to the appealing characteristics of low-cost, low-weight, low-profile and ease of integration with other circuitry. In addition, thanks to this versatility, the LWAs can be used in different scenarios, ranging from automotive radars [138], to indoor communications [139], passing through over conformal surfaces [140].

As for radiation properties, typically, the radiation pattern of the mono-dimensional LWAs is equivalent to that of a single line-source, providing only directivity along its longitudinal plane while showing a fan-beam at the cross-plane [137]. Array solutions have been proposed to overcome this flaw [141], [142]. Subsequently, a different approach proposed the usage of a single LWA with two radiating line-sources along the cross-plane [143], [144], thus avoiding the necessity of feeding networks. In this way, the main drawback consists of the possibility to control only the phase constant β of the leaky mode.

Instead, the simultaneous control of the leakage rate α and the phase constant β of the leaky mode $k = \beta - j\alpha$ has been achieved in a double-sided SIW LWA working with its second quasi-TE_{20} mode [94], [145], [146]. A detailed view of the prototype is highlighted in Fig. 2. In this case, the spacing *P* between adjacent posts has been increased on both sides of the SIW. Due to this symmetry, the generated equivalent magnetic currents M_1 and M_2 are added in phase at the centre of the antenna. In this way, they both contribute to the radiation, thus improving the directivity in the *E*-plane. In fact, this is possible thanks to the field configuration of the quasi-TE_{20} mode, that provides opposite polarizations at the two radiating edges, conversely to the case of the fundamental quasi-TE_{10} mode, that exhibits same polarization at both radiating edges, thus providing a null in the exact centre of the antenna. Furthermore, the spacing *P* between via mainly determines the leakage rate, while the width *w* of the SIW is responsible for the phase constant, thus demonstrating the independent control on α and β.

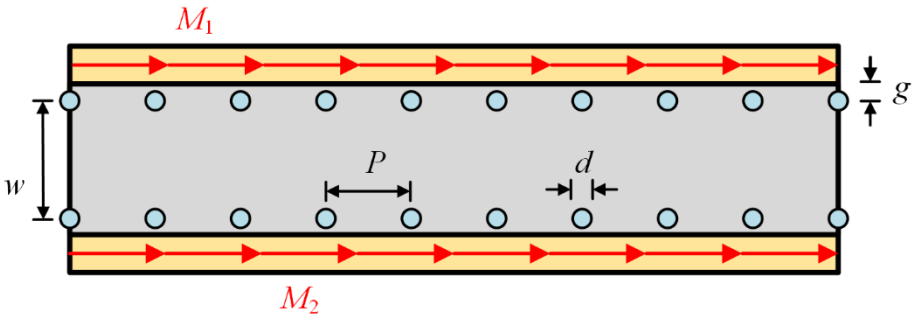

Fig. 2 - Schematic top view of the double-sided SIW LWA, along with its two equivalent magnetic currents M_1 and M_2.

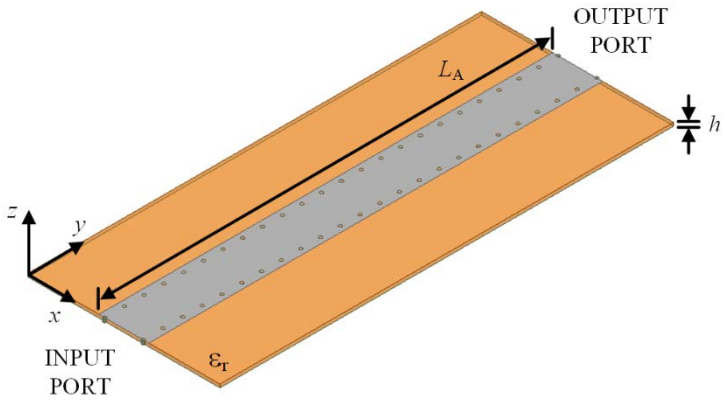

(*a*)

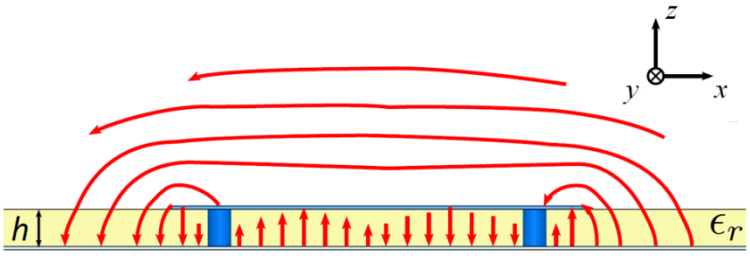

(*b*)

Fig. 3 - Double-sided SIW LWA [94]:
(*a*) 3D view of the prototype;
(*b*) Electric field distribution for the second quasi-TE_{20} SIW mode at the cross-section (*E*-plane).

3.2.1 Theoretical Analysis of Double-sided SIW LWA

A deep theoretical investigation on the double-sided SIW LWA has been presented in [94]. A summary of the crucial formula is reported in this Section, in order to understand the basic working principles of this structure.

In particular, the proposed double-sided SIW LWA is working with its second quasi-TE_{20} SIW mode and it guarantees a fully control on the complex propagation constant, as mentioned in the previous Section. In detail, the separation P between adjacent posts mainly affects the leakage rate α, while the width of the waveguide w mainly controls the phase constant β, thus ensuring a regulation mechanism on the complex propagation constant $\gamma = jk = \alpha + j\beta$. However, a simultaneous control over P and w is needed, since the values of α and β are coupled.

Subsequently, Fig. 3 (*a*) highlights the three-dimensional vision of the antenna prototype while Fig. 3 (*b*) shows the field distribution related to the quasi-TE_{20} SIW mode for the cross-section of the LWA, on the *E*-plane. Specifically, this image corroborates the phenomenon previously explained: the antenna presents two radiating sides, that can be modelled as two magnetic currents (M_1 and M_2 of Fig. 2) along the edges of the SIW LWA. Moreover, since the global width of the SIW LWA is $\approx \lambda_0$, the radiation of these magnetic currents is added in phase at the centre of the antenna. Eventually, only the second quasi-TE_{20} SIW mode is present in the structure, due to the suppression of the fundamental quasi-TE_{10} SIW mode, that allows for a simpler analysis of the structure.

Following the considerations of the previous paragraph, the complex propagation constant of the second quasi-TE_{20} SIW mode can be expressed as

$$k_z(z) = \beta_z(z) - j\alpha_z(z)$$

where β_z represents the phase constant and α_z the leakage rate along the *z*-axis. In addition, the radiating pointing angle $\theta_{\mathrm{RAD}}(z)$ can be determined by relating β_z with the free-space wavenumber $k_0 = 2\pi/\lambda_0$ as

$$\sin\theta_{RAD} = \beta_z(z)/k_0$$

Furthermore, the beamwidth $\Delta\theta$ can also be expressed as function of the total antenna length L_A and of the radiating pointing angle θ_{RAD}

$$\Delta\theta \approx \frac{1}{\frac{L_A}{\lambda_0} cos\theta_{RAD}}$$

that is providing a fast and straightforward way to identify the total antenna length L_A, once θ_{RAD} and $\Delta\theta$ are set. Eventually, the leakage rate α is determined for a desired radiation efficiency exploiting the formula $\eta_{RAD} = 1 - e^{-2\alpha L_A}$. All those formula are needed to efficiently design a double-sided SIW LWA.

3.3 Analysis of the Loss Mechanism in SIW and SISW lines

The geometric properties and the working principle of the substrate integrated slab waveguide (SISW) have been presented and discussed in Section I.9.3. This configuration represents a modified version of the conventional SIW structure and it is commonly used to increase the single-mode bandwidth. In addition, as observed in [43], it provides also a beneficial reduction in term of losses, when considering the frequency band related to the second quasi-TE_{20} mode. In fact, the attenuation constant of the second SISW mode assumes lower values with respect to the attenuation constant of the second SIW mode. This mechanism occurs due to the propagation of the second quasi-TE_{20} SISW mode in the lateral portions of the structure. In this way, the more intense electric field is travelling in the lateral air-filled parts, benefiting from the lower $\tan\delta$ offered by those air enclosures. This feature can be exploited in the design of devices and systems based on the SISW technology and operating with the second quasi-TE_{20} mode. Indeed, those properties allow the design of a simple, low-cost, low-profile, and compact in size circuitry that could operate at higher frequency, by exploiting the second mode. Moreover, all those features are compliant with the novel requirements of the fifth generation (5G) of mobile communications, the wireless sensors networks (WSN), and the Internet of Things (IoT), paving the road to a future class of SISW devices and systems operating in the microwave and mm-wave regimes.

In order to prove the concept of loss reduction, a detailed analysis on the attenuation constants of both SIW and SISW structures is required. In particular, by adopting the commercial software Ansys HFSS, it is possible to retrieve the attenuation constants via full-wave electromagnetic simulations. In this case, both structures, the SIW and the SISW, have been designed to operate with the second band centred at the operative frequency f=28 GHz, in compliance with the 5G requirements. For this reason, the width of the SIW-line assumes a different value with respect to the width of the SISW-line. Furthermore, as substrate choice, it has been adopted the RT/duroid® 6002 laminate (ε_r=2.94, tgδ=0.0012, and thickness h=0.508 mm). Besides, also the finite conductivity of both metal planes and lateral via has been considered, assuming the value reported in the data sheet for the finite conductivity of $\sigma=5.8\cdot10^7$ S/m. Finally, results are displayed in Fig. 4.

Subsequently, by observing Fig. 4, it is possible to appreciate that in the first mode the difference between the α of the SIW and the α of the SISW it is not as remarkable as in the second mode. In particular, losses are significantly decreased in the band related to the second mode. Specifically, considering the operative frequency f=28 GHz, explicitly dedicated to 5G applications, it is evident as the value of the attenuation constant has been halved. In fact, precisely for the second mode, it has been observed an α_{SIW}=1.8 (1/m), while the α_{SISW}=0.91 (1/m). This feature leads inherently to the significant reduction in term of losses, and pave the road to the implementation of SISW components, working with the second quasi-TE_{20} mode, dedicated to high frequency microwave and mm-wave applications.

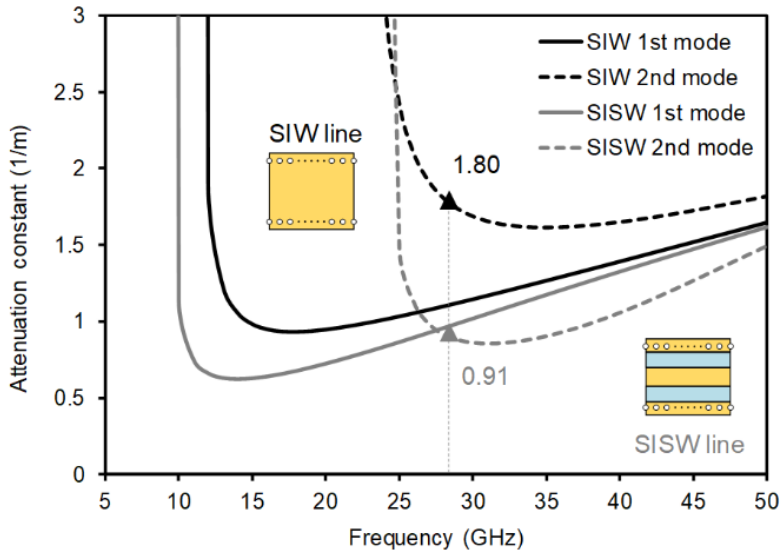

Fig. 4 - Comparison between the attenuation constants
for the SIW-line and the SISW-line (first and second modes) [82].

TABLE I
COMPARISON OF THE ATTENUATION CONSTANTS
EVALUATED AT 28 GHZ FOR DIFFERENT SUBSTRATES CHOICE

Material	ε_r	tan δ	Technology	Attenuation (α) [1/m]
FR-4	4.4	0.02	SIW	24.40
			SISW	13.47
RT/duroid® 6002	2.94	0.0012	SIW	1.80
			SISW	0.91

Eventually, Table I presents a direct comparison between the attenuation constants for two different substrates and technologies choice. In particular, the high performance RT/duroid® 6002 laminate is directly compared to the commercial low-cost laminate, the FR-4. The responsible of the large gap between the attenuation constants for these two diverse materials is represented by the loss tangent ($\tan\delta_{FR\text{-}4} = 0.02$ that is significantly larger than $\tan\delta_{RT/duroid6002} = 0.0012$). Still, the reduction of the attenuation constant for the SISW is remarkable when compared to the SIW, also in the case of the FR-4. For this reason, the SISW solution, combined with the second quasi-TE_{20} mode, allows to create microwave components, with acceptable performances, even when adopting extremely low-cost substrates, with high $\tan\delta$, like the FR-4.

3.4 Design and Testing of a Double-sided SIW LWA

Following the criteria highlighted in Section 3.2.1, a double sided SIW LWA has been designed adopting the specifications of $f = 28$ GHz, as centre operative frequency, $\theta_{RAD} = 50°$, as radiating pointing angle, and $\theta = 10°$, as beamwidth. A detailed view of the three-dimensional prototype is shown in Fig. 5, along with its main geometric parameters and optimized values, using the full-wave software Ansys HFSS.

First, the SIW LWA, as shown in the lower part of Fig. 5, has been considered. During this project phase, it is useful to recall that the antenna is working with the second quasi-TE_{20} SIW mode, and due to the asymmetry generated by this field distribution presents an increased directivity in the *E*-plane. Moreover, it is also worth remembering that it is possible to fully control the complex propagation constant by modifying the separation between posts *P*, responsible for the leakage rate, and the width of the SIW-line *w*, mainly responsible for the determination of the radiating pointing angle. Those values are used to achieve the desired α and β, as already described in Section 3.2.1. Subsequently, using the formula presented in Section 3.2.1, the total length *L* of the antenna can be obtained from the fixed radiation properties. Eventually, the extra metal gap *g* is tuned to complete the design procedure.

Afterwards, for measurement purposes, a direct, low-loss, compact coaxial cable to SIW transition has been implemented, as shown in the upper part of Fig. 5. The feeding consists of a coaxial launcher directly passing through the SIW structure, and soldered on both metal planes, to ensure electrical contacts. Simplicity, total shielding and ease of repeatability are the main feature of this

transition. In this way, it is possible to properly excite the quasi-TE_{20} SIW mode inside the structure, and, at the same time, to suppress the propagation of the quasi-TE_{10} SIW mode. This solution is totally similar to the one presented and widely discussed in Chapter 2, with the simple addition of eight matching posts. A detailed view along main geometric parameters is provided in the upper part of Fig. 5.

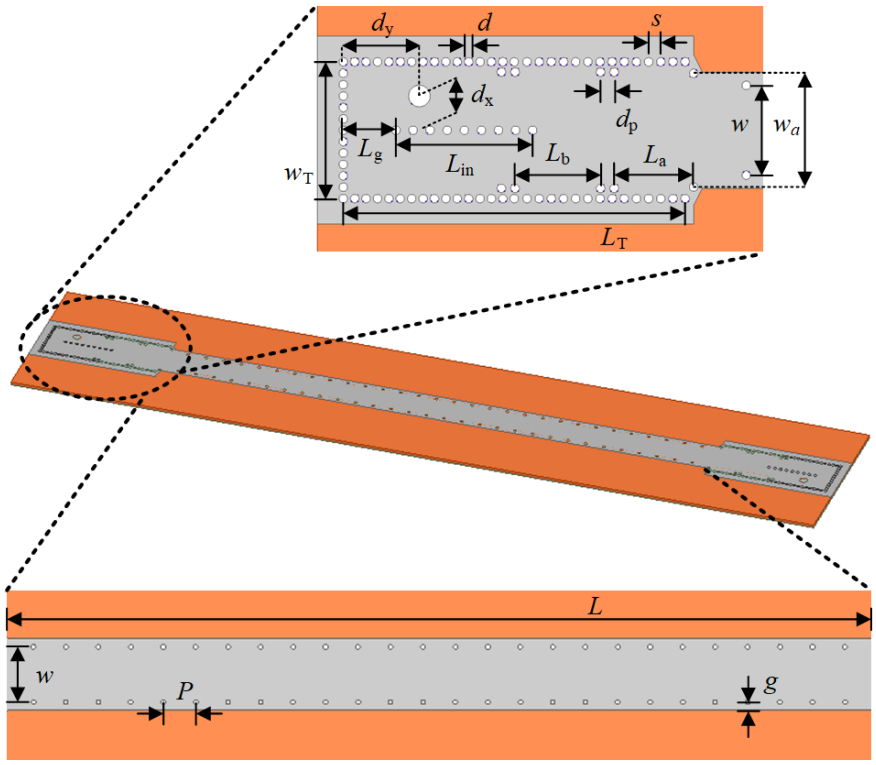

Fig. 5 - 3D model of the SIW LWA [82].
Upper part: detailed highlight of the feeding and transition used to excite the quasi-TE_{20} mode (values of the parameters in mm: w_T = 8, d_y = 4.45, d_x = w/4= 2, L_g = 3.08, L_{in} = 8, L_a= 4.65, L_b= 5, L_T = 20, w = 5.25, w_a = 6.65, d_p = 1, s = 1, and d = 0.5).
Lower part: detailed highlight of the main SIW-line
(values of the parameters in mm: w = 5.25, P = 3.08, g = 0.78, L = 95.5).

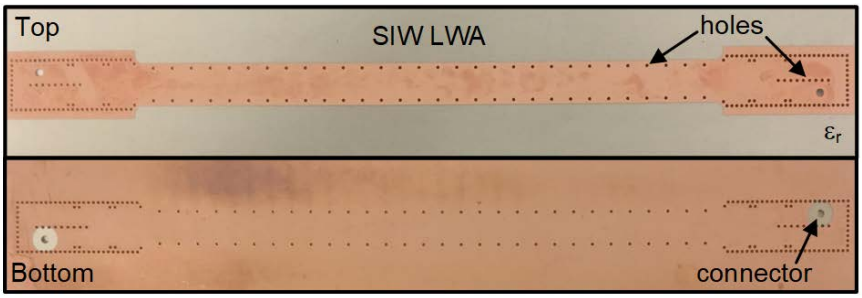

Fig. 6 - Photograph of the manufactured SIW LWA prototype [82].

Subsequently, in order to validate the simulated results, a prototype has been manufactured. A detailed view of top and bottom faces, prior to the soldering of the connectors, and prior to the metallization of the posts, is highlighted in Fig. 6. The substrate adopted is the RT/duroid® 6002 laminate, with the following characteristics: $\varepsilon_r = 2.94$, $\tan\delta = 0.0012$, thickness $h = 0.508$ mm, and metal conductivity $\sigma = 5.8 \cdot 10^7$ S/m. Furthermore, as for technology process, a laser drilling numerically controlled milling machine has been adopted to shape the metal layers and to drill the holes through the substrate. Then, the holes have been metallized by electroplating, and, finally, the connectors have been inserted through the substrate and soldered to both metal planes, thus completing the prototype manufacturing.

Afterwards, the same prototype has been experimentally validated. First, in Fig. 7 are depicted the simulated (solid line) and measured (dashed line) normalized radiation pattern of the SIW LWA in the *H*-plane (yz-plane, i.e. $\phi = 90°$), at the operative frequency of $f = 28$ GHz. In this case, measurements validate both the pointing angle of 50° and the beamwidth of 10°, thus demonstrating a good control of the complex propagation constant, as foreseen in simulations. Following, the normalized radiation patterns for the *E*-plane are highlighted in Fig. 8. In this case, the *E*-plane is defined along the angle of maximum radiation ($\theta_{RAD} = 50°$) and the angle ϕ assumes values in the range from 0° to 180°. In both cases, measured results are in good agreement with the simulated outcomes. Moreover, the cross-pol is well maintained, both in simulation and measurement, under -20 dB with respect to the normalized maximum value of the co-pol for the whole range of ϕ. Furthermore, it has been noted that the co-pol component has a -3 dB beamwidth of $\Delta\theta = 34°$ in simulation and $\Delta\theta = 30°$ in measurement, and a maximum gain of 14.36 dB in simulation and 14.21 dB in measurement. This measured gain leads to an overall efficiency of 88.15% for the SIW LWA prototype. Eventually, the scattering parameters versus frequency are reported in Fig. 9. Measured results are in dashed lines, while simulated results are in solid lines. In particular, at the working frequency of $f = 28$ GHz, the measured $|S_{11}| = -26.95$ dB confirms by the simulated $|S_{11}| = -28.77$ dB, and also the measured $|S_{21}| = -17.02$ dB proves the simulated $|S_{21}| = -16.30$ dB. Moreover, the observed narrow band is due to the compact feeding used to excite the second quasi-TE_{20} SIW mode. Other configurations [78], based on branch lines could provide wider bandwidths at the expense of increasing the overall size of the system.

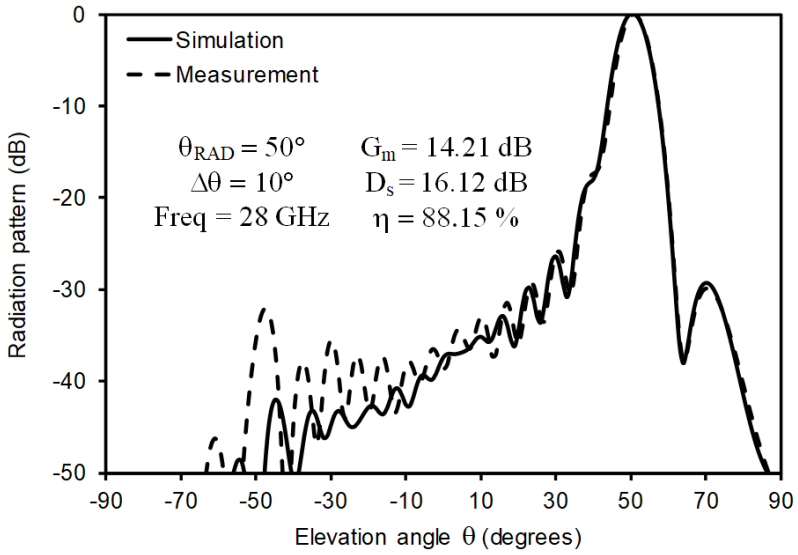

Fig. 7 - Measured and simulated normalized *H*-plane ($\phi = 90°$) radiation pattern of the SIW LWA, evaluated at the frequency $f = 28$ GHz [82].

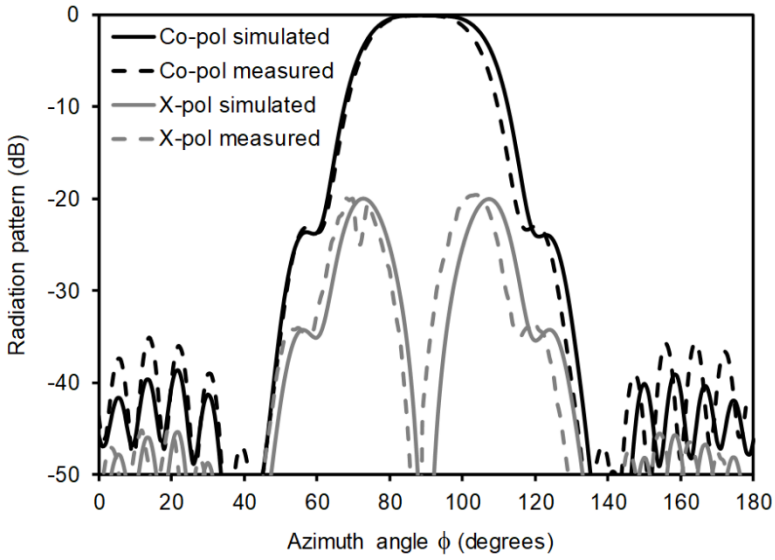

Fig. 8 - Measured and simulated normalized *E*-plane radiation patterns of the SIW LWA, evaluated at the frequency $f = 28$ GHz [82].

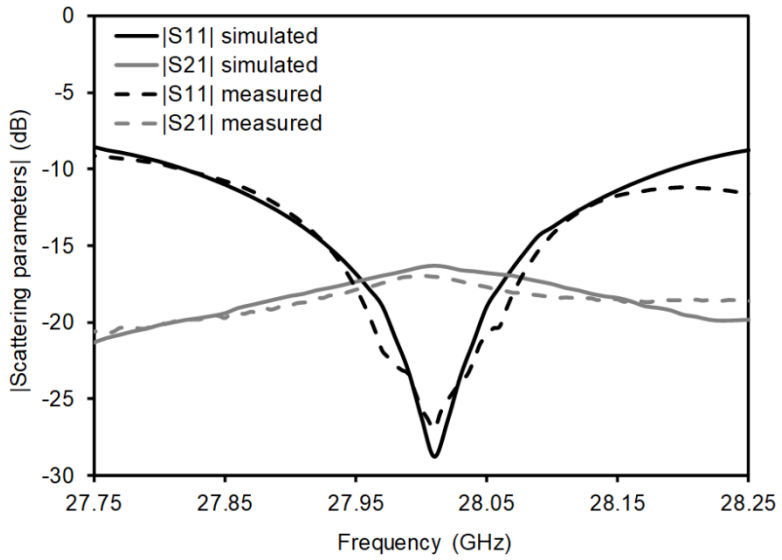

Fig. 9 - Measured and simulated scattering parameters versus frequency for the SIW LWA [82].

3.5 Design and Testing of a Double-sided SISW LWA

A double-sided SISW LWA, with same characteristics of the double-sided SIW LWA of Section 3.4, has been investigated with the aim of increasing the overall system efficiency. Same specifications of f=28 GHz, as centre operative frequency, θ_{RAD} = 50°, as radiating pointing angle, and θ= 10°, as beamwidth have been maintained for the study of this SISW LWA prototype. In addition, a detailed view of the three-dimensional prototype is provided in Fig. 10, along with its main geometric parameters and optimized values, retrieved via the full-wave software Ansys HFSS.

In particular, the device consists of a slight yet fundamental modification of the central transmission line, that represents the antenna itself. The SIW-line is replaced by a SISW-line, with a central dielectric part and lateral air-filled enclosures. Moreover, for mechanical considerations and manufacturing requirements, the central dielectric part has been connected to the lateral sides by means of small dielectric stubs. This solution presents a negligible effect in terms of transmission properties and has been taken into account in simulations. Eventually, the same feeding system adopted for the SIW LWA has been chosen to implement a direct, compact, low-cost and low-loss coax cable to SISW transition.

Subsequently, in order to validate the simulated results, a prototype has been manufactured. A detailed view of top and bottom faces, prior to the soldering of the connectors, and prior to the metallization of the posts, is highlighted in Fig. 11. The

substrate adopted is the RT/duroid® 6002 laminate, with the following characteristics: $\varepsilon_r = 2.94$, $\tan\delta = 0.0012$, thickness $h = 0.508$ mm, and metal conductivity $\sigma = 5.8 \cdot 10^7$ S/m. Furthermore, as for technology process, a laser drilling numerically controlled milling machine has been adopted to shape the metal layers and to drill the holes through the substrate. Then, the holes have been metallized by electroplating, and, finally, the connectors have been inserted through the substrate and soldered to both metal planes, ensuring the transmission of the quasi-TE_{20} mode and preventing the fundamental quasi-TE_{10} mode transmission inside the structure. Eventually, commercial copper adhesive tape has been used to close the top and bottom planes, thus completing the prototype manufacturing.

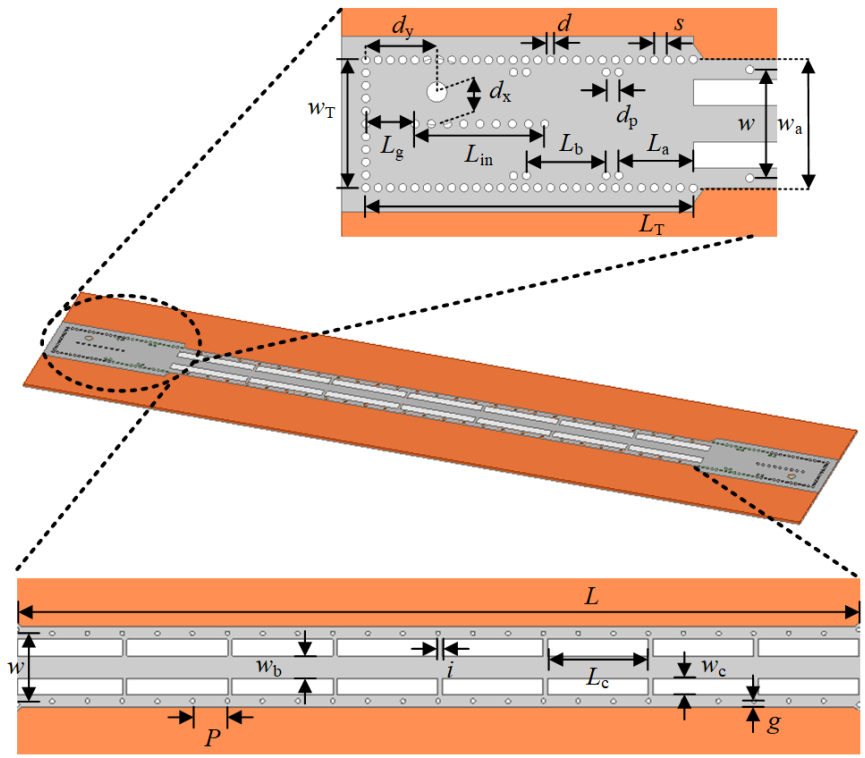

Fig. 10 - 3D model of the SISW LWA [82].
Upper part: detailed highlight of the feeding and transition used to excite the quasi-TE_{20} mode (values of the parameters in mm: $w_T = 8$, $d_y = 4.45$, $d_x = w/4 = 2$, $L_g = 3.08$, $L_{in} = 8$, $L_a = 4.65$, $L_b = 5$, $L_T = 20.5$, $w = 6.8$, $w_a = 8$, $d_p = 1$, $s = 1$, and $d = 0.5$).
Lower part: detailed highlight of the main SISW-line (values of the parameters in mm: $w = 6.8$, $w_b = 2.27$, $w_c = 1.7$, $P = 3.54$, $g = 0.6$, $L = 95.5$, $i = 0.508$, and $L_c = 13.135$).

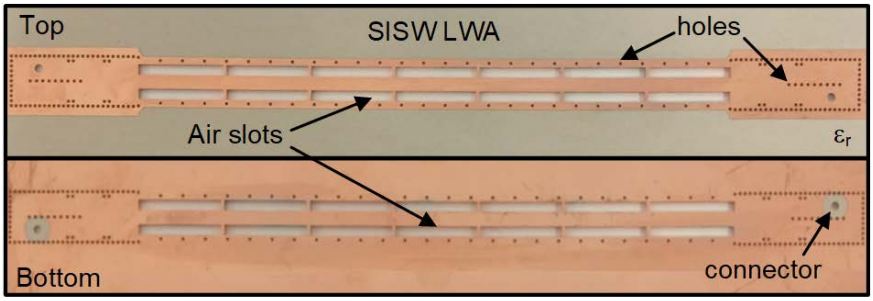

Fig. 11 - Photograph of the manufactured SISW LWA prototype [82].

Afterwards, the same prototype has been experimentally validated. First, in Fig. 12 are depicted the simulated (solid line) and measured (dashed line) normalized radiation pattern of the SIW LWA in the *H*-plane (yz-plane, i.e. ϕ=90°), at the operative frequency of f=28 GHz. In this case, measurements validate both the pointing angle of 50° and the beamwidth of 10°, thus demonstrating a good control of the complex propagation constant, as foreseen in simulations. Following, the normalized radiation patterns for the *E*-plane are highlighted in Fig. 13. In this case, the *E*-plane is defined along the angle of maximum radiation (θ_{RAD} = 50°) and the angle ϕ assumes values in the range from 0° to 180°. In both cases, measured results are in good agreement with the simulated outcomes. Moreover, the cross-pol is well maintained, both in simulation (-20 dB) and measurement (-22 dB), under -20 dB with respect to the normalized maximum value of the co-pol for the whole range of ϕ. Furthermore, it has been noted that the co-pol component has a -3 dB beamwidth of $\Delta\theta$=34° in simulation and $\Delta\theta$= 32° in measurement, and a maximum gain of 15.94 dB in simulation and 15.88 dB in measurement. This measured gain leads to an overall efficiency of 94.24% for the SISW LWA prototype. Eventually, the scattering parameters versus frequency are reported in Fig. 14. Measured results are in dashed lines, while simulated results are in solid lines. In particular, at the working frequency of f=28 GHz, the measured $|S_{11}|$=-24.51 dB confirms by the simulated $|S_{11}|$=-20.55 dB, and also the measured $|S_{21}|$=-14.87 dB proves the simulated $|S_{21}|$=-15.50 dB. Moreover, the observed narrow band is due to the compact feeding used to excite the second quasi-TE_{20} SISW mode, and in total agreement with the previous double-sided SIW LWA. As mentioned above, other configurations [78], based on branch lines could provide wider bandwidths at the expense of increasing the overall size of the system.

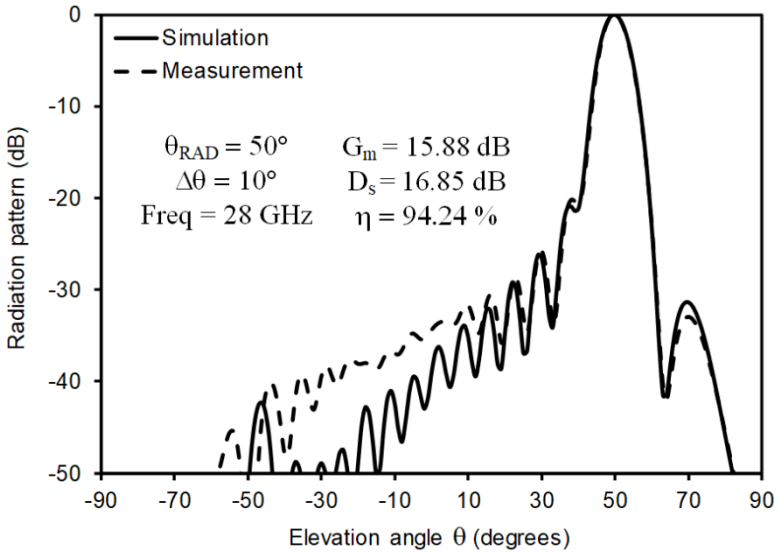

Fig. 12 - Measured and simulated normalized *H*-plane ($\phi = 90°$) radiation pattern of the SISW LWA, evaluated at the frequency $f = 28$ GHz [82].

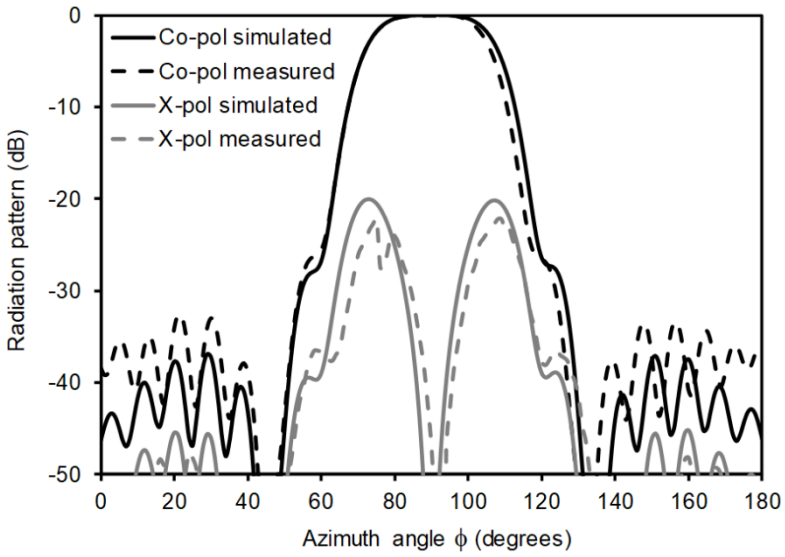

Fig. 13 - Measured and simulated normalized *E*-plane radiation patterns of the SISW LWA, evaluated at the frequency $f = 28$ GHz [82].

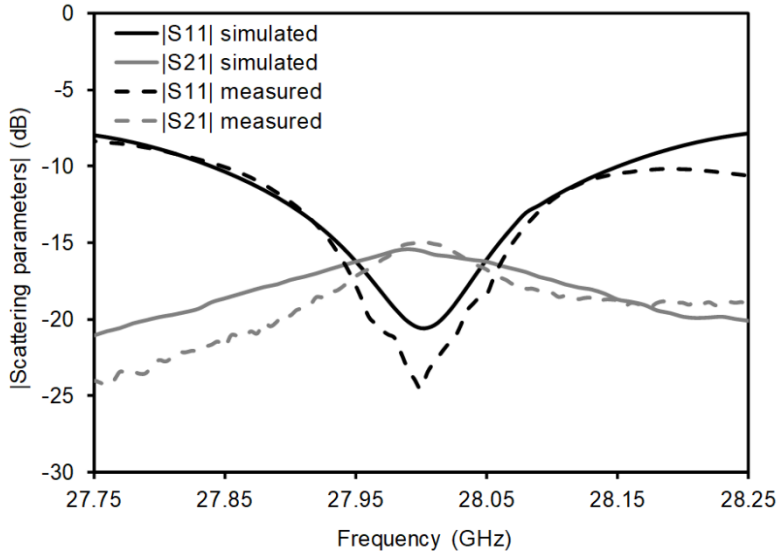

Fig. 14 - Measured and simulated scattering parameters for the SISW LWA [82].

3.6 Double-sided SIW and SISW LWAs Comparison

Section 3.4 and Section 3.5 presented a double-sided SIW LWA and a double-sided SISW LWA, respectively. Same radiation characteristics have been adopted during the design procedure ($f = 28$ GHz, $\theta_{RAD} = 50°$, and $\theta = 10°$), in order to directly compare the performance of those antennas in terms of efficiency. To summarize those results, Table II highlights the measured gain values and the estimated antennas efficiencies. At the working frequency of $f = 28$ GHz, the SIW LWA efficiency reaches the 88.15%. This value is increased when considering the SISW LWA, that exhibits an antenna efficiency of the 94.24%. In this way, as already observed in Section 3.3, the reduction of transmission losses provided by the SISW-line with respect to the SIW-line guarantees an overall increase of the system efficiency. Finally, this Chapter presented and experimentally proved the possibility to adopt double-sided SISW LWA as a novel class of extremely high efficiency antennas for the novel fifth generation (5G) of mobile communications.

TABLE II
EFFICIENCY COMPARISON

Antenna	Measured gain (dB)	Simulated directivity (dB)	Efficiency (%)
SIW LWA	14.21	16.12	88.15
SISW LWA	15.88	16.85	94.24

3.7 Conclusions

This Chapter presented the design, manufacturing and experimental verification of both SIW and SISW double-sided leaky-wave antennas (LWAs). In particular, the possibility to increase the efficiency of double-sided LWAs adopting the substrate integrated slab waveguide technology has been highlighted, as main goal for this dissertation.

At first, a brief historical overview on generic SIW antennas has been presented and widely discussed, following the guidelines of [3]. Subsequently, a special attention has been addressed to the double-sided SIW LWA, enumerating its advantages, and presenting the theoretical aspects, along with analytical formulas. After that, a deep investigation on the attenuation constant α for SIW and SISW lines has been discussed. In detail, as already observed in [43], adopting the SISW configuration and considering the second quasi-TE_{20} mode, it is possible to significantly reduce transmission losses, leading to the design of high efficiency microwave antennas. Subsequently, a double-sided SIW LWA has been designed, manufactured and experimentally validated, operating at the frequency of 28 GHz, with a beamwidth θ of 10°, and a radiating pointing angle θ_{RAD} of 50°. Afterwards, a double-sided SISW LWA, with same radiation properties, has been designed, fabricated and tested with the aim of demonstrating a better overall system efficiency. Eventually, this comparison proved the increased efficiency of the double-sided SISW LWA (94.24%) with respect to the double-sided SIW LWA (88.15%).

In conclusion, those prototypes, operating at 28 GHz, paved the road to the future implementation of a performing class of double-sided SISW LWA, with extremely high efficiency, for the novel fifth generation (5G) of mobile communications and wireless sensors networks (WSN).

Conclusions

This work has been entirely dedicated to the Substrate Integrated Waveguide (SIW) technology and its applications in the microwave regime. In particular, a special attention has been addressed to the investigation of novel materials and fabrication procedures. In detail, additive manufacturing processes, also known as 3D printing techniques, have been considered for the implementation of SIW interconnects, along with an intensive research on innovative and composite printable plastic filaments. Subsequently, subtractive manufacturing procedures have been applied for the implementation of a completely original two SIW modes coaxial launcher, able to sustain both the propagation of the fundamental quasi-TE_{10} and the second quasi-TE_{20} modes in the same physical prototype. Eventually, combining the results achieved in the 3D-printed substrate integrated slab waveguide (SISW) and in the combined coaxial SIW launcher, a double-sided SISW leaky-wave antenna (LWA) has been designed, manufactured and experimentally validated, proving an increased efficiency with respect to the classical double-sided SIW LWA. All these results are well inserted in the stimulating and ever-growing research field of SIW technology, laying the foundations to a future class of microwave components and systems, that well fit in the novel Internet of Things (IoT) scenario, specifically considering the fifth generation (5G) of mobile communications and the wireless sensors networks (WSN) applications.

In detail, Chapter 1 highlighted the possibility of 3D printing SIW interconnects, via the Fused Deposition Modelling (FDM) technique, and by using the thermoplastic polyurethane Ninjaflex® filament. In particular, the major contribution of this work is related to the feasibility of additive manufacturing techniques, especially suited for an innovative class of microwave components.

In particular, the characterization of the printable dielectric material, the validation of the FDM process, and the testing of both SIW and SISW interconnects

have been proposed as a technological demonstrator for a novel class of RF, microwave, and mm-wave 3D-printed components and systems.

Furthermore, considering the framework of the ever-increasing interest for the SIW technology, the possibility to implement novel broadband interconnects by 3D printing represents a remarkable innovation, towards fully integrated and shielded microwave systems. In particular, considering this work, the proposed 3D-printed SISW interconnect covers a mono-modal bandwidth 50% wider than the standard SIW line bandwidth. Besides the broader operation bandwidth, the interesting characteristic of the proposed waveguide is the possibility to implement the structure in one-single fabrication pass and using only one-single TPU filament. Finally, while nowadays losses of 3D-printed structures are still large, many composite and innovative materials are currently under development for 3D printing applications, which are expected to exhibit significantly lower losses in the near future.

In addition, particularly those experimental outcomes paved the road to the implementation of novel microwave components, based on the local variation of the dielectric permittivity, and suggest a technique to effectively reduce dielectric losses. In detail, this study has represented the motivation for the work highlighted in Chapter 3.

In conclusion, Chapter 1 proved the possibility to print fully three-dimensional SIW interconnects, adopting low-cost and flexible dielectric materials, via the versatile one-pass FDM procedure, with the possibility of varying the infill percentage, in order to tune both the dielectric constant and the loss tangent, for the implementation of a novel class of performing SIW microwave components and systems.

Eventually, within the context of Chapter 1, an ancillary topic has been discussed in Appendix 1. In particular, an original, low-cost and compact SIW cavity sensor, with enhanced sensitivity, for the electromagnetic characterization of materials, has been proposed for the first time. Specifically, the device consists of a cylindrical SIW cavity with a hole in the centre, in order to locate a glass pipe, that contains the material to be tested. Precisely, the major novelty consists of slight yet fundamental modification with respect to the standard SIW sensor: that is an added metal sheath around the pipe, which has proved to increase the sensitivity of the device.

In detail, this enhanced SIW cavity sensor is preferred especially for the characterization of printable materials, usually selected to fabricate microwave devices by additive manufacturing techniques. In fact, the importance of retrieving

accurate values for the dielectric constant and loss tangent factor is fundamental when dealing with innovative 3D printing procedures. Moreover, those values are required for a precise microwave design. In particular, the standard filaments, for the FDM technology, can be tested in a non destructive way. Indeed, the filament alone can be inserted and subsequently removed from the hole of the SIW sensor, in a safe and fast way. Afterwards, the same filament can be re-used to construct the specific designed microwave component, thus making the entire manufacturing procedure fast, economical, and convenient.

Furthermore, it is possible to integrate the sensor in a single substrate, adopting the idea of the System on Substrate (SoS), already presented in the Introduction. In fact, the SIW resonant cavity, the pair of microstrip lines, and the soldered SMA connectors are implemented on the same physical board.

In addition, this enhanced SIW cavity sensor represents also an easily repeatable and inexpensive product, thus constituting an intriguing solution both for industries and laboratories.

Bearing in mind all those features, the proposed enhanced SIW cavity sensor paves the road to a low-cost and smart characterization of the unknown electrical properties of 3D printable materials, particularly suited for microwave designs.

Subsequently, in Chapter 2, the design strategy, the manufacturing procedure, and the experimental verification of direct, compact, low-cost, and low-profile coaxial cable to SIW transitions have been presented and widely discussed. In fact, among all transitions between SIW and other topologies of circuitry, the coax-to-SIW transitions are able to provide low transmission losses and are capable to support the propagation of higher order modes.

Bearing in mind all those features, the major novelty of this work consists of an innovative two SIW modes combined launcher, that enables the possibility to sustain both the fundamental quasi-TE_{10} and the second quasi-TE_{20} modes, within the same physical prototype.

To this aim, at the beginning of the investigation, the transitions for the single SIW modes have been considered separately. In parallel, several parametric analyses have been conducted through Ansys HFSS on substrate thickness, coaxial cable displacement, and capacitive effect next to the feeding point, thus constituting the design criteria to efficiently optimize the transitions themselves. Eventually, for all the cases, and for measurement purposes, back-to-back prototypes have been manufactured and tested, proving the simulated outcomes.

At this stage, considering the achieved results by the single SIW mode launchers, the innovative two SIW modes combined launcher has been proposed, along with design strategy, manufacturing procedure and measurements, confirming the theoretical and simulated predictions. In addition, measured fractional bandwidths (FBWs) and insertion losses (ILs) have been reported in Chapter 2, summarized in Table I, and compared to the state of the art of coax-to-SIW transitions. In detail, the combined prototype is able to cover a 35.1% FBW, evaluated at -15 dB, with measured IL of 0.23 dB at $f = 7$ GHz, interesting data among the investigated scientific literature. Moreover, it is also offering a 13.2% FBW, evaluated at -15 dB, with measured IL of 0.78 dB at $f = 10.5$ GHz, feature not present in any of the above mentioned transitions.

Last, another relevant property consists in the direct insertion of the coaxial cable through the substrate, that implements a simple, repeatable and robust to fabrication inaccuracies solution. Indeed, this feature could be considered as fundamental property when dealing with industrial applications.

Besides, the possibility to cover two different frequency bands, using only one physical transmission channel, makes the two SIW modes combined launcher an extremely interesting transition for the development of a novel class of performing SIW components and systems for the new wireless sensors network (WSN) and 5G applications.

Afterwards, Chapter 3 has been dedicated to the study of SIW antennas. In particular, both SIW and SISW double-sided leaky-wave antennas (LWAs) have been designed, manufactured and experimentally validated, with the aim of increasing the overall antenna efficiency. In particular, a special attention has been addressed to LWA for their performing radiation properties, and for the achieved high values of gain and directivity. In detail, theoretical bases and analytical formulas have been listed in Chapter 3, enabling an accurate electromagnetic design.

Successively, recalling the consideration of Chapter 1, a deep investigation on the attenuation constant α for SIW and SISW lines has been discussed in Chapter 3. In detail, as already observed in Section 1.3, adopting the SISW configuration and considering the second quasi-TE_{20} mode, it is possible to significantly reduce transmission losses, leading to the design of high efficiency microwave antennas, as subsequently demonstrated in this work.

In parallel, in order to properly excite the transmission of the second quasi-TE_{20} mode inside the proposed double-sided LWAs, the coaxial cable to SIW transition presented in Chapter 2 has been adopted. In particular, it provides a

compact in size, and direct solution for the feeding system, necessary for measurement purposes.

Subsequently, to summarize the achieved results, the double-sided SIW and SISW LWAs operating at 28 GHz have been designed, manufactured and experimentally validated adopting same radiation properties: beamwidth θ of 10°, and radiating pointing angle θ_{RAD} of 50°, thus enabling the possibility of a direct comparison. Eventually, properly this comparison proved the increased efficiency of the double-sided SISW LWA (94.24 %) with respect to the double-sided SIW LWA (88.15 %).

In conclusion, the prototypes presented in this work, operating at 28 GHz, paved the road to the future implementation of a performing class of double-sided SISW LWA with extremely high efficiency for the novel fifth generation (5G) of mobile communications and wireless sensors networks (WSN).

Eventually, the entire work proposed a detailed overview on the Substrate Integrated Waveguide (SIW) technology and its applications, highlighting the original and stimulating possibilities offered by this technology. Moreover, a broad investigation about novel manufacturing procedures and innovative materials have been considered, leading to the validation of 3D-printed SIW interconnects. In parallel, even a two SIW modes combined coaxial launcher and a double-sided SISW LWA have been proposed for the first time, opening interesting design opportunities for a future class of RF, microwave and mm-wave components and systems. In addition, those results well fit with the recent industry market requirements, inserted into the Internet of Things (IoT) scenario, the fifth generation (5G) of mobile communication and the wireless sensors network (WSN).

Appendix 1

Substrate Integrated Waveguide (SIW) Sensors for Material Characterization

This Appendix presents a novel, compact and low-cost SIW cavity sensor with enhanced sensitivity, especially suited for the electromagnetic characterization of materials. In particular, the device is based on a cylindrical SIW cavity with a hole in the centre, in order to locate a glass pipe, that contains the material to be tested. In detail, the major novelty consists of slight yet fundamental modification with respect to the standard SIW sensor: that is an added metal sheath around the pipe, which has proved to increase the sensitivity of the device. Moreover, specifically this sensor can be adopted to estimate the electrical properties of printable materials in an easy, fast and non destructive way. In fact, considering FDM applications, printable filaments could be directly inserted in the hole of the SIW sensor, thus retrieving their ε_r and $\tan\delta$, without damaging the filaments themselves. Subsequently, the same filaments can be 3D printed to create the designed microwave components. To summarize, an innovative, compact and not expensive SIW sensor has been designed, manufactured and experimentally validated and it allows for a fast, precise, and non destructive testing of materials, retrieving their electrical properties, and enabling a precise design of an original class of 3D-printed microwave devices and systems.

Considering the recent wider spectrum of scientific applications, the development of novel and low-cost sensors for the characterization of the electromagnetic properties of materials has been receiving wide attention in the last years, also in conjunction with the implementation of lab-on-chip systems [147]. In general, several different techniques have been introduced for material characterization, including coaxial probes, free-space methods, transmission-line techniques, and cavity resonator methods [83]. Among them, the cavity resonators

are particularly suitable for narrow-band and highly accurate characterization procedures. Specifically, the implementation of cavity resonators is particularly convenient in Substrate Integrated Waveguide (SIW) technology, which allows for low-cost solutions and relatively high quality factor [84]. Moreover, considering the recent scientific literature, several sensors based on SIW cavities have been proposed [85]-[90]. As for those examples, a typical sensor consists of a SIW cavity resonator, manufactured on a commercial low-loss laminate substrate, with a small hole drilled in the middle of the cavity, and a glass testing pipe containing the material under test (MUT) inserted through the hole [90], [148]. Then, the MUT determines a variation of the resonance frequency f_{res} and of the quality factor Q of the fundamental cavity mode, which in turn allows retrieving the MUT's dielectric properties. Specifically, an example of SIW cavity perturbation technique has been presented in [85]. Similar considerations have been adopted for the work presented in the next Sections. In particular, in this Appendix, an improved SIW cavity sensor for the characterization of materials has been proposed. In detail, the device sensitivity has been considerably enhanced by means of the addition of a metal sheath around the glass pipe (Fig. 1), which increases the penetration of the electromagnetic field into the pipe. Furthermore, the retrieval of dielectric permittivity and loss tangent of a variety of materials has been highlighted and the results are compared with the values measured adopting a commercial coaxial probe.

Eventually, all those results have been collected and published in [91].

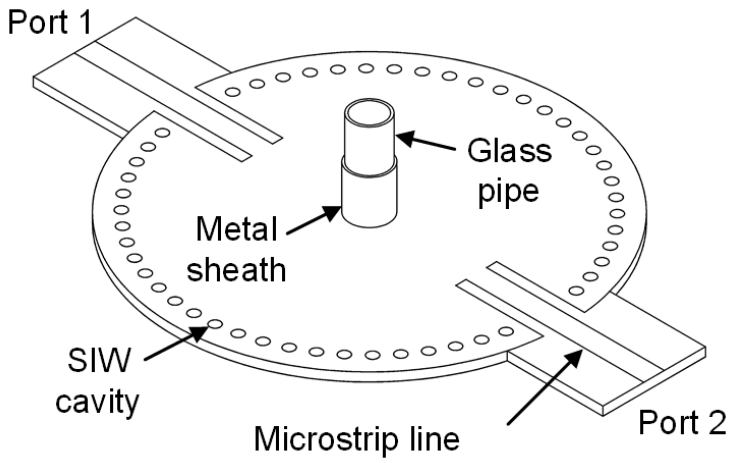

Fig. 1 - 3D view of the modified SIW sensor with the addition of the metal sheath [91].

A.1 Standard SIW Two-port Sensor

This Section is entirely dedicated to the design and manufacturing of a standard SIW two-port sensor. In particular, the standard topology consists of a cylindrical resonant cavity with a hole in the centre, fed by a pair of microstrip lines added for measurement purposes. Moreover, theoretical aspects are well known among the scientific community, and the working principle is pretty simple: the cavity resonates on the fundamental TM_{010} mode, whose electric field amplitude is maximum at the centre and minimum at the rim. Subsequently, when the glass pipe is inserted through the cavity hole, the presence of the material under test (MUT) perturbs the electromagnetic field inside the cavity, by shifting the resonance frequency f_{res} and changing the quality factor Q. Specifically, this phenomenon occurs because the MUT modifies the effective dielectric permittivity and the effective loss tangent of the resonator. In effect, in the empty cavity, the hole is filled with air, and therefore the presence of any MUT shifts down the resonance frequency and reduces the quality factor. Finally, this briefly summarize the behaviour of the standard SIW two-port sensor.

Afterwards, a prototype based on a circular SIW cavity, operating inside the Industrial, Scientific and Medical (ISM)-band around the frequency of 2.45 GHz, has been designed and fabricated. A photograph of the manufactured device is shown in Fig. 2. In particular, regarding the material properties, the substrate is a standard Taconic TLY-5 laminate, with height $h = 1.52$ mm, relative dielectric permittivity $\varepsilon_r = 2.2$, loss tangent $\tan\delta = 0.0009$, and metal conductivity $\sigma = 5.8\times10^7$ S/m. Eventually, the geometrical parameters of the structure are also listed on the right-hand side of Fig. 2.

Subsequently, the structure has been simulated through the full wave electromagnetic simulator High Frequency Structure Simulator (HFSS), provided by Ansys. After that, a prototype has been manufactured by using the LPKF E33 milling machine, which is able to pattern the metal layers and drill the holes through the substrate. Then, to finalize the device, a silver-based conductive paste has been used to metalize the via holes of the SIW.

In addition, it is worth noting that the behaviour of this SIW cavity is different from the one observed in standard metallic cavity resonators. In fact, due to the small thickness h of the SIW cavity, this structure exhibits a strong reactance at the edge of the central hole, thus limiting the penetration of the electromagnetic field in the hole and reducing the effect of the MUT. This phenomenon is evident on the left-hand side of Fig. 3, which shows the amplitude of the electric field inside

the cavity at the resonance frequency f_{res}. This problem results into a low sensitivity to the change of the MUT's electromagnetic characteristics, and motivated a deep investigation that lead to the proposal of the modified SIW sensor.

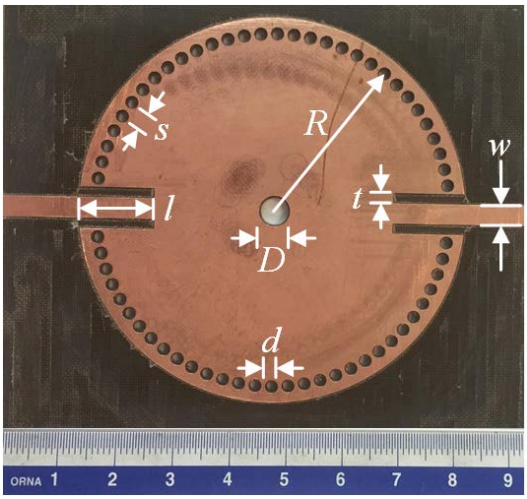

Parameter	Dimension (mm)
d	2.0
D	5.1
s	2.88
l	12.8
t	1.5
R	31.2
w	4.0

Fig. 2 - Photograph of the manufactured SIW sensor along with its physical dimensions [91].

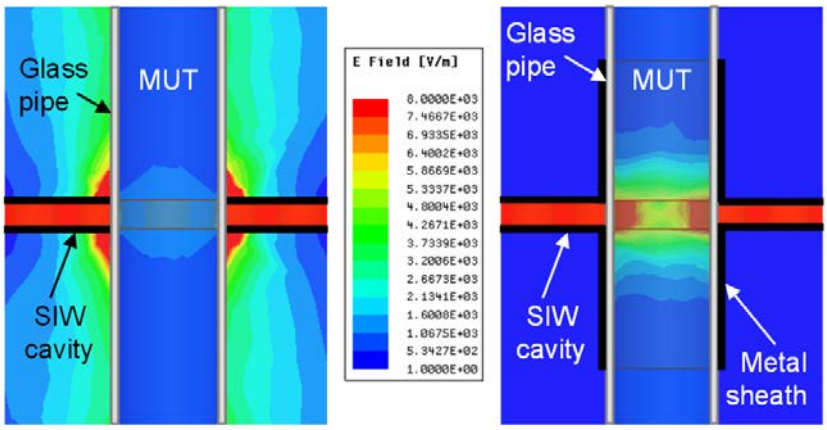

Fig. 3 - Amplitude of the electric field at the resonant frequency
in the standard SIW sensor (on the left) and in the enhanced SIW sensor (on the right) [91].

A.2 Enhanced SIW Two-port Sensor

This Section is entirely dedicated to the design and manufacturing of a novel SIW two-port sensor. In particular, this enhanced structure will outclass the limitation of the standard sensor based on an SIW cavity, that consists on the strong reactance at the edge of the hole, where the MUT is inserted. Specifically, this problem can be mitigated by adding a metal sheath wrapping the glass testing pipe, as previously shown in Fig. 1. Precisely, this allows the electromagnetic field to penetrate more deeply inside the MUT, as depicted on the right-hand side of Fig. 3. Moreover, the metal sheath wrapped around the glass pipe behaves like a waveguide section below cut off, thus avoiding spurious radiation. The benefit of the proposed solution is an enhanced sensitivity of the sensor and a better accuracy in the retrieval of the electrical characteristics of the MUT.

Furthermore, same software, design strategies, materials and fabrication facilities adopted for the standard SIW sensor have been employed also for the enhanced SIW sensor. Besides, the only exception consists on the implementation of the additional metal sheath. In fact, in the experimental verification, the added metal sheath was simply made by using a commercial aluminium conductive tape, directly wrapped around the glass testing pipe and fixed on both conductive planes, to ensure electrical contact.

At this stage, both prototypes are ready to be experimentally tested.

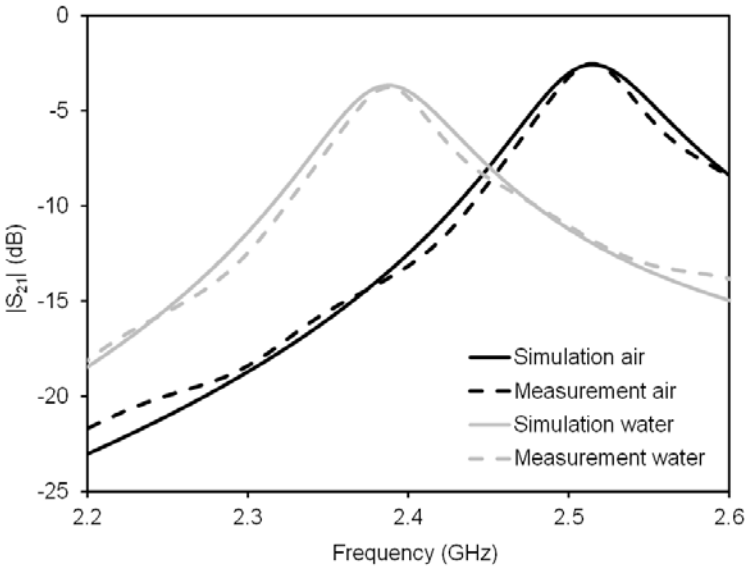

Fig. 4 - Simulated (continuous lines) and measured (dashed lines) transmission coefficient $|S_{21}|$ for distilled water (ε_r=77 and tanδ=0.12, in grey) and air (ε_r=1, in black), for the enhanced SIW sensor [91].

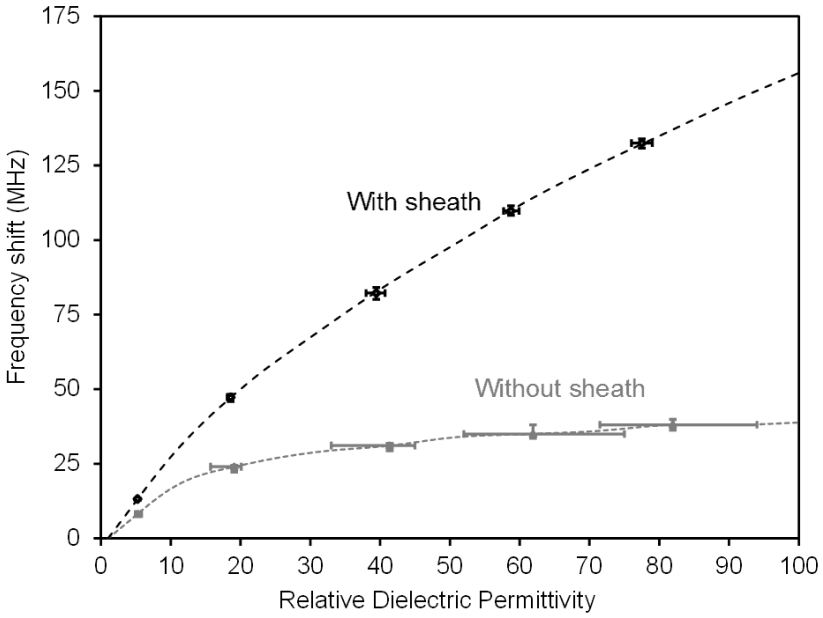

Fig. 5 - Simulated curves of frequency shift Δf versus ε_r, for the standard SIW sensor (without sheath) and the enhanced SIW sensor (with sheath), along with measured values (dot symbols) and related error bars for the five different liquid mixtures [91].

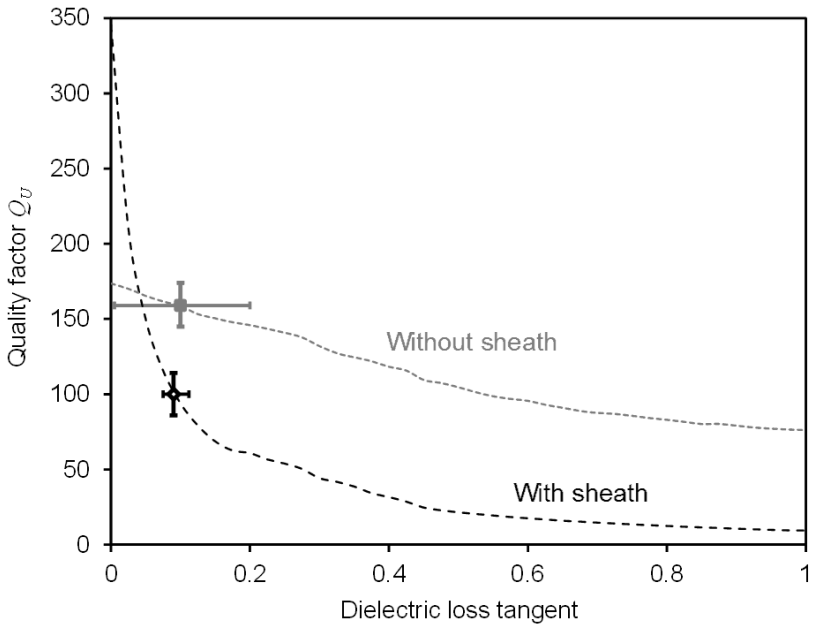

Fig. 6 - Simulated curves of unloaded quality factor Q_U versus tanδ (with ε_r=77), for the standard SIW sensor (without sheath) and the enhanced SIW sensor (with sheath), along with measured values (dot symbols) and relative error bars related to 100% water MUT [91].

TABLE I

MEASUREMENT OF DIELECTRIC PERMITTIVITY AND LOSS TANGENT OF DIFFERENT LIQUID MIXTURES FOR THE STANDARD SIW SENSOR

Mixture Under Test	f_{res} (GHz)	Coaxial Probe		Standard SIW sensor			
		ε_r	tanδ	ε_r	$\Delta\varepsilon_r$	tanδ	Δtanδ
100% Isopropanol	2.525	5.14	0.728	5.29	2.84%	0.65	10.71%
75% Isopropanol/25% Water	2.512	18.35	0.608	19.09	3.88%	0.54	11.18%
50% Isopropanol/50% Water	2.501	39.21	0.375	41.37	5.22%	0.34	9.33%
25% Isopropanol/75% Water	2.496	58.47	0.238	61.91	5.56%	0.21	11.76%
100% Water	2.493	77.14	0.119	81.94	5.86%	0.09	24.37%

TABLE II

MEASUREMENT OF DIELECTRIC PERMITTIVITY AND LOSS TANGENT OF DIFFERENT LIQUID MIXTURES FOR THE ENHANCED SIW SENSOR

Mixture Under Test	f_{res} (GHz)	Coaxial Probe		Enhanced SIW sensor			
		ε_r	tanδ	ε_r	$\Delta\varepsilon_r$	tanδ	Δtanδ
100% Isopropanol	2.519	5.16	0.724	5.25	1.71%	0.68	6.08%
75% Isopropanol/25% Water	2.472	18.45	0.603	18.60	0.81%	0.57	5.47%
50% Isopropanol/50% Water	2.446	39.41	0.368	39.45	0.10%	0.35	4.89%
25% Isopropanol/75% Water	2.418	58.71	0.230	58.75	0.07%	0.22	4.35%
100% Water	2.391	77.22	0.110	77.50	0.36%	0.10	9.09%

A.3 Experimental Results

This Section is entirely dedicated to the testing of both manufactured SIW sensors. At first, in order to test the quality of the proposed sensor, the measurement of different liquid mixtures has been performed by using the enhanced SIW sensor, described in Section A.2. Specifically, a graduate scale of different mixing percentages between isopropanol and distilled water has been considered. In particular, for this work, five mixtures have been prepared: 100 % Isopropanol, 75 % Isopropanol and 25 % Water, 50 % Isopropanol and 50 % Water, 25 % Isopropanol and 75 % Water, and last 100 % Water, thus constituting a variegated scientific set to be analysed. In detail, those liquid mixtures require to be inserted in the glass pipe, located in the central hole of the SIW cavity, as shown in Fig. 1. Furthermore, the simulated (continuous line) and measured (dashed line) amplitude of the transmission coefficient $|S_{21}|$ is reported in Fig. 4, for both distilled

water ($\varepsilon_r = 77$ and $\tan\delta = 0.12$) and air ($\varepsilon_r = 1$), providing a good agreement. Those cases represent the extremes for the resonant frequencies, in the estimate of the electrical properties of the unknown materials, considered in this work. In fact, the air introduces the higher resonant frequency due to its lower ε_r, while the water presents a lower resonant frequency due to its higher ε_r, thus constituting the extremes of the interval for the estimates of the considered liquid mixtures.

Subsequently, it is worth noting that the measurement of the scattering parameters is of crucial importance. In fact, the scattering parameters allow determining the resonance frequency f_{res} and the unloaded quality factor Q_U of the cavity and, in turns, the electromagnetic properties of the MUT [83]. Furthermore, the simulated frequency shift $\Delta f = f_0 - f_{res}$ (where f_0 represents the resonance frequency in the case of air-filled pipe) versus the relative dielectric permittivity of the generic MUT is shown in Fig. 5, for both SIW cavity sensor configurations. Specifically, in this figure, the outcomes obtained using the standard SIW sensor without metal sheath, presented in Section A.1, and the results obtained using the enhanced SIW sensor with metal sheath, highlighted in Section A.2, are plotted together for ease of comparison. In detail, the proposed sensor (black curve and symbols) clearly exhibits a larger variation of the resonance frequency with respect to the standard sensor (grey curve and symbols), resulting into an increased sensitivity. Indeed, according to the definition presented in [85], the sensitivity has been identified as $S = dF/d\varepsilon_r$, where $F = \Delta f / f_0$ represents the fractional frequency shift. In particular, the sensitivity is useful to compare devices working in different frequency bands. Here, since the devices compared in Fig. 5 are working at nearly the same frequencies (designed in the ISM band, around 2.45 GHz), the slopes of the curves have practically the same meaning as the sensitivity *S*. Last, for both SIW sensor configurations, it is important to highlight the fact that the symbols are related to the five different liquid mixtures, listed at the beginning of this Section. Instead, the dashed curves represent the simulated outcomes of the parametric analyses conducted via HFSS. Considering the configuration of the standard sensor, without metallic sheath, it is clear as the slope of the curve seems saturating for higher values of ε_r, and the frequency span is covering almost only 30-35 MHz. Moreover, the error bars, plotted on the measured symbols, emphasize the high inaccuracies in the estimate of the dielectric permittivity for the proposed liquid mixtures, as they will be clearly mentioned in Table I. Conversely, the enhanced SIW sensor is able to span a frequency band of more than 150 MHz, five times more than the standard SIW sensor case, thus presenting an augmented sensitivity. Even more, the error bars are largely small when compared to the respective ones of the standard sensor, thus leading to a better estimate of the dielectric constant. Eventually, values will be reported in detail in Table I and Table II, respectively.

Following, the simulated unloaded quality factor Q_U versus the loss tangent $\tan\delta$ is shown in Fig. 6, for both SIW sensor configurations, with and without metal sheath. Similarly to the previous case, even the dielectric loss tangent estimate is more accurate while adopting the enhanced SIW cavity sensor. Also in this figure, the curves are related to the HFSS simulated outcomes, while the dotted symbols refer to the measurements of the distilled water ($\varepsilon_r = 77$). In addition, the sensitivity is way higher for the enhanced SIW cavity sensor, and the different slopes of the curves prove this observation. Eventually, even error bars assume significant diverse quantities, leading to different error percentages in the estimate of the loss tangent for the considered distilled water sample. Precise values are reported in Table I and Table II, respectively.

Eventually, to summarize all the outcomes of the performed experimental validations, the values of the relative dielectric permittivity and loss tangent of the five different liquid mixtures have been measured using the standard and the enhanced SIW cavity sensors and reported in Table I and Table II, respectively. In particular, these data are compared with the ones obtained by using the commercial coaxial probe Keysight 85070E Dielectric Probe Kit, considered as a reference test methodology. Moreover, those results refer to the measured resonance frequencies of each different material and sensor type, fundamental feature for a detailed and precise comparison. Therefore, Table I presents the five different liquid mixtures in the first column, along with their resonant frequencies, in the second column, retrieved adopting the standard SIW cavity sensor. Subsequently, the values of ε_r and $\tan\delta$ are measured with the coaxial probe, and listed in the third and fourth columns. Then the retrieved values of ε_r and $\tan\delta$ with the standard SIW sensor are reported in the fifth and seventh columns, and their percentage differences with respect to the reference are highlighted in the sixth and eighth columns. The percentage difference in the estimate of the dielectric constant is always less than the 6%, while it reaches the 25% in the estimate of the loss tangent for the distilled water. Same analyses have been replicated to fill Table II, regarding outcomes for the enhanced SIW cavity sensor. In this case, the difference in the dielectric permittivity with respect to the coaxial probe values is below 1.7% for all liquid mixtures. Furthermore, reasonably good accuracy is also shown in the estimate of the loss tangent, with a relative difference below than 6% for all MUTs except for distilled water, which exhibits a relative difference of 9%. Last, it is worth noting that all values of ε_r, retrieved via both SIW sensors, show slightly higher values when compared to the outcomes of the coaxial probe. Moreover, the values of $\tan\delta$ are lower with respect to coaxial probe estimates. This phenomenon is attributed to a small air layer between the pipe and the sheath, as confirmed by several HFSS simulations.

In conclusion, the proposed enhanced SIW cavity sensor exhibits a better accuracy in the determination of both dielectric permittivity and loss tangent for all the analysed liquid mixtures, when compared to the standard SIW cavity sensor.

A.4 Conclusions

A low-cost and compact SIW cavity sensor, with enhanced sensitivity, for electromagnetic characterization of materials, has been presented and validated in this Appendix. In particular, the device is based on a cylindrical SIW cavity with a hole in the centre, in order to locate a glass pipe, that contains the material to be tested. In detail, the major novelty consists of slight yet fundamental modification with respect to the standard SIW sensor: that is an added metal sheath around the pipe, which has proved to increase the sensitivity of the device.

Specifically, both prototypes for the standard SIW sensor and the enhanced SIW sensor have been designed, manufactured and experimentally validated. Specially, a set of different liquid mixtures have been tested to retrieve their dielectric permittivity and loss tangent values, with both device configurations. Moreover, a coaxial probe, with an embedded measurement software, has been adopted as a reference, to compare the different measured outcomes. Finally, the proposed SIW sensor always outperforms the standard SIW sensor, and, in all cases, the relative difference with the coaxial probe results is better than 1.7% for the dielectric permittivity and 9% for the dielectric loss tangent.

Eventually, this novel enhanced SIW cavity sensor could be adopted in the estimate of the electrical properties of unknown materials, specially suited for additive manufacturing applications. In fact, the importance of retrieving accurate values for dielectric constant and loss tangent is fundamental when dealing with innovative 3D printing procedures. Moreover, those values are required for a precise microwave design. In particular, the filament adopted in the FDM technology, can be tested in a non destructive way. Indeed, the filament can be inserted in the hole of the cavity, in this way perturbing the field and shifting the resonant frequency, thus leading to the estimate of its electrical properties. Afterwards, it can be removed safely and immediately used to construct the specific designed microwave component. For all those reasons, the proposed enhanced SIW cavity sensor paves the road to a low-cost and smart characterization of the unknown electrical properties of 3D printable materials, particularly suited for microwave and mm-waves applications.

Appendix A

Standard IEEE frequency bandwidths

Name	Frequency range
HF	3 – 30 MHz
VHF	30 – 300 MHz
UHF	300 – 1000 MHz
L	1 – 2 GHz
S	2 – 4 GHz
C	4 – 8 GHz
X	8 – 12 GHz
X-Tx	7.19 GHz
X-Rx	8.45 GHz
Ku	12 – 18 GHz
K	18 – 26.5 GHz
Ka-Rx	32.05 GHz
Ka-Tx	34.45 GHz
Q	30 – 50 GHz
U	40 – 60 GHz
V	50 – 75 GHz
E	60 – 90 GHz
W	75 – 110 GHz
F	90 – 140 GHz
D	110 – 170 GHz

Appendix B
List of Abbreviations

ADS = Advanced Design System

AM = Additive Manufacturing

ASTM = American Society for Testing and Materials

FDM = Fused Deposition Modelling

HFSS = High Frequency Structure Simulator

HMSIW = Half Mode Substrate Integrated Waveguide

IoT = Internet of Things

ISM = Industrial Scientific and Medical (Band)

LWA = Leaky-wave Antenna

MUT = Material Under Test

NRD = Non Radiative Dielectric

SIFW = Substrate Integrated Folded Waveguide

SIRW = Substrate Integrated Ridge Waveguide

SISW = Substrate Integrated Slab Waveguide

SIW = Substrate Integrated Waveguide

SLM = Selective Laser Melting

TPU = Thermoplastic Polyurethane

WSN = Wireless Sensors Networks

Bibliography

[1] M. Bozzi and K. Wu, "Guest Editorial," *IEEE Transactions on Microwave Theory and Techniques*, Vol. 66, No. 6, pp. 2915-2919, June 2018.

[2] K. Wu, Y. J. Cheng, T. Djerafi and W. Hong, "Substrate-Integrated Millimeter-Wave and Terahertz Antenna Technology," *Proceedings of the IEEE*, Vol. 100, No. 7, pp. 2219-2232, July 2012.

[3] R. Garg, I. Bahl, and M. Bozzi, “Microstrip Lines and Slotlines,” 3rd ed. Norwood, MA, USA, Artech House, 2013.

[4] F. Shigeki, “Waveguide line,” (in Japanese) Japan Patent 06–053 711, Feb. 25, 1994.

[5] D. Deslandes, and K. Wu, “Integrated Microstrip and Rectangular Waveguide in Planar Form,” *IEEE Microwave Wireless Comp. Lett.*, Vol. 11, No. 2, 2001, pp. 68–70.

[6] D. Deslandes, and K. Wu, “Single–Substrate Integration Technique of Planar Circuits and Waveguide Filters,” *IEEE Trans. on Microwave Theory and Tech.*, Vol. 51, No. 2, 2003, pp. 593–596.

[7] F. Xu, and K. Wu, “Guided–Wave and Leakage Characteristics of Substrate Integrated Waveguide,” *IEEE Trans. on Microwave Theory and Tech.*, Vol. 53, No. 1, 2005, pp. 66–73.

[8] D. Deslandes, and K. Wu, “Accurate Modeling, Wave Mechanisms, and Design Considerations of a Substrate Integrated Waveguide,” *IEEE Trans. on Microwave Theory and Tech.*, Vol. 54, No. 6, 2006, pp. 2516–2526.

[9] R. E. Collin, “Field Theory of Guided Waves,” Wiley–IEEE Press, 1991.

[10] Y. Cassivi, et al., “Dispersion Characteristics of Substrate Integrated Rectangular Waveguide,” *IEEE Microwave Wireless Comp. Lett.*, Vol. 12, No. 9, 2002, pp. 333–335.

[11] W. Che, et al., “Analytical Equivalence Between Substrate–Integrated Waveguide and Rectangular Waveguide,” *IET Microwave Ant. Propagat.*, Vol. 2, No. 1, 2008, pp. 35–41.

[12] M. Bozzi, L. Perregrini and K. Wu, “Modeling of Conductor, Dielectric and Radiation Losses in Substrate Integrated Waveguide by the Boundary Integral-Resonant Mode Expansion Method,” *IEEE Trans. Microwave Theory Tech.*, Vol. 56, No. 12, 2008, pp. 3153–3161.

[13] M. Bozzi, et al., “On the Losses in Substrate Integrated Waveguides and Cavities,” *International J. Microwave and Wireless Technologies*, Vol. 1, No. 5, 2009, pp. 395–401.

[14] M. Pasian, M. Bozzi and L. Perregrini, "A Formula for Radiation Loss in Substrate Integrated Waveguide," *IEEE Transactions on Microwave Theory and Techniques*, Vol. 62, No. 10, pp. 2205-2213, Oct. 2014.

[15] M. Bozzi, L. Perregrini, and K. Wu, “Modeling of Losses in Substrate Integrated Waveguide by Boundary Integral–Resonant Mode Expansion Method,” *IEEE MTT–S International Microwave Symposium Digest* (IMS 2008), Atlanta, GA, June 10–15, 2008, pp. 515–518.

[16] M. Bozzi, L. Perregrini and K. Wu, "Modeling of Conductor, Dielectric, and Radiation Losses in Substrate Integrated Waveguide by the Boundary Integral-Resonant Mode Expansion Method," *IEEE Transactions on Microwave Theory and Techniques*, Vol. 56, No. 12, pp. 3153-3161, Dec. 2008.

[17] D. Deslandes, “Design Equations for Tapered Microstrip–to–Substrate Integrated Waveguide Transitions,” *IEEE MTT–S International Microwave Symposium Digest* (IMS 2010), Anaheim, CA, May 23–28, 2010, pp. 704–707.

[18] D. Deslandes, and K. Wu, “Integrated Transition of Coplanar to Rectangular Waveguides,” *IEEE MTT–S International Microwave Symposium Digest* (IMS 2001), Baltimore, MD, June 5–10, 2001, pp. 619–622.

[19] W.-P. Chen, and K. Wu, “Low–Loss Ultra–Wideband Transition between Conductor–Backed Coplanar Waveguide and Substrate Integrated Waveguide,” *IEEE MTT–S International Microwave Symposium Digest* (IMS 2009), Boston, MA, June 7–12, 2009, pp. 349–352.

[20] A. Patrovsky, M. Daigle, and K. Wu, “Millimeter–Wave Wideband Transition from CPW to Substrate Integrated Waveguide on Electrically Thick High–Permittivity Substrates,” *37th European Microwave Conference 2007*, Munich, Germany, Oct. 8–12, 2007, pp. 138–141.

[21] D. Deslandes, and K. Wu, “Analysis and Design of Current Probe Transition from Grounded Coplanar to Substrate Integrated Rectangular Waveguides,” *IEEE Trans. on Microwave Theory and Tech.*, Vol. 53, No. 8, 2005, pp. 2487–2494.

[22] A. Morini, M. Farina, C. Cellini, T. Rozzi, and G. Venanzoni, “Design of low-cost non-radiative SMA-SIW launchers,” *Proc. 36th Eur. Microw. Conf.*, pp. 526–529, Sept. 2006.

[23] E. Arnieri, G. Amendola, L. Boccia, and G. D. Massa, “Coaxially fed substrate integrated radiating waveguides,” *Proc. IEEE Antennas Propag. Soc. Int. Symp.*, pp. 2718–2721, Jun. 2007.

[24] S. Mukherjee, P. Chongder, K. V. Srivastava, and A. Biswas, “Design of a broadband coaxial to substrate integrated waveguide (SIW) transition,” *Proc. Asia-Pasific. Microw. Conf.*, pp. 896–898, Nov. 2013.

[25] A. A. Khan, M. K. Mandal, and R. Shaw, “A compact and wideband SMA connector to empty substrate integrated waveguide (ESIW) transition,” *Proc. IEEE MTT-S Int. Microw. RF Conf.* (IMaRc), pp. 246–248, Dec. 2015.

[26] A. A. Khan, and M. K. Mandal, “A Compact Broadband Direct Coaxial Line to SIW Transition,” *IEEE Microwave and Wireless Components Letters*, Vol. 26, No. 11, pp. 894-896, Nov. 2016.

[27] A. Suntives, and R. Abhari, “Design and Application of Multimode Substrate Integrated Waveguides in Parallel Multichannel Signaling Systems,” *IEEE Transactions on Microwave Theory and Techniques*, Vol. 57, No. 6, pp. 1563-1571, June 2009.

[28] D.-Y. Kim, J. W. Lee, T. K. Lee, and C. S. Cho, “Design of SIW Cavity-Backed Circular-Polarized Antennas Using Two Different Feeding Transitions,” *IEEE Transactions on Antennas and Propagation*, Vol. 59, No. 4, pp. 1398-1403, April 2011.

[29] M. A. Tlaxcalteco-Matus, and R. Torres-Torres, “Systematic Modeling and Characterization of a Via-to-SIW Transition,” *IEEE Microwave and Wireless Components Letters*, Vol. 20, No. 12, pp. 657-659, Dec. 2010.

[30] G. L. Chen, T. L. Owen, and J. H. Whealton, “Theoretical Study of the Folded Waveguide,” *IEEE Trans. Plasma Science*, Vol. 16, No. 2, 1988, pp. 305–311.

[31] N. Grigoropoulos, B. S. Izquierdo, and P. R. Young, “Substrate Integrated Folded Waveguides (SIFW) and Filters,” *IEEE Microwave Wireless Comp. Lett.*, Vol. 15, No. 12, 2005, pp. 829–831.

[32] W. Che, L. Geng, K. Deng and Y. L. Chow, "Analysis and Experiments of Compact Folded Substrate-Integrated Waveguide," *IEEE Transactions on Microwave Theory and Techniques*, Vol. 56, No. 1, pp. 88-93, Jan. 2008.

[33] W. Hong, et al., “Half Mode Substrate Integrated Waveguide: A New Guided Wave Structure for Microwave and Millimeter Wave Application,” *Proc. Joint 31st International Conference on Infrared Millimeter Waves and 14th International Conference on Terahertz Electronics*, Shanghai, China, Sept. 18–22, 2006, p. 219.

[34] Q. Lai, et al., “Characterization of the Propagation Properties of the Half–Mode Substrate Integrated Waveguide”, *IEEE Trans. on Microwave Theory and Tech.*, Vol. 57, No. 8, 2009, pp. 1996–2004.

[35] G. Macchiarella, C. Tomassoni, E. Massoni, M. Bozzi, and L. Perregrini, “A Novel Class of Half-Mode SIW Filters with Extracted Poles,” *47th European Microwave Conference* (EuMC2017), Nuremberg, Germany, Oct. 8–13, 2017.

[36] E. Massoni, N. Delmonte, G. Macchiarella, L. Perregrini, and M. Bozzi, “Half-mode SIW Filters with Resonant Couplings Implementing Transmission Zeros,” *2018 IEEE MTT-S International Microwave Symposium* (IMS2018), Philadelphia, PA, USA, 10-15 June 2018.

[37] G. H. Zhai, et al., “Folded Half Mode Substrate Integrated Waveguide 3 dB Coupler,” *IEEE Microwave Wireless Comp. Lett.*, Vol. 18, No. 8, 2008, pp. 512–514.

[38] N. Delmonte, C. Tomassoni, M. Bozzi and L. Perregrini, "Compact resonators in substrate integrated waveguide technology," *2018 IEEE MTT-S International Wireless Symposium (IWS)*, Chengdu, 2018, pp. 1-3.

[39] N. Delmonte, C. Tomassoni, M. Bozzi, and L. Perregrini, "Miniaturization and Quality-Factor in Substrate Integrated Waveguide Cavities," *2018 IEEE MTT-S International Conference on Numerical Electromagnetic and Multiphysics Modeling and Optimization* (NEMO2018), Reykjavik, Iceland, Aug. 8-10, 2018.

[40] P. H. Vartanian, and A. L. Helgesson, “Propagation in Dielectric Slab Loaded Rectangular Waveguide,” *IEEE Trans. on Microwave Theory and Tech.*, Vol. 6, No. 2, 1958, pp. 215–222.

[41] M. Bozzi, et al., “Efficient Analysis and Experimental Verification of Substrate Integrated Slab Waveguides for Wideband Microwave Applications,” *International J. RF and Microwave Computer-Aided Engineering*, Vol. 15, No. 3, 2005, pp. 296–306.

[42] L. Silvestri, E. Massoni, C. Tomassoni, A. Coves, M. Bozzi, and L. Perregrini, "Substrate Integrated Waveguide Filters Based on a Dielectric Layer with Periodic Perforations," *IEEE Transactions on Microwave Theory and Techniques*, Vol. 65, No. 8, pp. 2687–2697, Aug. 2017.

[43] E. Massoni, L. Silvestri, G. Alaimo, S. Marconi, M. Bozzi, L. Perregrini, and F. Auricchio, "3D-Printed Substrate Integrated Slab Waveguide for Single-Mode Bandwidth Enhancement," *IEEE Microwave and Wireless Components Letters*, Vol. 27, No. 6, pp. 536-538, June 2017.

[44] S. B. Cohn, “Properties of Ridge Waveguide,” *Proc. IRE*, Vol. 35, No. 8, 1947, pp. 783–788.

[45] W. Che, et al., “Propagation and Band Broadening Effect of Planar Integrated Ridged Waveguide in Multilayer Dielectric Substrates,” *IEEE MTT–S International Microwave Symposium Digest* (IMS 2008), Atlanta, GA, June 10–15, 2008, pp. 217–220.

[46] W. Che, et al., “Investigations on Propagation and the Band Broadening Effect of Ridged Rectangular Waveguide Integrated in a Multilayer Dielectric Substrate,” *IET Microwaves, Ant. and Propagat.*, Vol. 4, No. 6, 2010, pp. 674–684.

[47] M. Bozzi, S. A. Winkler, and K. Wu, “Broadband and Compact Ridge Substrate Integrated Waveguides,” *IET Microwave Ant. and Propagat.*, Vol. 4, No. 11, 2010, pp. 1965–1973.

[48] S. Moscato, R. Moro, M. Pasian, M. Bozzi, and L. Perregrini, "Two-Material Ridge Substrate Integrated Waveguide for Ultra-Wide Band Applications," *IEEE Transactions on Microwave Theory and Techniques*, Vol. 63, No. 10, pp. 3175-3182, Oct. 2015.

[49] Wu, K., “Towards System–on–Substrate Approach for Future Millimeter–Wave and Photonic Wireless Applications,” *Proc. Asia–Pacific Microwave Conference 2006*, Yokohama, Japan, Dec. 12–15, 2006, pp. 1895–1900.

[50] Li, Z., and K. Wu, “24–GHz Frequency–Modulation Continuous–Wave Radar Front–End System–on–Substrate,” *IEEE Trans. Microwave Theory Tech.*, Vol. 56, No. 2, 2008, pp. 278–285.

[51] Samanta, K. K., D. Stephens, and I. D. Robertson, “Design and Performance of a 60–GHz Multi–Chip Module Receiver Employing Substrate Integrated Waveguides,” *IET Microwaves, Antennas Propagat.*, Vol. 1, No. 5, 2007, pp. 961–967.

[52] B.-J. Chen, T.-M. Shen, and R.-B. Wu, “Dual–Band Vertically Stacked Laminated Waveguide Filter Design in LTCC Technology,” *IEEE Trans. on Microwave Theory and Tech.*, Vol. 57, No. 6, 2009, pp. 1554–1562.

[53] H.-Y. Chien, et al., “Miniaturized Bandpass Filters With Double–Folded Substrate Integrated Waveguide Resonators in LTCC,” *IEEE Trans. on Microwave Theory and Tech.*, Vol. 57, No. 7, 2009, pp. 1774–1782.

[54] I.-J. Hyeon, et al., “Fully Micromachined, Silicon–Compatible Substrate Integrated Waveguide for Millimetre–Wave Applications,” *Electron. Lett.*, Vol. 47, No. 5, 2011, pp. 328–330.

[55] S. Cheng, H. Yousef, and H. Kratz, “79 GHz Slot Antennas Based on Substrate Integrated Waveguides (SIW) in a Flexible Printed Circuit Board,” *IEEE Trans. Antennas and Propagat.*, Vol. 57, No. 1, 2009, pp. 64–71.

[56] R. Moro, et al., “Novel Inkjet–Printed Substrate Integrated Waveguide (SIW) Structures on Low–Cost Materials for Wearable Applications,” *42nd European Microwave Conference 2012*, Amsterdam, The Netherlands, Oct. 28–Nov. 2, 2012.

[57] R. Moro, et al., “Wearable Textile Antenna in Substrate Integrated Waveguide Technology,” *IET Electron. Lett.*, Vol. 48, No. 16, 2012, pp. 985–987.

[58] E. Massoni, P. F. Espin Lopez, M. Pasian, M. Bozzi, L. Perregrini, S. Marconi, G. Alaimo, and F. Auricchio, “Additive Manufacturing of a Chalk Powder NRD 3-port Junction via Binder Jetting Technology,” *IEEE MTT-S International Microwave Workshop Series-Advanced Materials and Processes* (IMWS-AMP 2017), Pavia, Italy, 20-22 Sept. 2017.

[59] E. Massoni, P. F. Espin-Lopez, M. Pasian, M. Bozzi, L. Perregrini, G. Alaimo, S. Marconi, and F. Auricchio, “3D-printed Chalk Powder for Microwave Devices: Experimental Results for a NRD-guide in Ku-Band,” *47th European Microwave Conference* (EuMC2017), Nuremberg, Germany, Oct. 8–13, 2017.

[60] E. Moldovan, R.G. Bosisio and K. Wu, “W–Band Multiport Substrate–Integrated Waveguide Circuits,” *IEEE Trans. on Microwave Theory and Tech.*, Vol. 54, No. 2, 2006, pp. 625–632.

[61] B. Youzkatli El Khatib, T. Djerafi, and K. Wu, "Substrate-Integrated Waveguide Vertical Interconnects for 3-D Integrated Circuits," *IEEE Transactions on Components, Packaging and Manufacturing Technology*, Vol. 2, No. 9, pp. 1526-1535, Sept. 2012.

[62] A. Suntives, R. Abhari, "Transition Structures for 3-D Integration of Substrate Integrated Waveguide Interconnects," *IEEE Microwave and Wireless Components Letters*, Vol. 17, No. 10, pp. 697-699, Oct. 2007.

[63] J. J. Simpson, A. Taflove, J. A. Mix, and H. Heck, "Substrate integrated waveguides optimized for ultrahigh-speed digital interconnects," *IEEE Transactions on Microwave Theory and Techniques*, Vol. 54, No. 5, pp. 1983-1990, May 2006.

[64] S.-H. Yang, “Wireless sensor networks: principles, design and applications,” Springer, 2014.

[65] F. Calignano *et al.*, "Overview on Additive Manufacturing Technologies," *Proceedings of the IEEE*, Vol. 105, No. 4, pp. 593-612, April 2017.

[66] E. MacDonald, R. Salas, D. Espalin, et al., “3D printing for the rapid prototyping of structural electronics,” *IEEE Access*, 2, pp. 234–242, 2014.

[67] C. Chua, K. Leong, and C. Lim, “Rapid prototyping: principles and applications,” River Edge, NJ, USA, 2003.

[68] H. Lipson and M. Kurman, “Fabricated: The New World of 3D Printing,” John Wiley & Sons, 2013.

[69] S. Moscato, R. Bahr, T. Le, M. Pasian, M. Bozzi, L. Perregrini, and M.M. Tentzeris, “Additive Manufacturing of 3D Substrate Integrated Waveguide Components,” *Electronics Letters*, Vol. 51, No. 18, pp. 1426-1428, Sept. 2015.

[70] E. Massoni, L. Silvestri, M. Bozzi, L. Perregrini, G. Alaimo, S. Marconi, and F. Auricchio, "Characterization of 3D-Printed Dielectric Substrates with Different Infill for Microwave Applications," *IEEE MTT-S International Microwave Workshop Series on Advanced Materials and Processes for RF and THz Applications* (IMWS-AMP 2016), Chengdu, China, July 20-22, 2016.

[71] M.J. Da Cruz and H. W. Francis, "Face and content validation of a novel three-dimensional printed temporal bone for surgical skills development," *JLO*, Vol. 129, Issue S3, pp. S23-S29, July 2015.

[72] N. Bizzotto, I. Tami, A. Santucci, R. Adani, P. Poggi, D. Romani, G. Carpeggiani, F. Ferraro, S. Festa and B. Magnan "3D Printed replica of articular fractures for surgical planning and patient consent: a two years multi-centric experience," *3D Printing in Medicine*, Vol. 2, No. 2, 2016.

[73] Z. Onerci Altunay, J.A. Bly, P.K. Edwards, D.R. Holmes, S. Hamilton, E.K. O'Brien, A.B. Carr, J.J. Camp, J.K. Stokken, J.F. Pallanch, "Three- dimensional printing of large nasal septal perforations for optimal prosthetic closure," *American Journal of Rhinology & Allergy*, Vol. 30, No. 4, pp. 287-293 (7), July-August 2016.

[74] A. Périgaud, S. Bila, O. Tantot, N. Delhote and S. Verdeyme, "3D printing of microwave passive components by different additive manufacturing technologies," *2016 IEEE MTT-S International Microwave Workshop Series on Advanced Materials and Processes for RF and THz Applications* (IMWS-AMP), Chengdu, 2016, pp. 1-4.

[75] O. A. Peverini *et al*., "Selective Laser Melting Manufacturing of Microwave Waveguide Devices," *Proceedings of the IEEE*, Vol. 105, No. 4, pp. 620-631, April 2017.

[76] A. Georgiadis, J. Kimionis, and M. M. Tentzeris, "3D/Inkjet-printed millimeter wave components and interconnects for communication and sensing," *2017 IEEE Compound Semiconductor Integrated Circuit Symposium* (CSICS), Miami, FL, 2017, pp. 1-4.

[77] M. Bozzi, S Moscato, L. Silvestri, N. Delmonte, M. Pasian, and L. Perregrini, “Innovative SIW Components on Paper, Textile, and 3D-Printed Substrates for the Internet of Things,” *2015 Asia-Pacific Microwave Conference* (APMC2015), Nanjing, China, Dec. 6–9, 2015.

[78] D. Pozar, “Microwave Engineering,” 4th Edition, JohnWiley & Sons, Hoboken, NJ, 2012.

[79] S. Moscato, R. Bahr, T. Le, M. Pasian, M. Bozzi, L. Perregrini, and M.M. Tentzeris, "Infill Dependent 3D-Printed Material Based on NinjaFlex Filament for Antenna Applications," *IEEE Antennas and Wireless Propagation Letters*, Vol. 15, No. 1, 2016.

[80] C. Tomassoni, R. Bahr, M. Bozzi, L. Perregrini, and M. Tentzeris, "3D Printed Substrate Integrated Waveguide Filters with Locally Controlled Dielectric Permittivity," *46th European Microwave Conference* (EuMC2016), London, UK, Oct. 3–7, 2016.

[81] H.-M. Chang and C. Liao, "A Parallel Derivation to the Maxwell-Garnett Formula for the Magnetic Permeability of Mixed Materials," *World Journal of Condensed Matter Physics*, Vol. 1, pp. 55-58, 2011.

[82] E. Massoni, M. Bozzi, and K. Wu, "Increasing the Efficiency of Leaky-Wave Antennas by Using the Substrate Integrated Slab Waveguide," *IEEE Antennas and Wireless Propagation Letters*, (submitted).

[83] L. F. Chen et al., "Microwave Electronics: Measurement and Materials Characterization," *Ed. John Wiley & Sons*, Chichester, UK, 2004.

[84] M. Bozzi, A. Georgiadis, and K. Wu, "Review of substrate integrated waveguide (SIW) circuits and antennas," *IET Microw. Antennas Propag.*, Vol. 5, No. 8, pp. 909–920, June 2011.

[85] K. Saeed, R. D. Pollard, and I. C. Hunter, "Substrate integrated waveguide cavity resonators for complex permittivity characterization of materials," *IEEE Trans. Microw. Theory Techn.*, Vol. 56, No. 10, pp. 2340-2347, Oct. 2008.

[86] C. Liu, and F. Tong, "An SIW resonator sensor for liquid permittivity measurements at C band," *IEEE Microw. Compon. Lett.*, Vol. 25, No. 11, pp. 751-753, Nov. 2015.

[87] Y. Seo, M. U. Memon, and S. Lim, "Microfluidic eighth-mode substrate-integrated-waveguide antenna for compact ethanol chemical sensor application," *IEEE Trans. Antennas Propag.*, Vol. 64, No. 7, pp. 3218-3222, July 2016.

[88] N. Y. Sama, M. Ndoye, D. Deslandes, and F. Domingue, "Partially-open SIW resonator for microwave characterization of particulate dielectrics: effect of interaction with gases," *2016 IEEE International Workshop on Electromagnetics* (iWEM), pp. 1-3, Nanjing, China, May 16-18, 2016.

[89] S. Liu et al., "A 90 GHz liquid sensing substrate integrated cavity resonator in LTCC for microfluidic sensing applications," *2014 IEEE MTT-S International Microwave Workshop Series on RF and Wireless Technologies for Biomedical and Healthcare Applications* (IMWS-Bio2014) , pp. 1-3, London, UK, Dec. 8-10, 2014.

[90] A. K. Jha and M. J. Akhtar, "SIW cavity based RF sensor for dielectric characterization of liquids," *IEEE Conf. Antenna Measurements and Applications*, Antibes, France, Nov. 16-19, 2014.

[91] E. Massoni, G. Siciliano, M. Bozzi, and L. Perregrini, "Enhanced Cavity Sensor in SIW Technology for Material Characterization," *IEEE Microwave and Wireless Components Letters* (in print).

[92] M.D. Janezic and J.A. Jargon, "Complex permittivity determination from propagation constant measurements," *IEEE Microwave and Guided Wave Letters*, Vol. 9, No. 2, pp. 76-78, Feb. 1999.

[93] Z.-C. Hao, W. Ding and W. Hong, “Developing Low-Cost W-Band SIW Bandpass Filters Using the Commercially Available Printed-Circuit-Board Technology,” *IEEE Transactions on Microwave Theory and Techniques*, Vol. 64, No. 6, pp. 1775-1786, June 2016.

[94] A. J. Martinez-Ros, M. Bozzi and M. Pasian, "Double-Sided SIW Leaky-Wave Antenna With Increased Directivity in the E-Plane," *IEEE Transactions on Antennas and Propagation*, Vol. 66, No. 6, pp. 3130-3135, June 2018.

[95] Z. Y. Zhang, Y. R. Wei and K. Wu, "Broadband Millimeter-Wave Single Balanced Mixer and Its Applications to Substrate Integrated Wireless Systems," *IEEE Transactions on Microwave Theory and Techniques*, Vol. 60, No. 3, pp. 660-669, March 2012.

[96] J. L. Cano, E. Villa, A. Mediavilla and E. Artal, "A Wideband Correlation and Detection Module Based on Substrate-Integrated Waveguide Technology for Radio Astronomy Applications," *IEEE Transactions on Microwave Theory and Techniques*, Vol. 66, No. 6, pp. 3145-3152, June 2018.

[97] P. Wu, S. Liao, and Q. Xue, “Wideband Excitations of Higher-Order Mode Substrate Integrated Waveguides and Their Applications to Antenna Array Design,” *IEEE Transactions on Antennas and Propagation*, Vol. 65, No. 8, pp. 4038-4047, Aug. 2017.

[98] L. Sun, Y. Zhang, Y. Cai, and Z. Qian, “Wideband excitation technology of substrate integrated waveguide TE30 mode and its antenna application,” *IET Electronics Letters*, Vol. 53, No. 13, pp. 828-830, June 2017.

[99] M. Du, J. Xu, Y. Dong, and X. Ding, “LTCC SIW-Vertical-Fed-Dipole Array Fed by a Microstrip Network With Tapered Microstrip-to-SIW Transitions for Wideband Millimeter-Wave Applications,” *IEEE Antennas and Wireless Components Letters*, Vol. 16, pp. 1953-1956, July 2017.

[100] X. Dai, “An Integrated Millimeter-Wave Broadband Microstrip-to-Waveguide Vertical Transition Suitable for Multilayer Planar Circuits,” *IEEE Microwave and Wireless Components Letters*, Vol. 26, No. 11, pp. 897-899, Nov. 2016.

[101] L. Li, Z. Wu, K. Yang, X. Lai and Z. Lei, "A Novel Miniature Single-Layer Eighth-Mode SIW Filter With Improved Out-of-Band Rejection," *IEEE Microwave and Wireless Components Letters*, Vol. 28, No. 5, pp. 407-409, May 2018.

[102] M. Lin, P. Liu, Y. Gao and J. Liu, "Improved SIW Corrugated Technique With Grounded Coplanar Waveguide Transition," *IEEE Antennas and Wireless Propagation Letters*, Vol. 17, No. 6, pp. 978-982, June 2018.

[103] R.-Y. Fang, C.-F. Liu, and C.-L. Wang, “Compact and Broadband CB-CPW-to-SIW Transition Using Stepped-Impedance Resonator With 90°-Bent Slot,” *IEEE Transactions on Components, Packaging and Manufacturing Technology*, Vol. 3, No. 2, pp. 247-252, Feb. 2013.

[104] F. Taringou, D. Dousset, J. Bornemann and K. Wu, "Substrate-integrated waveguide transitions to planar transmission-line technologies," *2012 IEEE/MTT-S International Microwave Symposium Digest*, Montreal, QC, Canada, 2012, pp. 1-3.

[105] F. F. He, K. Wu, W. Hong, L. Han and X. Chen, "A Planar Magic-T Structure Using Substrate Integrated Circuits Concept and Its Mixer Applications," *IEEE Transactions on Microwave Theory and Techniques*, Vol. 59, No. 1, pp. 72-79, Jan. 2011.

[106] F. Parment, A. Ghiotto, T-P. Vuong, L. Carpentier, and K. Wu, "Substrate Integrated Suspended Line to Air-Filled SIW Transition for High-Performance Millimeter-Wave Multilayer Integration," *IEEE MTT-S International Microwave symposium* (IMS2017), Honololu, HI, USA, June 2017.

[107] W. M. Abdel-Wahab, A. Ehsandar, H. Al-Saedi, and S. Safavi-Naeini, "E-plane metallic RWG-to-SIW transition for large-scale MM-wave phased array antenna applications," *IET Electronics Letters*, Vol. 52, No. 17, pp. 1465-1467, Aug. 2016.

[108] Y. Zhang, S. Shi, R. D. Martin and D. W. Prather, "Broadband SIW-to-Waveguide Transition in Multilayer LCP Substrates at W-Band," *IEEE Microwave and Wireless Components Letters*, Vol. 27, No. 3, pp. 224-226, March 2017.

[109] J. Dong, Y. Liu, Z. Yang, H. Peng and T. Yang, "Broadband Millimeter-Wave Power Combiner Using Compact SIW to Waveguide Transition," *IEEE Microwave and Wireless Components Letters*, Vol. 25, No. 9, pp. 567-569, Sept. 2015.

[110] J. L. Cano, A. Mediavilla, and A. R. Perez, "Full-Band Air-Filled Waveguide-to-Substrate Integrated Waveguide (SIW) Direct Transition," *IEEE Microwave and Wireless Components Letters*, Vol. 25, No. 2, pp. 79-81, Feb. 2015.

[111] E. Massoni, M. Bozzi, and L. Perregrini, " Substrate Integrated Waveguide Two-Modes Coaxial Launcher," *IEEE Transactions on Microwave Theory and Techniques*. (submitted)

[112] D. Giusto, A. Iera, G. Morabito, and L. Atzori (eds), "The Internet of Things," Springer, 2010.

[113] Special Issue, "The Internet of Things," *IEEE Wireless Communications*, Vol. 17, Issue 6, Dec. 2010.

[114] Special Issue, "The Internet of Things," *IEEE Communication Magazine*, Vol. 49, Issue 11, Nov. 2011.

[115] T. S. Rappaport et al., "Millimeter wave mobile communications for 5G cellular: It will work!," *IEEE Access*, Vol. 1, pp. 335–349, May 2013.

[116] F. Boccardi, R. W. Heath, A. Lozano, T. L. Marzetta and P. Popovski, "Five disruptive technology directions for 5G," *IEEE Communications Magazine*, Vol. 52, No. 2, pp. 74-80, February 2014.

[117] A. Osseiran, J. F. Monserrat, P. Marsch, "5G Mobile and Wireless Communications Technology," New York, NY, USA: Cambridge University Press, 2016.

[118] E. Dahlman, S. Parkvall, D. Astély, and H. Tullberg, "Advanced antenna solutions for 5G wireless access," *Proc. Asilomar ACSSC*, Nov. 2014, pp. 810-814.

[119] M. Bozzi, A. Georgiadis and K. Wu, "Review of substrate-integrated waveguide circuits and antennas," *IET Microwaves, Antennas & Propagation*, Vol. 5, No. 8, pp. 909-920, 6 June 2011.

[120] H. Xu, J. Zhou, Q. Wu, Z. Yu and W. Hong, "Wideband Low-Profile SIW Cavity-Backed Circularly Polarized Antenna With High-Gain and Conical-Beam Radiation," *IEEE Transactions on Antennas and Propagation*, Vol. 66, No. 3, pp. 1179-1188, March 2018.

[121] H. Abdel Ali, E. Massoni, L. Silvestri, M. Bozzi, L. Perregrini, and A. Gharsallah, "Increasing the Bandwidth of Cavity-Backed SIW Antennas by Using Stacked Cavities," *International Journal of Microwave and Wireless Technologies* (in print).

[122] F. Giuppi, A. Georgiadis, A. Collado, M. Bozzi and L. Perregrini, "Tunable SIW cavity backed active antenna oscillator," *Electronics Letters*, Vol. 46, No. 15, pp. 1053-1055, 22 July 2010.

[123] F. Giuppi, A. Georgiadis, A. Collado and M. Bozzi, "A Compact, Single-Layer Substrate Integrated Waveguide (SIW) Cavity-Backed Active Antenna Oscillator," *IEEE Antennas and Wireless Propagation Letters*, Vol. 11, pp. 431-433, 2012.

[124] L. Yan, et al. "Simulation and Experiment on SIW Slot Array Antennas," *IEEE Microwave Wireless Comp. Lett.*, Vol. 14, No. 9, 2004, pp. 446–448.

[125] R.S. Elliott, "An Improved Design Procedure for Small Arrays of Shunt Slots," *IEEE Trans. Antennas Propagat.*, Vol. 31, No. 1, 1983, pp. 48–53.

[126] P. Chen, et al., "A Substrate Integrated Waveguide Circular Polarized Slot Radiator and Its Linear Array," *IEEE Antennas Wireless Propagat. Lett*., Vol. 8, No. 1, 2009, pp. 120–123.

[127] D. Deslandes, and K. Wu, "Substrate Integrated Waveguide Leaky–Wave Antenna: Concept and Design Considerations," *Proc. Asia–Pacific Microwave Conference 2005*, Suzhou, China, December 4–7, 2005, pp. 346–349.

[128] F. Xu, K. Wu, and X. Zhang, "Periodic Leaky–Wave Antenna for Millimeter Wave Applications Based on Substrate Integrated Waveguide," *IEEE Trans. Antennas Propagat.*, Vol. 58, No. 2, 2010, pp. 340–347.

[129] G. Q. Luo, et al., "Planar Slot Antenna Backed by Substrate Integrated Waveguide Cavity," *IEEE Antennas Wireless Propagat. Lett.*, Vol. 7, No. 1, 2008, pp. 236–239.

[130] J. C. Bohorquez, et al., "Planar Substrate Integrated Waveguide Cavity–Backed Antenna," *IEEE Antennas Wireless Propagat. Lett*., Vol. 8, No. 1, 2009, pp. 1139–1142.

[131] H. Wang, et al., "Dielectric Loaded Substrate Integrated Waveguide (SIW) – Plane Horn Antennas," *IEEE Trans. Antennas Propagat*., Vol. 58, No. 3, 2010, pp. 640–647.

[132] X. Y. Wu and P. S. Hall, "Substrate integrated waveguide Yagi-Uda antenna," *Electronics Letters*, Vol. 46, No. 23, pp. 1541 -1542, 11 November 2010.

[133] O. Kramer, T. Djerafi and K. Wu, "Very Small Footprint 60 GHz Stacked Yagi Antenna Array," *IEEE Transactions on Antennas and Propagation*, Vol. 59, No. 9, pp. 3204-3210, Sept. 2011.

[134] G. Q. Luo, et al. "Theory and Experiment of Novel Frequency Selective Surface Based on Substrate Integrated Waveguide Technology," *IEEE Trans. Microwave Theory Tech*., Vol. 53, No. 12, 2005, pp. 4035–4043.

[135] G. Q. Luo, et al. “Design and Experimental Verification of Compact Frequency–Selective Surface With Quasi–Elliptic Bandpass Response,” *IEEE Trans. Microwave Theory Tech*., Vol. 55, No. 12, 2007, pp. 2481–2487.

[136] S. A. Winkler, et al, “Polarization Rotating Frequency Selective Surface Based on Substrate Integrated Waveguide Technology,” *IEEE Trans. Antennas Propagat*., Vol. 58, No. 4, 2010, pp. 1202–1213.

[137] A. A. Oliner and D. R. Jackson, “Leaky-wave antennas,” in Antenna Engineering Handbook, 4th ed., J. L. Volakis, Ed. New York: McGraw-Hill, Jun. 2007, ch. 11.

[138] M. Ettorre, R. Sauleau, L. L. Coq, and F. Bodereau, “Single-folded leaky-wave antennas for automotive radars at 77 ghz,” *IEEE Antennas Wireless Propag. Lett*., Vol. 9, pp. 859–862, 2010.

[139] Y. P. Zhang, “Indoor radiated-mode leaky feeder propagation at 2.0 ghz,” *IEEE Transactions on Vehicular Technology*, Vol. 50, No. 2, pp. 536–545, Mar. 2001.

[140] A. J. Martinez-Ros, J. Gomez-Tornero, and G. Goussetis, “Conformal tapered substrate integrated waveguide leaky-wave antenna,” *IEEE Trans. Antennas Propag*., Vol. 62, No. 12, pp. 5983–5991, Dec. 2014.

[141] T. Zhao, D. Jackson, J. Williams, H.-Y. Yang, and A. Oliner, “2-D periodic leaky-wave antennas-part I: metal patch design,” *IEEE Trans. Antennas Propag.*, Vol. 53, No. 11, pp. 3505 – 3514, Nov. 2005.

[142] M. Ettorre, A. Neto, G. Gerini, and S. Maci, “Leaky-wave slot array antenna fed by a dual reflector system,” *IEEE Trans. Antennas Propag*., Vol. 56, No. 10, pp. 3143–3149, Oct. 2008.

[143] W. Menzel, “A new travelling wave antenna in microstrip,” *Arch. Elektron. Uebertrag. Tech.*, Vol. 33, No. 4, pp. 137–140, Apr. 1979.

[144] A. A. Oliner, “Leakage from higher modes on microstrip line with application to antennas,” *Radio Sci.*, Vol. 22, pp. 907–912, Nov. 1987.

[145] A. J. Martinez-Ros, M. Bozzi, M. Pasian and F. Mesa, "Leaky-wave antenna in planar technology with high directivity in the transverse plane," *2017 11th European Conference on Antennas and Propagation* (EUCAP), Paris, 2017, pp. 3869-3871.

[146] A. J. Martinez-Ros, J. L. Gomez-Tornero and G. Goussetis, "Planar Leaky-Wave Antenna With Flexible Control of the Complex Propagation Constant," *IEEE Transactions on Antennas and Propagation*, Vol. 60, No. 3, pp. 1625-1630, March 2012.

[147] E. Silavwe, N. Somjit, and I. D. Robertson, “A microfluidic-integrated SIW lab-on-substrate sensor for microliter liquid characterization,” *IEEE Sensors J.*, Vol. 16, No. 21, pp. 7628-7635, Nov. 2016.

[148] H. Lobato-Morales et al., “Wireless sensing of complex dielectric permittivity of liquids based on the RFID,” *IEEE Trans. Microw. Theory Techn.*, Vol. 62, No. 9, pp. 2160-2167, Sep. 2014.